Silicon Vacancy Centers in Diamond Coupled to a Fiber-based Microcavity at Cryogenic Temperatures

Master Thesis

by

Yanik Stefan Herrmann

4th December 2019

Silicon Vacancy Centers in Diamond Coupled to a Fiber-based Microcavity at Cryogenic Temperatures

Masterarbeit

zur Erlangung des akademischen Grades

Master of Science

am Fachbereich Physik, Mathematik und Informatik

der Johannes Gutenberg-Universität

in Mainz

vorgelegt von

Yanik Stefan Herrmann

4. Dezember 2019

JOHANNES GUTENBERG
UNIVERSITÄT MAINZ

1. Evaluator: Univ.-Prof. Dr. Ferdinand Schmidt-Kaler
2. Evaluator: Univ.-Prof. Dr. Dmitry Budker

Statutory Declaration

I declare that I have authored this thesis independently, that I have not used other than the declared sources/resources, and that I have explicitly marked all material which has been quoted either literally or by content from the used sources.

Eidesstattliche Erklärung

Ich versichere, dass ich diese Dissertation selbstständig und ohne Benutzung anderer als der angegeben Hilfsmittel angefertigt habe. Alle Stellen, die wörtlich oder sinngemäß aus Veröffentlichungen oder anderen Quellen entnommen sind, sind als solche eindeutig kenntlich gemacht. Die Arbeit ist in gleicher oder ähnlicher Form noch nicht veröffentlicht und noch keiner Prüfungsbehörde vorgelegt worden.

Mainz, 4. Dezember 2019

Yanik Herrmann
Quanten-, Atom- & Neutronenphysik an der Universität Mainz (QUANTUM)
Institut für Physik
Staudingerweg 7
Johannes Gutenberg-Universität D-55099 Mainz
yherrman@students.uni-mainz.de

Abstract

The negatively charged Silicon Vacancy Color Center in diamond (SiV^-) is a promising candidate for various applications in quantum information processing. It offers a narrow zero phonon line with a high Debye Waller factor and an optical addressable electronic spin. The spin coherence time is sufficiently long for performing quantum operations, but require Millikelvin temperatures.

The SiV^- spin can serve as a stationary qubit to build up a quantum memory, an essential part of a quantum repeater. For efficient access to the spin, a robust interface between flying qubit (photon) and stationary qubit (SiV^- electronic spin or a proximal nuclear spin) has to be established. One possibility is to employ an optical resonator for enhanced emission into a well-collectible mode.

This thesis reports on the coupling of SiV^- ensembles, incorporated in a 1.4 µm thick diamond membrane into a fiber-based microcavity. The plano-concave Fabry-Pérot design has a symmetric, high reflectivity coating, which leads to a finesse of 2100. For reaching the narrow SiV^- linewidth and long spin coherence times, the microcavity is integrated into a He^3/He^4 dilution refrigerator. At liquid nitrogen temperature, the bare microcavity length could be reduced to a minimum of 1.6 µm, which corresponds to a fundamental mode order of 4, a mode volume of 5.8 λ^3 and a quality factor of ≈ 9100. The nontrivial dispersion relation between lengths and resonant wavelengths, revealed in a hybridized modes structure from the coupled system of air and diamond cavity, is observed.

SiV^- ensembles, created by silicon ion implantation inside the diamond membrane, are investigated at room temperature and at cryogenic temperatures down to liquid helium temperature. The broad zero phonon line around 738 nm with an room temperature typical linewidth of ≈ 6 nm is measured. At lower temperature, the fine structure splitting is partly resolved. Because of inhomogeneous broadening due to the high SiV^- density and potential strain in the membrane, a splitting into a doublet is recorded. At 4 K, only one SiV^- transition is visible in the spectra with a linewidth of ≈ 270 GHz. In contrast, in-grown SiV^- are subject to less inhomogeneous broadening and feature splitting into a doublet with a linewidth of ≈ 180 GHz. By measuring the excited state lifetime of the SiV^- ensemble, a Purcell-reduced lifetime of 32 % is obtained. This leads to a measured Purcell factor of 1.47.

Kurzfassung

Das negativ geladene Silizium-Fehlstellen-Farbzentrum in Diamant (SiV^-) bietet außergewöhnlich gute Eigenschaften für eine Vielzahl an Anwendung in der Quanteninformationsverarbeitung. Es zeichnet sich durch einen schmalen Null-Phonon-Übergang mt hohem Debeye-Waller-Faktor und einen optische adressierbaren, elektronischen Spin aus. Die Spinkohärenzzeit is ausreichend lange für die Anwendung von Quantengatter, benötigt allerdings Millikelvin Temperaturen.
Das SiV^- kann auch als stationäres Qubit zum Aufbau einen Quantenspeichers dienen. Dieser stellt einen Schlüsselbaustein für einen Quantenrepeater dar. Zum effizienten Kontrollieren den Spins ist eine robuste Schnittstelle zwischen fliegenden Qubit (Photon) und dem stationären Qubit (SiV^- Elektron Spin oder ein benachbarter Kernspin) notwendig. Eine Möglichkeit ist die Ankopplung an einen optischen Resonator, um die Emission mit einer Resonatormode möglichst effizient einzusammeln.
Diese Arbeit berichtet über die Kopplung von SiV^- Ensembles in einer 1.4 µm dicken Diamant Membran an einen faser-basierten Mikroresonator. Das plan-konkave Fabry-Pérot Design mit einer symmetrischen, hoch reflektierenden Spiegelbeschichtung führt zu einer Finesse von 2100. Um die besonders schmale SiV^- Linienbreite und lange Spinkohärenzzeit zu erreichen, ist der Mikroresonator in einen He^3/He^4 Mischungskryostat eingebaut. Die Mikroresonatorlänge konnte bei Flüssigstickstoff Temperaturen ohne Diamant Membran auf ein Minimum von 1.6 µm reduziert werden, was einer fundamentalen Mode mit Ordnung vier entspricht, einem Modenvolumen von 5.8 λ^3 und einem Qualitätsfaktor von $\approx$ 9100.
Die nicht triviale Dispersionsrelation zwischen Länge und resonanter Wellenlänge, welche zu einer hybriden Modenstruktur durch das gekoppelte System aus Luft und Diamant Resonator führt, ist beobachtet worden.
In die Diamant Membran implantierte SiV^- Ensembles sind bei Raumtemperatur und kryogenen Temperaturen bis hin zu 4 K untersucht worden. Die breite Null-Phonon-Übergangslinie bei 738 mit einer Raumtemperatur typischen Linienbreite von $\approx$ 6 nm ist gemessen worden. Die Feinstrukturaufspaltung bei Tieftemperaturen ist teilweise aufgenommen worden. Die inhomogen verbreiterte Linienbreite durch die hohe SiV^- Dichte und eventuelle Spannung in der Membran führen auf ein Dublett im Emissionsspektrum. Bei 4 K ist nur noch ein SiV^- Übergang sichtbar mit einer Linienbreite von $\approx$ 270 GHz. Natürlich gewachsene SiV^- Ensemble zeigen im Gegensatz dazu eine weniger inhomogen verbreiterte Linienbreite $\approx$ 180 GHz mit Aufspaltung in ein Dublett. Durch Messung der Lebenszeit des angeregten SiV^- Ensemble konnte eine Purcell-reduzierte Lebenszeitverkürzung um 32 % gemessen werden. Dies führt auf einen Purcell-Faktor von 1.47.

Contents

List of Abbreviations

SiV^-	Negatively charged Silicon Vacancy Center.
APD	Avalanche Photodiode.
BW	Broken Window Diamond Sample.
DBR	Distributed Bragg Reflector.
DL	Diode Laser.
FSR	Free Spectral Range.
FWHM	Full Width at Half Maximum.
IVC	Inner Vacuum Chamber.
LDTS	Length Dependent Transmission Spectrum.
LHe	Liquid Helium.
LN	Liquid Nitrogen.
MM	Multimode Fiber.
NV	Nitrogen Vacancy Center.
OD	Optical Density.
OVC	Outer Vacuum Chamber.
PD	Photo Diode.
PID	Proportional–Integral–Derivative.
PL	Photoluminescence.
PM	Polarization Maintaining Fiber.
PSB	Phonon Side Band.
QIP	Quantum Information Processing.
QKD	Quantum Key Distribution.
RMS	Root Mean Square.
ROC	Radius of Curvature.
SM	Singlemode Fiber.
TEM	Transverse Electromagnetic Mode.
ZPL	Zero Phonon Line.

1

Introduction: The Quantum Repeater

On October 29th in 1969, the first data ever was transmitted over the Arpanet, a prototype of the modern internet, from a computer at the University of California, Los Angeles (UCLA) to the Stanford Research Institute (SRI) in Palo Alto. The UCLA computer scientist Leonard Kleinrock described the first sending of data (the word "LOGIN"), while they are communicating with SRI by phone [Wolchover, 2019]:

> *"We typed the L and we asked, 'Did you get the L?' 'Yep' came the reply from SRI. We typed the O and asked, 'Did you get the O?' 'Yep.' We typed the G and asked, 'Did you get the G?' Crash! The SRI host had crashed. Thus was the first message that launched the revolution we now call the internet."*

One hour later, the scientist fixed the problem and successfully transmitted "LOGIN" from Los Angles to Palo Alto. In the following 50 years, this was developed into the present day internet, which radically changed modern day life.
The next stage of the evolution of the internet could be a quantum version [Kimble, 2008]. Maybe a quantum internet could become during the next years in a state, where the Arpanet was 50 years ago. Instead of transmitting classical bits, the quantum internet would transmit quantum bits (qubits), a superposition state of zero and one, which would lead to fundamental new applications. Prominent examples are large-scale modular quantum-computers [Monroe et al., 2014] or long-baseline telescopes [Gottesman et al., 2012]. A quantum network of clocks would allow much more precise measurements of phenomena like gravitational waves [Kómár et al., 2014].
Another feature of the quantum internet is physical measurable secure communication. The BB84 protocol showed first, that a quantum state, encoded in the polarization of a photon, could be used for sharing a secret key between two parties, commonly referred as Alice (A) and Bob (B) [Bennett u. Brassard, 1984]. A is sending quantum states to B, generated by a randomly chosen bases. B is measuring also in a randomly chosen

bases until enough states are transferred. They both communicate their choice of bases via a (not necessary secure) classical channel. With a subset of measurements, A and B compare the outcome. By statistics, the can reliably detect an eavesdropper. With Quantum Key Distribution (QKD), the problem of a secure key distribution can be solved. This enables encryption techniques like one-time pad, which can't be cracked due to a unique key usage.

Usually, the quantum state is send via a bosonic channel (photons in free space or in fibers). The development of a scalable technology, which connects several of theses channels via nodes to a quantum network remains an outstanding challenge. So far, QKD-networks have been only realized by trusted nodes with fibers (like the SECOQO QKD network in Vienna [Peev et al., 2009]), where the security remains critically on the integrity of the node stations. If they are infiltrated by an eavesdropper, the security can not be ensured anymore. Another disadvantage is that they don't allow the transmission of a quantum state over several nodes, which makes them available only for secure commutation, but not for further quantum applications like sharing entanglement for distributed quantum computer.

In the free space approach for QKD, the satellite Micius was launched to the lower earth orbit in 2017 [Liao et al., 2017]. One year later, an intercontinental video chat between Vienna and Beijing was demonstrated, partly secured with QKD [Liao et al., 2018]. The covered distance of 7600 km on earth is far away from anything else realized so far. With satellite-based QKD, the number of trusted nodes can be dramatically reduced, but the security is still based on the trust to the satellite (or in the words of the mastermind Pan Jianwei behind the project: "The satellite knows everything." [Castelvecchi, 2018]).

Compared to the free space version, the usage of optical fibers for a quantum network is attractive due to their high abundance and the commercial standard for communication. Large submarine optical data cables handle more than 95 % of IP voice and data traffic between countries and 100 % of the international internet traffic [Coffey, 2014]. The wavelength used for transporting classical information in these fibers is in the infrared range. One example is the telecom C-band, which lays with 1.55 µm inside a wavelength valley, which features very low losses (see 1.1). Despite this, the signal must be amplified by repeater stations, which are usually separated by a distance of about 60 km [Coffey, 2014].

Transporting quantum information through optical fibers relies on the the successful transmission light on the level of single photons. They are affected by the losses and noise due to scattering, sketched in figure 1.1, which lead to dephasing or complete loss of the quantum states. Tekeoka, Guha and Wilde have shown, that with a channel

transmittivity of η, the secret key rate is limited to $log_2[(1+\eta)/(1-\eta)]$ bits per mode per channel [Takeoka et al., 2014]. The TGW bound leads to an exponentially decreasing key rate with length of the channel. Because of the no-cloning theorem, which states that it is impossible to create an identical copy of an arbitrary quantum state [Wootters u. Zurek, 1982], it is not possible to use classical repeater stations for the quantum channel.

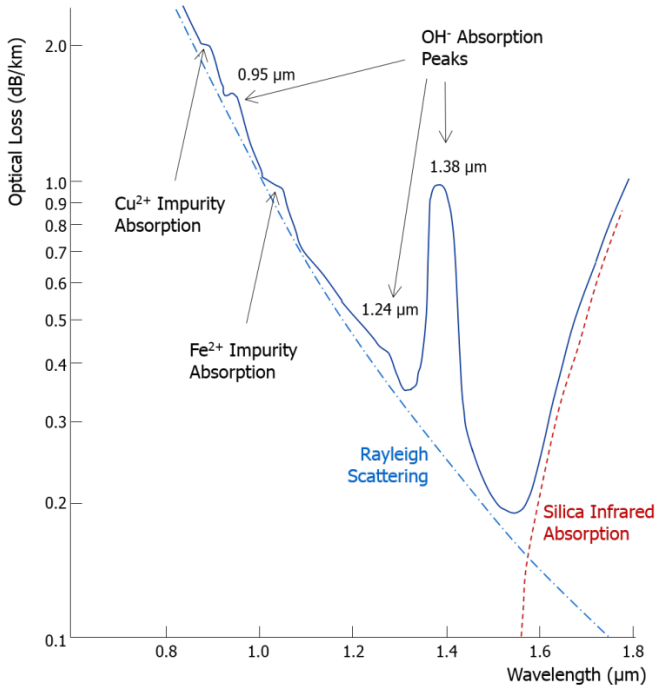

Figure 1.1.: Fiber losses vs wavelength from Clesca [2017]. Several effects in fibers contribute to the wavelength dependent losses: intrinsic absorption by the fiber material like the infrared absorption band of silicon dioxide (SiO_2) in red, extrinsic impurity ion absorption, for example by a small abundance of copper or iron ions and hydroxide ions (OH^-) from water dissolved in glass. The most light is loss due to Rayleigh scattering caused by small-scale fiber homogeneity compared to the light wavelengths [Clesca, 2017].

One way to overcome this limit for long distance communication is the quantum repeater Briegel et al. [1998]. The function principle is sketched in fig. 1.2. The distance between Alice and Bob is divided into segments, with quantum memories at each node. An entangled pair of photons, also called EPR pair (Einstein-Podolsky-Rosen), is generated by a source between the nodes. This pair is used to entangle two adjacent memories with each other, by a Bell State Measurement (BSM). The joint quantum measurement ends up with a segment, where the entanglement is stored in each quantum memory. In the next step, the outer repeater nodes fulfill an entanglement swapping operation on

their memories, by readout of the quantum state in the BSM. In that way, entangled pairs can be consecutively created in more distant nodes, until Alice and Bob end up with an shared entangled pair in their quantum memory. The entangled pair can then be used for different applications of Quantum Information Processing (QIP) like QKD using the Ekert protocol [Ekert, 1991].
With the protocol invented by Briegel et al. [1998], the exponential scaling overhead can be transformed into a polynomial. Furthermore, error correction protocols can be used to distill an entangled pair with high purity from several pairs with imperfect entanglement [Bennett et al., 1996].
From the Briegel et al. [1998] quantum repeater protocol, following building blocks can be identified [Pfister et al., 2016]: (1) an efficient interface between a flying qubit and a long lived stationary memory. The quantum memory must by accessed by a narrow, photostable, transition to generate indistinguishable photons [Machielse et al., 2019]. (2) quantum logic operations on the memory, (3) quantum error correction [Terhal, 2015] and (4) a frequency conversion to transform the photons used for transmission to a telecom wavelength with lower attenuation, like the C-band around 1.55 µm (see fig. 1.1).

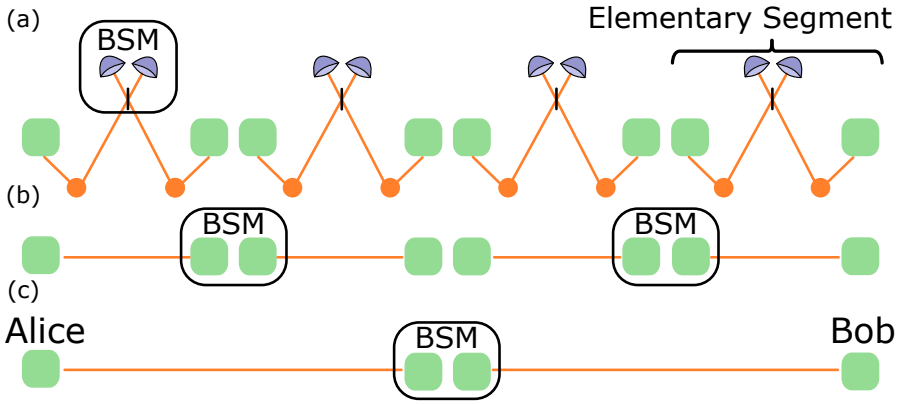

Figure 1.2.: Principle of the quantum repeater. Alice wants to share an entangled quantum state with Bob. Their distance is separated into several segments, for which lengths difference the fiber (orange line) has high enough transmission efficiency. (a) Entanglement is generated between two neighboring nodes, consisting of two quantum memories (green round box), by a pair of entangled photons from an EPR source (orange circles). One of the photon is send to the quantum memory and the other one to a Bell State Measurement (BSM). In that way, each segment is successively entangled. (b) Then the two memories at the nodes swap consecutive their entanglement by a measurement in the Bell basis. (c) In the end, an entangled pair is created, stored in each quantum memory of Alice and Bob.

This thesis is part of the Q.Link.X collaboration[1], which aims to realize a demonstrator of a quantum repeater, to overcome the TGW bound. The project is divided into an theory group for the analysis and simulation of different protocols and three experimental platforms. Each of them focus on building up a demonstrator by an elementary, fiber-based node [Luong et al., 2016], which can connect two segments (see 1.2). The quantum memories of the central node in the middle allows to generate entanglement asynchronously in each of the segments.
The realization of the node is done by three different experimental approaches: quantum dots [Song et al., 2016], trapped ions or atoms [Ritter et al., 2012] and color centers in diamond. Blocks of a quantum repeater on the last basis has been demonstrated. Examples are the deterministic entanglement of two Nitrogen Vacancy Center (NV) spins, separated into two 2 m distant cryostats [Humphreys et al., 2018] or the quantum frequency conversion of single photons from a NV to telecom wavelength [Dréau et al., 2018].
The diamond platform is split into two sub-systems, one for NV and one for Negatively charged Silicon Vacancy Center (SiV^-). The SiV^- demonstrator platform should be realized in Mainz. As a first step toward a quantum repeater node, an efficient interface between photons and the stationary qubit can be aimed. The quantum memory can be the SiV^- electron spin [Sukachev et al., 2017] or a nearby ^{13}C or ^{29}Si nuclear spin [Metsch et al., 2019].
Due to the high index of refraction of diamond, the extraction efficiency in a commonly used confocal microscope is diminished due to total internal reflection at the diamond surface. This problem can be solved by following different paths. One way is to use a solid immersion lens, which is milled into the diamond substrate Jamali et al. [2014], or a parabolic reflector [Wan et al., 2018]. The methods restrict the flexibility, because a single color centers needs to be placed at the right position.
Another approach is to bring the SiV^- into an optical cavity, which enhances the emission into a well-collectible mode. The coupling of spontaneous emission into the resonator mode is quantified by the Purcell factor. As figure of merit for a strong coupling, three main criteria must be met: (1) The emitter needs to have a stable, narrow linewidth. (2) A high quality factor (or high finesse) of the cavity. (3) Low mode volume of the cavity mode, to which the emitter is resonant.
These conditions can be fulfilled by a nanophotonic crystal cavity, where a one-dimensional lattice structure of air holes is fabricated into a freestanding single-crystal diamond waveguide by electron beam lithography and etching. Zhang et al. [2018] showed with

[1] online: `https://qlinkx.de/`

such a design, a 10-fold lifetime reduction of the SiV^- and a high collection of the excited state emission into the cavity mode. Very recently, Nguyen et al. [2019b] demonstrated with a diamond nanocavity a nearly deterministic interface between photons and the SiV^- electron spin with millisecond long SiV^- spin coherence times below 100 mK. The SiV^--cavity coupling features a high coorperativity. Coupling to a ^{13}C nuclear spin with a nearly second long coherence time is shown [Nguyen et al., 2019b]. With photonic crystal cavities, q-factors higher than 10^4 and a mode volume $< 0.6\ [\lambda/(n = 2.4)]^3$ are reached [Nguyen et al., 2019a].
These devices have the disadvantage of inhomogenously broadened linewidth of the emitter due to nanofabrication-induced strain or the SiV^- proximity to surface. The detuning of crystal cavities is less flexible, because nitrogen gas needs to be flown into the setup to shift the cavity resonance to the red. The gas is condensing into the crystal, which changes the index of refraction. To prevent freezing, the dilution refrigerator needs to be heated to higher temperatures. The blue-detuning is achieved by irradiating the device with a broadband laser [Nguyen et al., 2019a]. The outcoupling of light from the nanocavity is done by a waveguide structure with a tapered end, where a tapered optical fiber is attached (see fig. 1.3 (b)). The fragile part can break after repeated fiber coupling attempts, limiting the device lifetime [Nguyen et al., 2019a].
Instead of nanofabrication of the SiV^- environment, a other approach is to bring SiV^- into an optical cavity. Here experiments with NV and SiV^- have been also realized. Kaupp et al. [2016] showed Purcell-enhanced emission from single NV in nanodiamonds at room temperature by a fiber-based microcavity with a mode volume of 1.0 λ^3. Coupling of single NV in a diamond membrane to a miniaturized microcavity is shown by Riedel et al. [2017] at 4 K, achieving an quality factor of 58500 and enhanced emission into to the Zero Phonon Line (ZPL) from the usual 3 % to 46 %. Both have shown a reduced lifetime of the NV.
For the case of SiV^- in nanodiamonds, Benedikter et al. [2017] demonstrated an effective Purcell Factor of 9.2 for single SiV^- in nanodiamonds with a reduced lifetime of 32 %, which is measured in a fiber-based microcavity with a quality factor of 19000 (see fig. 1.3 (c)). By a similar cavity desgin, Häußler et al. [2018] couple an ensemble of SiV^- in an approx. 200 nm thick diamond membrane. The finesse drop due to additional losses from the membrane is negligible. Both experiments are performed at room temperature.

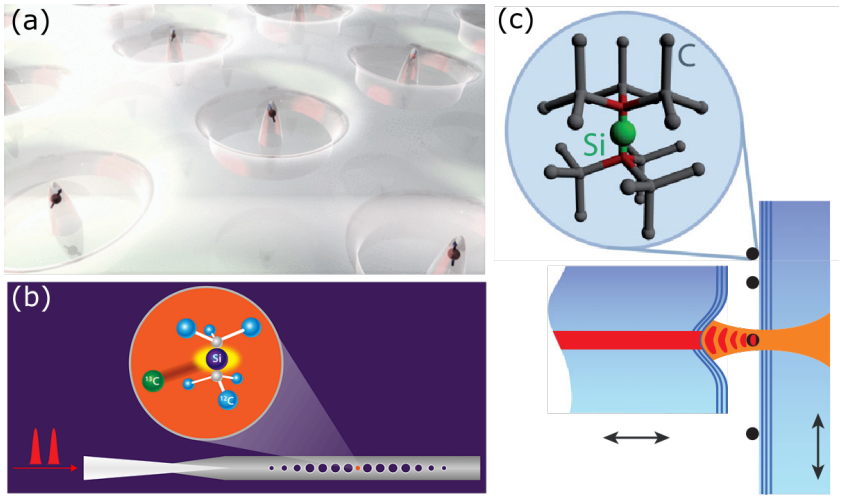

Figure 1.3.: Enhancing the collection efficiency from color centers in diamond. (a) from Wan et al. [2018]: efficient extraction from NV by a monolithic parabolic reflector pattern, incorporated by electron-beam lithography and reactive-ion etching. (b) from Fu [2019] and Nguyen et al. [2019b]: diamond photonic nanocavity coupled via a waveguide structure to a tapared fiber. The nanocavity enhances the emission from a single SiV^-, which can be coupled to a ^{13}C nuclear spin in close proximity. (c) from Benedikter et al. [2017]: nanodiamonds containing single SiV^- coupled to a fiber based microcavity.

Scope of this Thesis

The goal of this thesis is to accomplish the coupling of SiV^- in a diamond membrane to a microcavity at room temperature and to investigate, if the coupling can be still maintained at lower temperatures. For reaching theses temperatures, the experimental insert, which carries the microcavity and coupling optics was integrated into a dilution refrigerator. The work starts with a first characterization of properties of the bare microcavity (chapter 4) at room temperature and at lower temperatures. After receiving the diamond membrane sample with implanted SiV^-, the hybrid cavity system of air part and diamond part is examined (chapter 5). Ensembles of SiV^- are coupled to the microcavity at room temperature and at temperatures down to 4 K. The Purcell effect from the microcavity is shown by a reduced lifetime (chapter 6).

2

Theory

In Neolithic times, diamond was used to polish stone axes, while nowadays, in the "second quantum revolution", it becomes very attractive for applications in QIP [Aharonovich et al., 2011b]. The transparent diamond receives its color from atomic or molecular impurities or imperfections in the crystalline structure.
Over 500 of the so called color centers have been found, while only a part of them features a bright and stable emission [Aharonovich et al., 2011a]. The most prominent defect in diamond is the NV, with a spin coherence time close to one second [Bar-Gill et al., 2013]. Other color centers have been investigated in the last years with vacancy centers formed by group-IV elements like germanium [Iwasaki et al., 2015], tin [Iwasaki et al., 2017] and silicon. This thesis concentrates on the last one, the SiV^-*, whom basic properties are introduced in the first section of this chapter. The theory of the second ingredient of the experiment, the optical microcavity, is presented in the second section. In the last section, both parts are meet in the interaction between light and matter.*

2.1. The Silicon Vacancy Center in Diamond

Diamond is a solid form of pure carbon in a crystalline structure (lattice structure left of fig. 2.1) with extraordinary properties like its hardness, transparency or thermal conductivity which are used in many industrial applications like cutting or polishing. Under ambient conditions, diamond is chemical inert to organic solvents or acids, which makes the material attractive as well for application in biology [Schirhagl et al., 2014]. The electronic structure features a wide indirect band gab $\Delta E_i = 5.5$ eV, which allows the formation of lots of different color centers. Diamond has a high index of reflection $n_D = 2.4$ for visible light.

This introduction of the SiV^- follows the thesis of Becker [2017]. If two adjacent carbon atoms along the (111) direction in the diamond host lattice are substituted by a silicon atom, a silicon vacancy center is formed in the center (right of fig. 2.1). It can exist in two different optically active states with ZPL at 737 nm (1.68 eV) as the negatively charged SiV^- [Clark et al., 1995] and 946 nm as the neutral defect SiV^0 [D'Haenens-Johansson et al., 2011]. This thesis concentrates only on the much brighter SiV^- due to the very low quantum efficiency of the SiV^0 [Rose et al., 2018].

The fluorescence spectra of a defect in a solid state matrix like diamond differentiate to that of an isolated atom, because of the coupling to the crystalline environment by phonons (quantized vibrations of the host lattice or the defect itself). Purely electronic transitions without phonons are denoted to the ZPL, where transitions with the creation or annihilation of phonons are assigned to a red- or blue-shifted Phonon Side Band (PSB). The ratio of light emitted in the ZPL and PSB is described with the Huang-Rhys factor S, which indicates the number of phonons involved in the transition and is calculated by [Neu et al., 2011]:

$$DW = \exp^{-S} = \frac{I_{ZPL}}{I_{ZPL} + I_{PSB}} \tag{2.1}$$

I_{ZPL} and I_{PSB} are the intensities of the ZPL and PSB, DW is the Debye-Waller factor. For QIP applications, a strong and photostable ZPL is important to operate with a robust optical qubit and in generating entanglement. In contrast to the negatively charged nitrogen vacancy center NV, most of the SiV^- emission is concentrated into to ZPL with a weak red PSB over 100 nm.

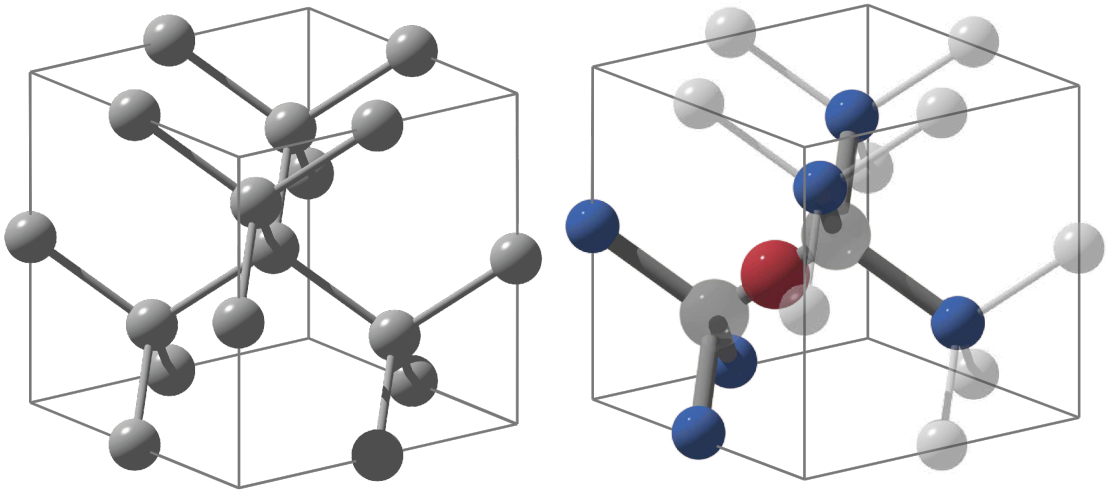

Figure 2.1.: Diamond lattice and physical structure of the SiV^- from Becker [2017]. *Left:* Tetrahedral structure of carbon atoms (in gray) forming a cubic diamond unit cell. *Right:* Sketch of the diamond lattice hosting the SiV^- in a split-vacancy configuration with D_{3d} symmetry. The interstitial silicon atom (drawn in red) is sitting in the center between two vacant neighboring lattice sites. The six nearest-neighbor carbon atoms are drawn in blue.

The Huang-Rhys factor for the SiV^- is in the range between S = 0.29 and S = 0.13 in nanodiamonds [Neu et al., 2011], which also coincide with the value in bulk diamond [Dietrich et al., 2014]. This means that 75-88 % are emitted into the ZPL (Debye-Waller factor), which changes only slightly at lower temperatures [Dietrich et al., 2014].
At room temperature, the SiV^- fluorescence in bulk diamond features a strong ZPL peak at 738 nm with a linewidth between 1 nm and 5 nm depending on the crystal environment. For a strongly strained host diamond, e.g. observed in nanodiamonds, the ZPL can be shifted over a wide range between 730 nm and 750 nm [Neu et al., 2011]. If the SiV^- is cooled down to lower temperatures, the ZPL starts to split into a doublet at about 100 K, which splits again below 50 K, first observed by Sternschulte et al. [1994] and Clark et al. [1995] (shown in fig. 2.2). The so emerging four line structure at Liquid Helium (LHe) temperature, is blue-shifted by about 1 nm to 737 nm. In high quality diamonds for temperature < 20 K, the linewidth of the four peaks become narrower as a linear function with falling temperature, until they reached their lifetime limited linewidth of several 100 MHz at 4 K [Rogers et al., 2014b]. For temperature > 70 K, a cubic dependence of linewidth and temperature was measured in Jahnke et al. [2015].
SiV^- can be built up from all three stable silicon isotopes, namely ^{28}Si,^{29}Si and ^{30}Si , which appear in a natural abundance of (92.22,4.69,3.03)% [Clark et al., 1995; Jahnke,

2015]. The intensity scales with the abundance, so the main signal comes from SiV^- made of ^{28}Si. For LHe temperature, an identical, but weaker four peak structure, which is red-shifted of the two other isotopes can be observed [Clark et al., 1995].
From now on, the four peaks of the SiV^- are labeled A-D with increasing wavelength like in the literature. The peaks can be assigned to four transitions in the electronic levels of the SiV^- [Jahnke et al., 2015], lifted by spin orbit coupling, dynamical Jahn-Teller interaction and crystal strain, which depend on the diamond quality. The excited state branch is split by 259 GHz, while the ground state branch splits by 48 GHz, see fig. 2.3.

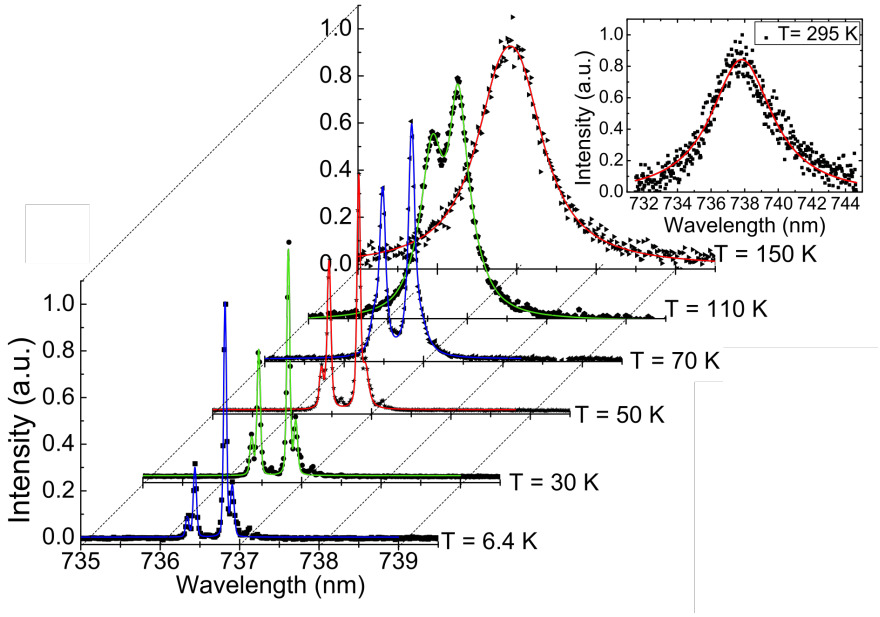

Figure 2.2.: Spectrum of the SiV^- at room temperature and at lower temperature from Neu et al. [2013]. Temperature dependent fluorescence of SiV^- ensemble in a homoepitaxial, high-quality, low-stress diamond film, produced by chemical vapor deposition (CVD). The single peak at room temperature splits into four narrow peaks at LHe temperature. The insert shows a room temperature spectrum. Excitation with 532 nm laser light.

The transition rates from the excited to the ground state doublets (lifetime of the excited state) has a temperature dependence. Jahnke et al. [2015] measured a linearly increasing excited state lifetime for temperatures above 50 K, reaching about 1 ns at room temperature. Below 50 K, the lifetime saturates at a level of $\tau_{5K} = 1.7$ ns.
A magnetic field lifts the degeneracy of the spin orbit levels by Zeeman splitting.
Theses Zeeman sublevels can be used as a qubit. For application in QIP, the initialization is necessary, which can be done by splin-flipping lambda transitions or optical pumping into a Zeeman sublevel. State readout is possible due to the long-cycling spin-conserving

transitions. Rogers et al. [2014a] and Pingault et al. [2014] showed optical manipulation of this electronic spin including initialization, readout and coherent preparation. With coherent population trapping, they prepared a dark superposition state with a spin coherence time T_2^* in the nanosecond range at 4 K. This is limited by orbital relaxation because of phonon processes [Jahnke et al., 2015].

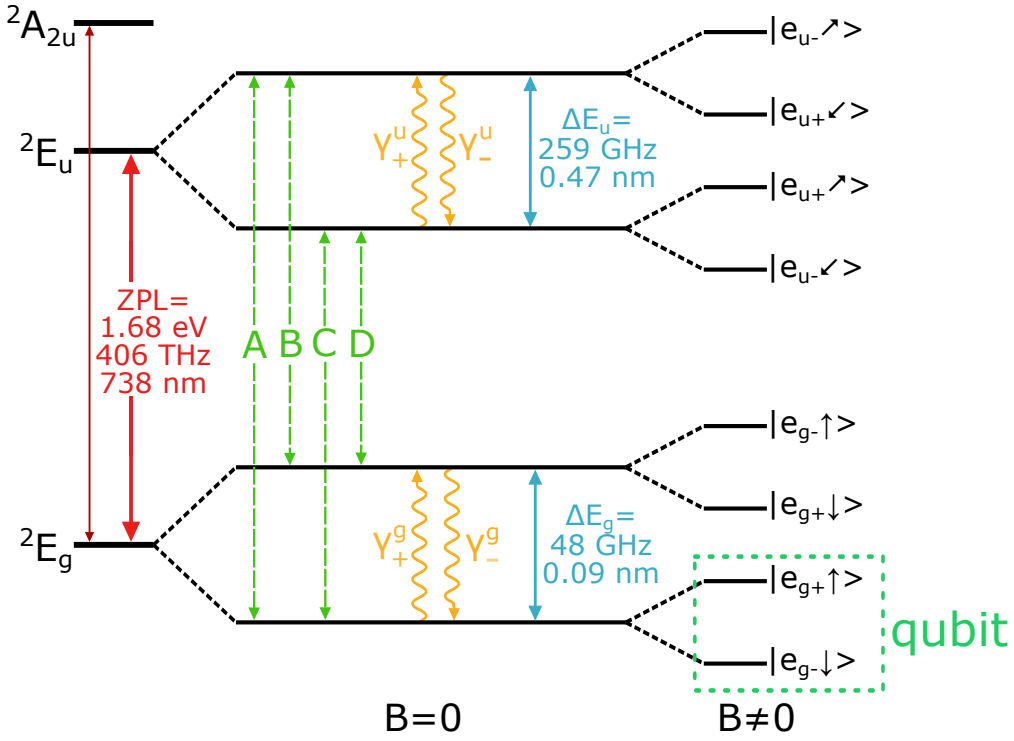

Figure 2.3.: SiV^- level scheme: The dipole transition at 738 nm connects a ground state ^2E_g and excited state ^2E_u. A second rapidly decaying excited state $^2A_{2u}$ is at 605 nm. The degeneracies of the ground and excited states are lifted by spin-orbit coupling, Jahn-Teller interaction and potentially crystal strain. The four transitions A-D are revealed at lower temperature as four peaks, shown in figure 2.2. An external magnetic field lifts the degeneracies of the electronic spin levels by Zeeman interaction. $\gamma^{g/u}_{+/-}$ denotes the phonon transitions between the branches of the ground and excited doublet. The sublevel of the lower ground state can be used as a qubit.

Different techniques are used to overcome this limit, for example by engineering the strain environment by a nano-electro-mechanical system [Sohn et al., 2018] or the fabrication of periodic nano-structrues to construct a phononic band gap at the phonon transition frequency [Tao et al., 2014]. Another method is to cool the diamond to much lower temperatures, which reduces the orbital relaxation by lower phonon occupation (temperatures according to the splitting of the orbital states are shown in 2.3). Operat-

ing at 100 mK, Sukachev et al. [2017] demonstrated with single-shot spin readout fidelity of 89 % and sequences of dynamical decoupling a spin coherence time of $T_2^* = 13$ ms. To achieve this long coherence time, hyperfine interactions between the spin qubit and the surrounding nuclear spin bath have to be suppressed. For that, high quality diamond is needed (low abundance of nitrogen and boron) and a low concentration of ^{13}C isotopes with a nuclear spin [Balasubramanian et al., 2009].

Width and Shape of Spectral Lines

In general, a transition of an emitter from an excited level (energy E_e) to a ground state (energy E_g) leads to a peak at the frequency ν_0 in the electromagnetic spectrum: $E_e - E_g = h\dot{\nu}$. The Full Width at Half Maximum (FWHM) of the peak is denoted as linewidth $\delta\nu$. No transition is perfectly monochromatic due to different broadening mechanisms, depending on the lifetime of the emitter excited state and the environment. The mechanism can be separated into two classes. The homogeneous broadening, where all individual emitters are equally affecting the lineshape. On the other hand for inhomogeneous broadening, all emitters behave individually and contribute differently to the spectrum.

The excited state of an emitter has a specific lifetime, determined by the transition rate 2.15 from the upper to the lower level. With the energy-time uncertainty principle, a minimum lifetime τ can be related with the linewidth: $\delta\nu = \Delta E/h \geq \tau^{-1}$ [Fox, 2006]. If no other effects occur, an emitters linewidth is only broadened to the natural lifetime (lifetime limited linewidth $\delta\nu_\tau = \tau^{-1}$). The lifetime is the same for all emitters (neglecting environmental influences), so it is a homogeneous broadening effect, leading to a Lorentzian shaped linewidth.

The emission spectra of emitters inside crystalline or amorphous solids depend on it's quality and purity. They can undergo a non-radiative transition, where no photon is emitted. These transitions shorten the lifetime, which leads to homogeneous broadening of the linewdith [Fox, 2006]. The emission spectrum is also affected to the interaction with the local environment. If this is not entirely uniform, each emitter sees a different surrounding, which leads to inhomogeneous broadening of the emitters ensemble linewidth (environmental broadening). In diamond, the color centers are subject to local strain of the host material, which broadens and shifts the ZPL [Lindner et al., 2018].

2.2. Optical Cavities

An optical cavity is composed of two highly reflecting mirrors (reflectivity R, transitivity T) separated by a length d, which are acting as a resonator for an electromagnetic light wave. The high reflectivity can be archived by a Distributed Bragg Reflector (DBR) mirror coating. The cavity is resonant for a certain wavelength, if a whole-number ratio of half the wavelength is fitting into the length between the two mirrors [Saleh u. Teich, 2008].

$$d = q \cdot \frac{\lambda}{2} \quad with \quad q \in \mathbb{N} \tag{2.2}$$

This can be explained in a picture, where several interfering light beams are bouncing back and forth between the mirrors. All beams are interfering constructively for the right wavelength, a standing wave is formed and the resonator is transparent for the light. The nodes of the standing wave are associated with longitudinal modes of the light field (also called fundamental modes q).
Light with a wavelength that does not match to the lengths is reflected from the incoupling mirror. The reflected I_r and transmitted intensity I_t can be expressed with the Airy functions [Demtröder, 2013](I_t plotted in 2.4). They depend on the phase ϕ, which the light picks up inside the resonator, the incoupled light I_0 and the reflectivity of the mirrors by the finesse coefficient $F = \frac{4R}{(1-R)^2}$:

$$I_r(\phi) = I_0 \frac{F \sin^2(\phi/2)}{1 + F \sin^2(\phi/2)} \qquad I_{(t)}(\phi) = I_0 \frac{1}{1 + F \sin^2(\phi/2)} \tag{2.3}$$

The frequency periodicity of called the longitudinal modes is the Free Spectral Range (FSR), which is calculated with the refractive index n of the medium filling the cavity:

$$FSR_\nu = \nu_{q+1} - \nu_q = \frac{c}{2n\,d} \tag{2.4}$$

The cavity linewidth, defined as $\delta\nu = \nu_1 - \nu_2$ for the transmitted intensities $I(\nu_1) = I(\nu_2) = \frac{1}{2} I(\nu_q)$ can be calculated by the Airy function [Riehle, 2006]:

$$\delta\nu = \frac{2FSR_\nu}{\pi\sqrt{F}} = FSR_\nu \cdot \frac{(1-R)}{\sqrt{\pi}R} \tag{2.5}$$

The ratio of FSR and linewidth is named finesse, an important parameters which quantifies the spectral resolution of the cavity. The finesse is determined by the losses and also a gauge for the amount of interfering beams inside the resonator. Including losses L from scattering and absorption in the coating or mirror substrate, the condition $1 = \mathrm{R}+\mathrm{T}+\mathrm{L}$ has to be fulfilled due to energy conservation. With a symmetric coating for both mirrors (for a high reflecting mirror, $\sqrt{R} \approx 1$ can be assumed for the last recast), the finesse can be expressed as [Meschede, 2008]:

$$\mathcal{F} = \frac{FSR_\nu}{\delta\nu} = \frac{\pi\sqrt{R}}{1-R} = \frac{\pi}{T+L} \tag{2.6}$$

In the particle picture of light, the optical resonator stores a photon for a lifetime τ before it escapes through the output mirrors. This is described by the quality-factor (Q-factor) of the cavity, which relates the stored energy to the energy loss per cycle [Saleh u. Teich, 2008]:

$$Q_{cav} = \frac{\nu\mathcal{F}}{FSR_\nu} = \frac{2nd}{\lambda}\mathcal{F} = \frac{\nu}{\delta\nu} = \frac{2\pi\nu}{\kappa} \tag{2.7}$$

So cavity linewidth and the lifetime of the photon are related. 2.7 also introduced the photon loss rate κ of the cavity:

$$\tau = \frac{1}{2\pi\delta\nu} \qquad \kappa = \frac{1}{\tau} = 2\pi\delta\nu = \frac{\pi c}{4\mathcal{F}d} \tag{2.8}$$

2.2.1. Plano Concave Cavity

If two plane mirrors are used to construct an optical resonator, the mirrors would have to be placed exactly parallel to raise a standing wave inside, which is the case, if the propagating light in the resonator reproduces itself in every circulation between the mirrors. For stable resonators, it is therefore more common to use concave mirrors, to ensure a spatial confinement. Defining the g-parameter as $g_i = 1 + d/ROC_i$, where ROC_i is the reflectivity of one of the mirrors ($i = 1, 2$), the cavity is stable if the equation $0 \leq g_1 g_2 \leq 1$ is satisfied [Saleh u. Teich, 2008]. Two plane mirrors represent the lower limit while the upper limit is reached for two curved mirrors with a distance of $d = -(ROC_1 + ROC_2)$. Increasing d leads to to non confined light field and the resonator becomes unstable.

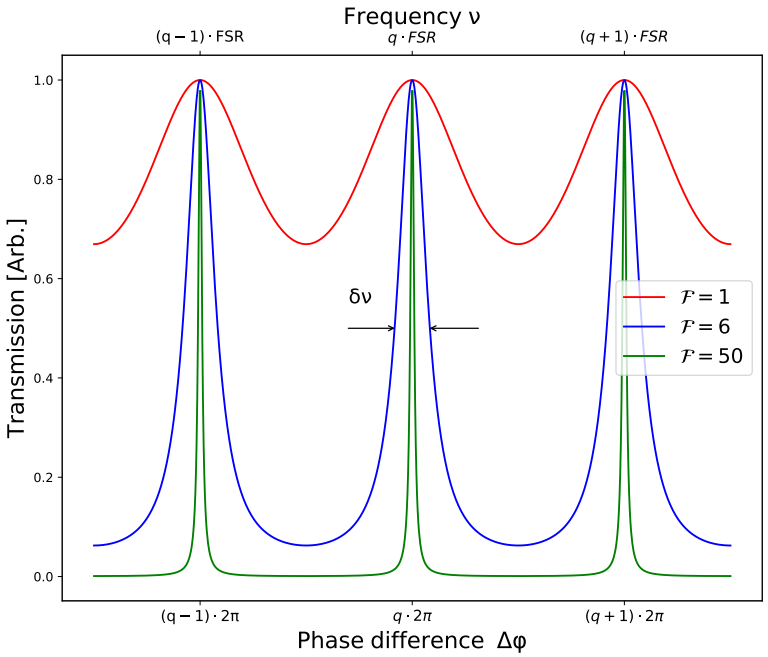

Figure 2.4.: Plotted Airy function I_t, describing the transmission of an optical cavity. Frequencies of a whole-number ratio of the FSR can pass the cavity with a linewidth of $\delta\nu$, determined by the finesse $\mathcal{F}$. The linewidth is defined as the FWHM of the intensity and becomes narrower for increasing finesse values.

The longitudinal modes of a cavity with curved mirrors are described by a Gaussian beam, which has an intensity distribution of a Gaussian shape at every position along the propagation axis and a minimum beam width in the focus point, called the beam waist with width $2 \cdot \omega_0$. However this is not the only solution for the paraxial Helmholtz equation, describing the propagation of a electromagnetic field. Higher order transversal modes can also evolve, characterized by the Hermite-Gaussian function [Kogelnik u. Li, 1966]. The complete mode spectrum of the cavity then contains of Transverse Electromagnetic Mode $(\text{TEM})_{l,m,q}$, where q states the order of the longitudinal mode, and l, m states the roots of the Hermite-Gaussian function (the transversal modes). Their frequency can be calculated [Kogelnik u. Li, 1966]:

$$\nu_{l,m,q} = FSR_\nu \cdot (q + \frac{1}{\pi}(l + m + 1)\arccos(\sqrt{g_1 g_2})) \tag{2.9}$$

The special case for a concave mirror with radius of curvature R and a plane mirror is sketched out in figure 2.5. The beam waist ω_0, plotted in 2.6, lies on the plane mirror only as a function of the cavity lengths [Kogelnik u. Li, 1966]:

$$\omega_0^2 = \frac{\lambda}{\pi} \cdot \sqrt{d(ROC - d)} \tag{2.10}$$

The mode volume for the longitudinal Gaussian mode can be calculated by integrating the distribution of the intracavity electric field $\vec{E}(\vec{r})$ and depends also only on the geometry of the resonator [Haroche u. Raimond, 2006]:

$$V_{mode} = \frac{\int d^3r |\vec{E}(\vec{r})|^2}{\max |\vec{E}(\vec{r})|^2} = \frac{\pi}{4}\omega_0^2 d = \frac{\lambda d}{4}\sqrt{d(ROC - d)} \tag{2.11}$$

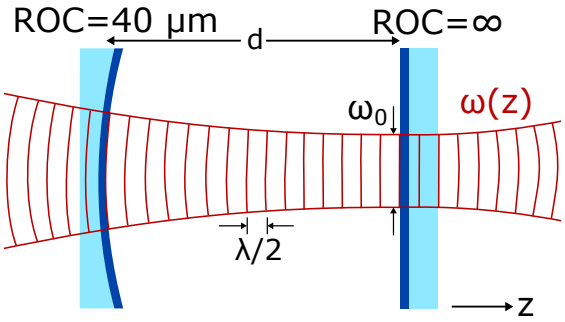

Figure 2.5.: Principle sketch of the plane concave microcavity configuration used in this thesis. The red lines represent the wave fronts of the fundamental Gaussian beam. $\omega(z)$ is the evolution of the beam width along the optical axis.

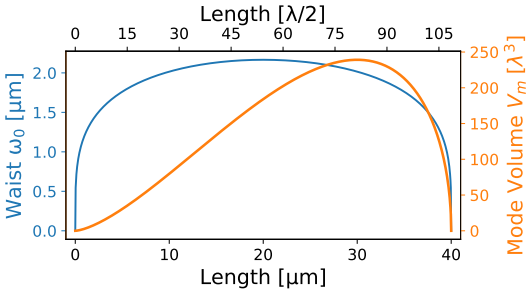

Figure 2.6.: Calculated waist (2.10) and mode volume (2.11) of the microcavity. The two parameters are only determined by the geometry of the cavity, expressed by the Radius of Curvature (ROC) of both mirrors. Here is ROC = 40 µm.

2.2.2. Coupled System of Air and Diamond Cavity

Incorporating a diamond membrane with thickness t_d into the microcavity by bonding it to the plane mirror side leads to a a system of two coupled cavities [Riedel, 2017]. The air gap has a length of $t_a = d - t_d$, while the membrane acts like an additional layer on the DBR stack of the plane mirror with refraction index n_d. The mode structure can be described by an one-dimensional model with anticrossing between air-confined and diamond-confined modes. Janitz et al. [2015] showed that the resonant wavelengths of a fundamental mode with order q for the complete system can be calculated:

$$\lambda_q \approx \Big(2\pi(t_a + n_d t_d)\Big)\left\{q\pi - (-1)^q \times \arcsin\left[\frac{n_d - 1}{n_d + 1}\sin\left(q\pi\left[\frac{t_a - n_d t_d}{t_a + n_d t_d}\right]\right)\right]\right\}^{-1} \tag{2.12}$$

For the ideal case, where the membrane-air interface is perfectly reflective ($n_d \to \infty$), the system splits into two separate cavities, where the normal modes would separate into "diamond" modes (dashed green lines in 2.7) and "air" modes (dashed orange line in 2.7). The electric field is then completely localized in the diamond or air cavity [Janitz et al., 2015]. For a finite n_d, the modes are coupled, which results in a avoided crossing in th spectrum:

- **"diamond-like" modes** have a shallow slope (see 2.7 (a) for 630 nm), length variation has a relative small impact on the resonant wavelength and the electric field is mostly concentrated in the diamond membrane

- **"air-like" modes** have a steeper slope (see 2.7 (b) for 630 nm), length variation has a strong impact on the resonant wavelength and the electric field is mostly concentrated in the air gap [Riedel, 2017]

The avoided crossing can be understood by considering the nodes of the standing waves inside the coupled system [van Dam et al., 2018]. The diamond-air interface present for the air gap a step in the refraction index from low value in air ($n_a \approx 1$) to a high value in diamond ($n_d = 2.41$). This results in a field with antinode at the interface. For the diamond cavity, its the opposite, the field has a node at the interface [van Dam et al., 2018]. In the end, the electric field at the interface has to be continuous for the coupled system, so this leads to anti-crossing with hybridized modes described by formula 2.12.

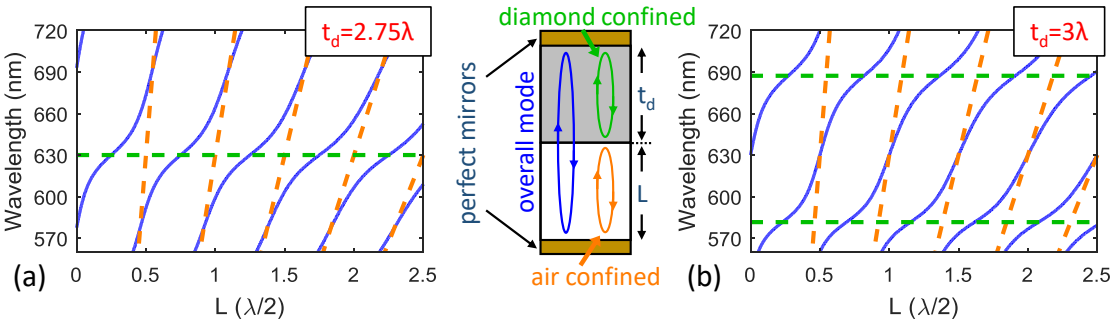

Figure 2.7.: Coupled system of air and diamond cavity from Riedel [2017]. Different diamond thickness lead to a "diamond-like" cavity mode at 630 nm (a) or a "air-like" mode (b), colored in solid blue. The dashed green line show the resonances only for the diamond (independent of cavity length) while the dashed orange line correspond to the resonances, which evolve in the air cavity, linearly increasing with the cavity length.

2.3. Light Matter Interaction

Bringing an emitter inside an optical resonator can lead to an enhancement of the emission by coupling to one mode of the resonator, which has to be resonant with the radiative transition of the emitter. This section follows the book of Fox [2006]. For the sake of convenience, the emitter is treated as a two-level system with excited and ground state, which transition frequency is resonant to the cavity. The relative strength of the coupling is described by three important parameters:

- photon decay rate of the cavity: $\kappa = 2\pi\delta\nu$
- spontaneous decay rate of the emitter γ
- emitter-photon coupling $g_0 = \left(\frac{\pi\mu_{eg}^2\nu}{\epsilon_0\hbar V_{mode}}\right)$

The emitter-photon coupling is determined by the electric dipole interaction energy between emitter and cavity vacuum field, calculated by the cavity mode volume 2.11 and the dipole moment μ_{eg} of the transition. The first parameter, the decay rate of photons out of the cavity is defined by the Q-factor of the cavity $\kappa = \frac{2\pi\nu}{Q}$. The spontaneous decay rate accounts for the emission into non-cavity modes. Depending on the time-scale for the dynamics of the composed system of emitter and cavity, one can define two regimes.

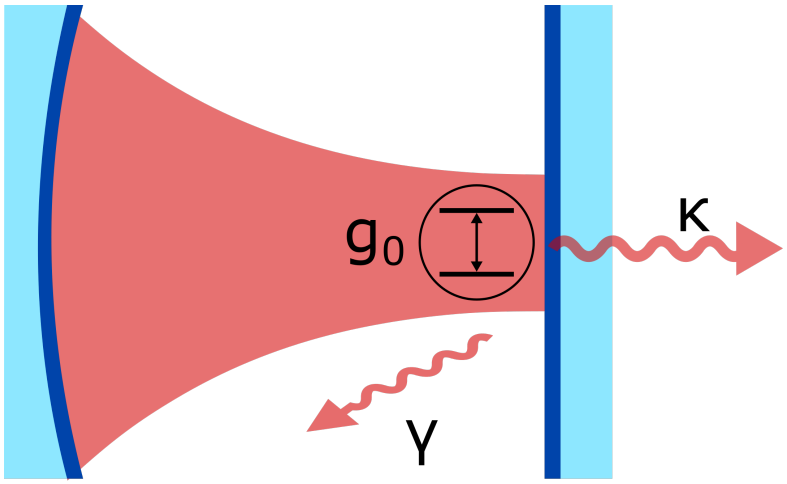

Figure 2.8.: Two level system inside a plano concave optical resonator.

Strong Coupling ($g_0 \gg \kappa, \gamma$)

In the strong coupling regime, g_0 between emitter and photon is large compared to the losses. If this condition is satisfied, the photons interacting with the emitter in a reversible way. Due to the low losses, the emitted photon into a resonant cavity mode can travel several times between the mirrors and then be re-absorbed by the emitter. So the time scale for this process is faster than losing it from the mode. The theory of cavity quantum electrodynamics (CQED) describes this regime of reversible interaction. The Jaynes-Cummings model explains the interaction of a two-level atom with a single quantized mode of a light field. The Hamiltonian is composed of a contribution of the atom, the light field of the cavity and an interaction term between both. If the coupling is switched on, the electric-dipole interaction of atom and photon lifts the degeneracy leading to dressed states. In this regime, a emitter state can be coherently mapped to a photon [Albrecht, 2014].

Weak Coupling ($g_0 \ll \kappa, \gamma$)

Here, the non-coherent losses are much larger then the coupling. Photons are lost before they can re-interact with the emitter (irreversible process). The emitter then decays with an increased rate compared to the free space emission, which is calculated in the next section.

2.3.1. Spontaneous Emission and Purcell Enhancement

The relatively small cavity influence in the weak coupling regime can be quantified by perturbation theory. Considering Fermi's golden rule, which describes the transition from a initial state (excited state e) to an final state (ground state g) under a certain perturbation (coupling of the emitter's dipole moment μ_{eg} to the vacuum field E_{vac}), the emission rate into free space and into a single cavity mode can be calculated. With the density of final states ρ_{free} and the transition matrix element $M_{i\to f}$, the transition rate is:

$$W_{free} = \frac{2\pi}{\hbar^2}|M_{e\to g}|^2\rho = \frac{2\pi}{\hbar^2}|\mu_{eg}E_{vac}|^2\rho_{free} \tag{2.13}$$

With the density of states for photon modes in free space (surrounding homogeneous medium V_0, which cancels out and vacuum permittivity ϵ_0) and the electric field amplitude of vacuum fluctuations at frequency ν:

$$\rho_{free}(\nu) = \frac{4\nu^2 V_0}{c^3} \qquad |E_{vac}|^2 = \frac{\hbar\pi\nu}{2\epsilon_0 V_0} \tag{2.14}$$

The vacuum fluctuations are randomly oriented to the dipole moment of the emitter, so averaging over all possible orientations leads to a factor of $\frac{1}{3}$. The transition rate of spontaneous emission into free space, can be calculated by putting 2.14 into 2.13:

$$W_{free} = \frac{1}{\tau_R} = \frac{\mu_{eg}^2 (2\pi\nu)^3}{3\hbar\epsilon_0\pi c^3} \tag{2.15}$$

The emitter is introduced into a single-mode cavity, where $V_0 = V_{mode}$ accounts for the corresponding mode volume. The density of final states inside a cavity (with linewidth $\delta\nu$ and resonant frequency ν_c) is described by the Lorentzian function:

$$\rho_{cav}(\nu) = \frac{1}{\pi^2\delta\nu}\frac{\delta\nu^2}{4(\nu-\nu_c)^2+\delta\nu^2} \tag{2.16}$$

A similar formula like in 2.13 can be taken for the electric dipole matrix element, where the cavity is included:

$$M_{e\to g,cav}^2 = \zeta^2\mu_{eg}^2 E_{vac}^2 = \frac{|\vec{\mu_{eg}}\cdot\vec{E}|}{|\vec{\mu_{eg}}||\vec{E}|}\mu_{eg}^2 E_{vac}^2 = \zeta^2\frac{\mu_{eg}^2\hbar\pi\nu}{\epsilon_0 V_{mode}} \tag{2.17}$$

The factor ζ take accounts for the overlap of the emitter's dipole with the position of the maximum electric field. By putting 2.16 and 2.17 into Fermi's golden rule, the emission rate into the cavity mode can be obtained:

$$W_{cav} = \frac{2\pi}{\hbar^2}|M_{e\to g,cav}|^2\rho_{cav} = \frac{2\mu_{eg}^2}{\hbar\epsilon_0 V_{mode}}\cdot\frac{\nu}{\delta\nu}\cdot\zeta^2\cdot\frac{\delta\nu^2}{4(\nu-\nu_c)^2+\delta\nu^2} \tag{2.18}$$

The two emission rates into free space and into a cavity mode can be compared. This is done by the Purcell factor F_P, named after Edward Mills Purcell, who discovered this effect in the 1940s [Purcell, 1995]. Because of the relation between emission rate and

radiative lifetime, the Purcell factor expresses the ratio of excited state lifetime in free space τ_R^{free} and inside the cavity τ_R^{cav}.

$$F_P = \frac{W_{cav}}{W_{free}} = \frac{\tau_R^{free}}{\tau_R^{cav}} = \frac{3c^3}{4\pi^2 V_{mode} \cdot \delta\nu \cdot \nu^2} \cdot \zeta^2 \cdot \frac{\delta\nu^2}{4(\nu - \nu_c)^2 + \delta\nu^2} \tag{2.19}$$

If the cavity is resonant with the emitters transition between excited state and ground state $\nu = \nu_c$, the last term in 2.19 vanishes. With the definition for the quality factor 2.7 and finesse 2.6 of a cavity and taking account of the index of refraction n of the medium filling the cavity, the Purcell factor can be written as:

$$F_P = \frac{3\zeta^2 Q(\lambda/n)^3}{4\pi^3 V_{mode}} = \frac{6d\zeta^2(\lambda/n)^2\mathcal{F}}{4\pi^2 V_{mode}} = \frac{3(\lambda/n)^2}{2\pi} \cdot \frac{\mathcal{F}}{\pi} / \left(\frac{\pi}{4}\omega_0^2\right) \tag{2.20}$$

In the last recasting of formula 2.20, the mode volume of the hemispherical mirror arrangement 2.11 is assumed. By writing the formula in this shape, the Purcell enhancement can be interpreted, that the absorption cross section of the emitter (first term) is increased by a factor of $\mathcal{F}/\pi$, which equals to the number of circulations of a photon inside the cavity [Riedel, 2017].
Large F_P requires high finesse (larger Q-factor), a small mode volume and a well orientated electric dipole parallel with the cavity mode. For Purcell factors $F_P > 1$, the spontaneous emission rate is faster and the lifetime of the emitter is reduced. On the other side, a slower emission rate with suppressed emission is reached for $F_P < 1$. The large density of states provided by the cavity leads to the enhanced emission rate. Or for the off-resonant case, an absence of modes results in the suppressed emission.
Another parameter, the β-factor (spontaneous emission coupling factor) describes the ratio of emission into the cavity versus the total emission:

$$\beta = \frac{W_{cav}}{W_{cav} + W_{free}} = \frac{F_P}{1 + F_P} \tag{2.21}$$

For the weak coupling regime, two sub-regimes are identified. One is the bad cavity regime, where the losses from the cavity are higher than the non-resonant decay: $\kappa > \gamma \gg g_0$. The other one is the bad emitter regime, which is met, when the losses are dominated by spontaneous emission into modes not supported by the cavity: $\gamma > \kappa \gg g_0$. The emitter linewidth is broadened compared to the cavity linewidth and the coupling is independent of the cavity decay rate κ [Albrecht, 2014]. The emission is then more affected by the properties of the cavity. In formula 2.20, this can be accounted by an effective Q-factor [Benedikter et al., 2017]:

$$Q_{eff} = (Q_{cav}^{-1} + Q_{em}^{-1})^{-1} \tag{2.22}$$

Q_C considers the Q-factor of the cavity 2.7 and $Q_{em} = \lambda/\delta\lambda$ represents the Q-factor of the emitter, obtained by its linewidth $\delta\lambda$. For solid state emitters, the branching ratio into the ZPL, determined by the Debye-Waller factor DW 2.1, also influences the emission into the cavity mode. To account this, the formula of of F_P has to be multiplied with DW.
Additionally, a nonradiative decay rate of the emitter has to be considered. The quantum efficiency is defined as the ratio of radiative decay rate γ_r and summed radiative and nonradiative decay rate γ_{nr}:

$$QE = \frac{\gamma_r}{\gamma_r + \gamma_{nr}} \tag{2.23}$$

For a $QE < 1$, as expected for SiV^- [Neu et al., 2012], the lifetime reduction changes to (with F_P from eqn. 2.20 and the Debye-Waller factor 2.1) [Benedikter et al., 2017]:

$$\frac{\tau^{free}}{\tau^{cav}} = F_P \cdot DW \cdot QE + 1 \tag{2.24}$$

3

Experimental Setup

This chapter gives an overview about the complete setup for the microcavity experiments. It can be divided into an optical part, where the lasers are controlled, connected by a fiber network to the cryostat with the experiment (first section of this chapter). The cryostat includes the experimental insert with the microcavity and light collection optics (second section of this chapter). The microcavity is provided by David Hunger's group from the Karlsruher Institute of Technology. The diamond membrane sample was produced, annealed and applied to the mirror by Nadarajah Athavan in Steven Prawer's group at the University of Melbourne, while implantation was done by Michael Kieschnick in Jan Meijer's group at the University of Leipzig. All steps from fabrication to application to mirror are explained (last section of this chapter). Furthermore, a quick summary of spectroscopy by confocal microscopy done by Morgane Gandil in the group of Christoph Becher from the Saarland University is shown.

3.1. Overview: Cryogenic Laboratory

The complete setup is sketched in figure 3.1. A grating stabilized red Diode Laser (DL) (Toptica DL Pro with a detuning range of 726-741 nm) for on-resonant excitation and characterization of the microcavity and a solid-state green laser (MGL-III-532) for off-resonant excitation. The DL can be frequency stabilized to a low-finesse reference cavity, the wavelength is measured by a Wavemeter (HighFinesse WS6-200). The red light is passing a polarization beam splitter to observe the reflection signal of the microcavity on a Photo Diode (PD) (Newport 1801). The polarization of the red light is controlled by a half-wave and a quater-wave plate. With the quater-wave plate, the laser light is circularly polarized, so that the reflection light traveling in the opposite direction passes the polarization beam splitter to the PD. Both lasers are coupled to a Polarization Maintaining Fiber (PM) (Schäfter+Kirchhoff PMC-630, 7 m), which guides the light to the fiber breakout box (picture in appendix A.4) on top of the cryostat. This home-built box contains all ends of the five fibers, which are installed inside the cryostat and connecting both sides of the microcavity (table of fibers in appendix B). The fibers are going through a press seal to a flexible tube, which is connected to an access port of the cryostat insert. In the cryostat insert (picture A.7), the fibers are glued (by GE low temperature vanish) to the stages to end at the level of the experimental insert. The fiber installation is described in detail by Stahl [2018]. In that way, the fibers connecting optics and experimental insert, can be disconnected to move the cryostat insert in and out of the cryostat dewar by a motor on the sailing.
Another advantage of the fiber breakout box is, that additional external lasers can be very easily integrated to the system by fiber coupling. A compact braodband light source, which is power stabilized (Thorlabs SLS201L, emission spectrum in A.10), can be fiber coupled to the microcavity by a Multimode Fiber (MM) (Thorlabs FG105LVA, 1 m) to probe the microcavity with white light. Furthermore, a diode laser from another laboratory (home-built, frequency stabilized Rubidium Doppler laser) can be used to characterize the microcavity with 780 nm laser light. A 25 m long fiber (Thorlabs SM630) is used to connect both laboratories. A pulsed green laser (PicoQuant PDL 800-D) for lifetime measurements is also fiber coupled through this box.
The experimental insert with the microcavity is cooled down by a He^3-He^4 dilution refrigerator (Oxford Kelvinox 100) with a base temperature of 23 mK (tested without experimental insert) and a cooling power of 100 µW at 100 mK. The dilution operation is carried out in the cryostat insert (A.7), where every stage is cooling to a lower temperature until the mixing chamber at the lowest level reaches base temperature. The

mixing chamber is in direct contact to the experimental insert, to conduct the heat load most efficiently. The experimental insert and the lowest stage with mixing chamber is protected by a 50 mK shield from thermal radiation. In addition the whole insert is closed to an Inner Vacuum Chamber (IVC). The cryostat can be cooled to 77 K by filling Liquid Nitrogen (LN) and 4 K by filling LHe. By pumping the 1-K pot, a temperature of about 1 K can be achieved. For lower temperatures, the mixture of He^4 and the much rarer He^3 is used. Three sensors are used to measure a temperature inside. Two of them are placed at the highest level, where the 1-K pot and an absorption pump is mounted (measuring a range of 4-250 K and mK to 6.5 K) and the third one is placed at the lowest level next to the mixing chamber (measuring from mK range up to 6.3 K). All temperature sensors are read out by the gas handling system (Oxford IGH). The cryostat dewar contains the Outer Vacuum Chamber (OVC) and an LN shield to minimize the LN/LHe evaporation rate from its main bath. For operation at cryogenic temperatures, the IVC is pumped to high vacuum. The insert is immersed to liquid nitrogen (77 K) or liquid helium (4 K). A small amount of helium is used as contact gas to prevent the buildup of ice and ensure thermal contact of the diamond sample with the surrounding bath.

The detection path can be chosen for the purpose of the measurement. The microcavity transmission light is observed by a PD (Thorlabs PDA36A-EC) with a high gain to amplify weak signals. For measuring spectra, the light is coupled into a fiber (by a MM, Thorlabs FG105LVA, 1 m) to a spectrometer (Andor Shamrock 500i with Andor iDus 420A CCD camera, performance in A.8). For the time correlated lifetime measurement, the fluorescent light is guided by a MM (Thorlabs FG105LVA, 7 m) to the detection setup, which contains a Avalanche Photodiode (APD) (Perkin Elmer SPCM-AQR). The light can be filtered by several spectral filters (table in appendix C) and is focused by a lens to the active area of the APD. The detection setup can by extended by a 50:50 beam splitter and a second APD (Excelitas SPCM-AQRH) to measure time correlations for the detection of single emitters. The APD are read out by a data acquisition card (National Instruments Card SCB-68) or a time-correlated single photon counting system (PicoQuant PicoHarp 300).

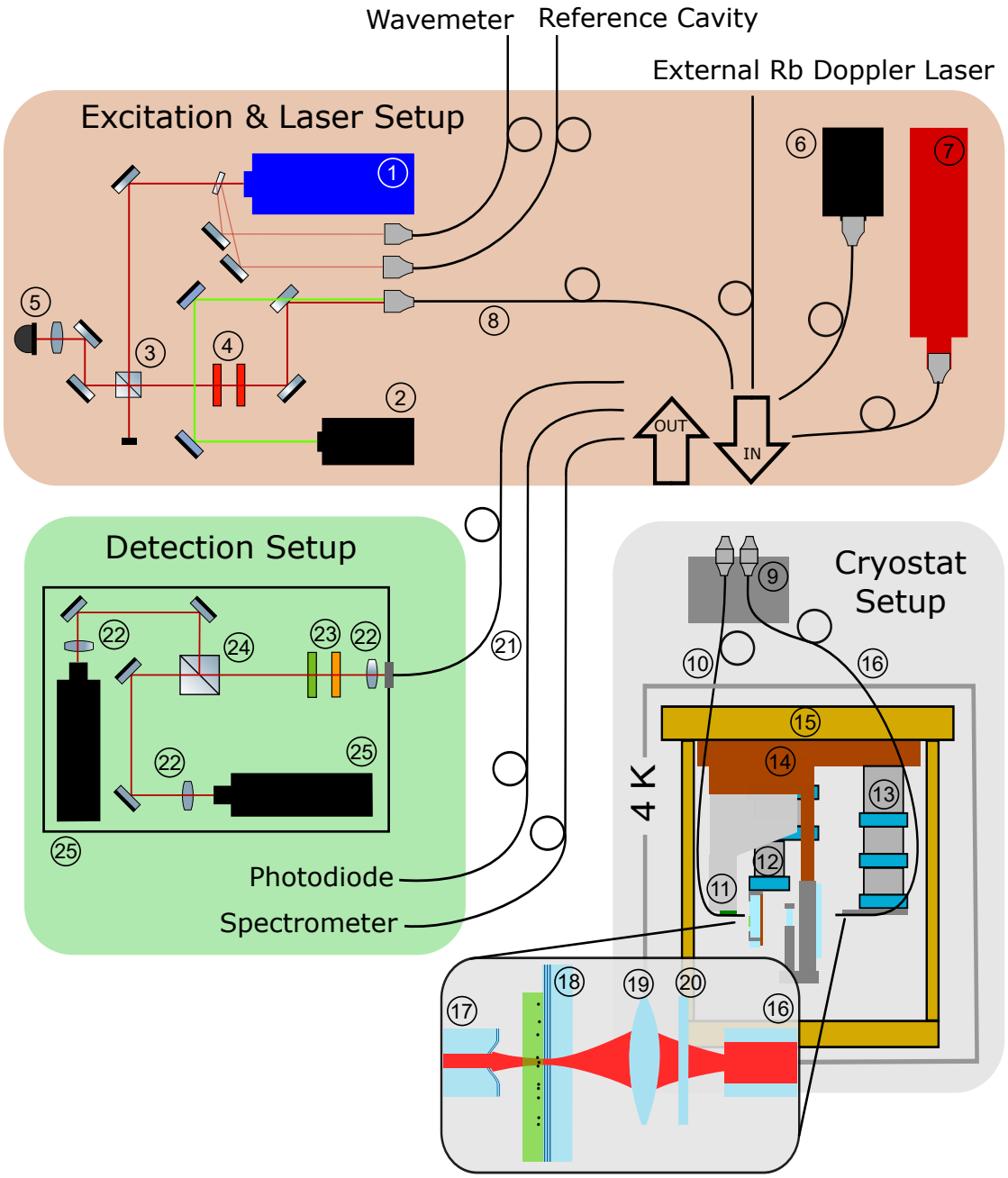

Figure 3.1.: Overview of the complete setup: (1) DL, (2) green solid-state laser, (3) polarizing beam splitter, (4) polarization control, (5) PD, (6) pulsed green laser, (7) broadband light source, (8) PM transfer fiber, (9) fiber breakout box, (10) PM to P4 in tab. A.2, (11) locking piezo, (12,13) 3D nanopositioner stack, (14) experimental insert, (15) cryostat baseplate, IVC, (16) MM to P1 in tab. A.2, (17) microcavity Singlemode Fiber (SM), (18) microcavity macroscopic mirror, (19) aspheric lens, (20) longpass filter, (21) MM transfer fiber, (22) collimation optics, (23) optical filters (C), (24) 50:50 non-polarizing beam splitter, (25) APD.

3.2. Experimental Insert with Microcavity

The heart of the experiment is the experimental insert, which carries the microcavity with the coupling optics and devices for spatial control. It is screwed to the lowest stage of the cryostat insert to sit directly below the mixing chamber. The microcavity is a plano-concave Fabry-Pérot cavity, consisting of a SM fiber (IVG Cu600) with a concave end facet and a half inch mirror. Both parts have a symmetric DBR coating (Laseroptik Garbsen, details in appendix A.8) with maximum reflection at 736 nm. The fiber end was shaped in the group of David Hunger, details of the micro-fabrication method can be found in Hunger et al. [2010] and Hunger et al. [2012]. The fiber end has an ultra-low surface roughness of about 0.2 nm in silica, which is achieved by a CO_2 laser pulse train, which evaporates the material and creates a low-viscosity melt layer on the surface. In that way the fiber end has a Gaussian profile, where the center can be approximated by a sphere with a ROC of 40 µm (interferometric measurement in appendix A.9), which is milled in a plateau on the fiber tip, which is 25 µm in diameter. In that way the microcavity length is less restricted by the lateral dimension of the fiber. The other end of the SM fiber is spliced to a PM fiber (Thorlabs PM630-HP) which is guided through the cryostat insert to the fiber breakout box.

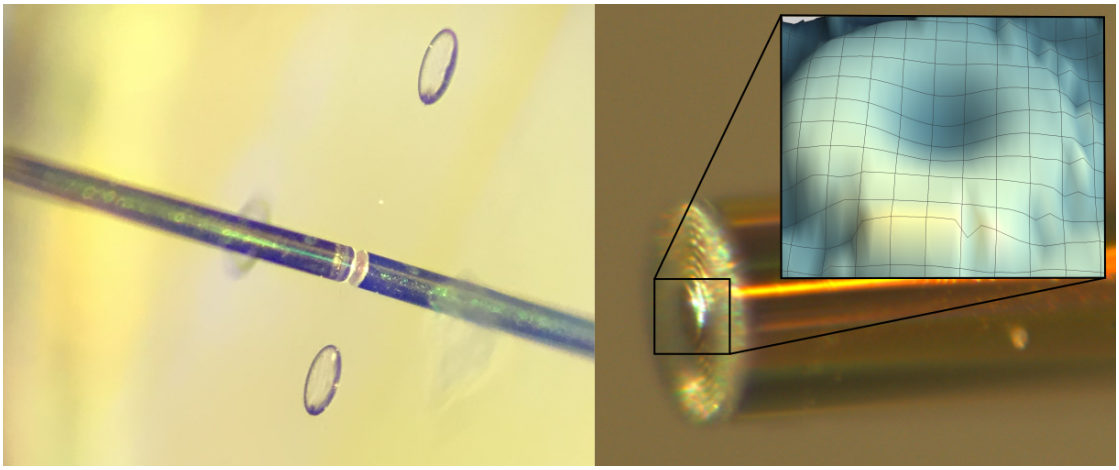

Figure 3.2.: *Left:* Light microscope image of the microcavity. The SM fiber is on the left side, reflected by the mirror, which holds the diamond membrane samples (two of the four are not in the right focus). *Right:* Fiber tip with concave end on the milled plateau in the center. The microscope picture was taken from another fiber end with comparable properties to the fiber used for the microcavity. The insert shows an interferometric measurement of the Gaussian shaped fiber dimple.

The microcavity SM is mounted on a shear piezo (one layer from PI P123.03T), for short scanning (travel range of 0.5 µm) and locking of the microcavity lengths. The control voltage is set by a function generator (HP 33108) for scanning or by a digital laser locking module (Toptica DigiLock 110) for length stabilization, amplified by a compact analog voltage amplifier (Piezomechanik SVR 350-1 or TEM MiniPia 101). The mirror is held on a 3D nanopositioner stack designed for cryogenic temperatures and vacuum conditions (2 x AttoCube ANPx311/RES/LT and ANPz51/RES/LT) for length detuning and lateral positioning of the mirror. Thermal anchoring of the mirror is ensured by a braid wire connecting the mirror holder (made of copper) with the copper part of the experimental insert, which is in direct contact with the mixing chamber.
Optical access from the mirror side of the microcavity is provided by a MM, which is focused by an aspheric lens (Thorlabs N414-B with 3.3 mm focal length). Its end is cleaved and glued to a stainless steel holder, which is screwed to a second 3D nanopositioner stack (2 x AttoCube ANPx101/RES/LT, ANPz102/RES/LT, made of beryllium copper). In that way, the MM fiber position can be optimized to the fixed position of the lens. A second cleaved fiber (Thorlabs PM460-HP) is also glued to the holder to couple in green light from the mirror side. Both fibers are connected to the fiber breakout box. For the detection of the SiV^- fluorescence, it was essential to introduce a longpass filter (Edmund Optics LP650), which cuts at 650 nm, between lens and fiber end to prevent the green excitation light to enter the detection part (see fig. 3.3 right). In this configuration, the optical path is fixed by the position of the SM and the lens, while the diamond membrane sample on the mirror can be laterally placed into the microcavity waist.
The nanopositioners and the locking piezo are connected by copper wires, which are thermally anchored to every stage, to a vacuum tight feedthrough connector (Fischer connector) at the top of the cryostat insert. Details of the wire installation in the cryostat can be found in Stahl [2018]. The six nanopositioner axes are controlled by a closed loop piezo controller (AttoCube ANC350), which provides a micrometer precise position resolution and a stepper function for spatial control over several millimeters. The piezo offset of one axis of the mirror stack, which controls the coarse microcavity length, can be changed to a BNC input by a selfmade electronic switch box, to scan the microcavity length with an analog voltage ramp.
The experiment is controlled with a modular laboratory experiment management suite in python, called Qudi[1]. More details can be found in Binder et al. [2017]. The program is extended by self-written code for automatic readout of devices like the nanoposition-

[1]download from GitHub: `https://github.com/Ulm-IQO/qudi`

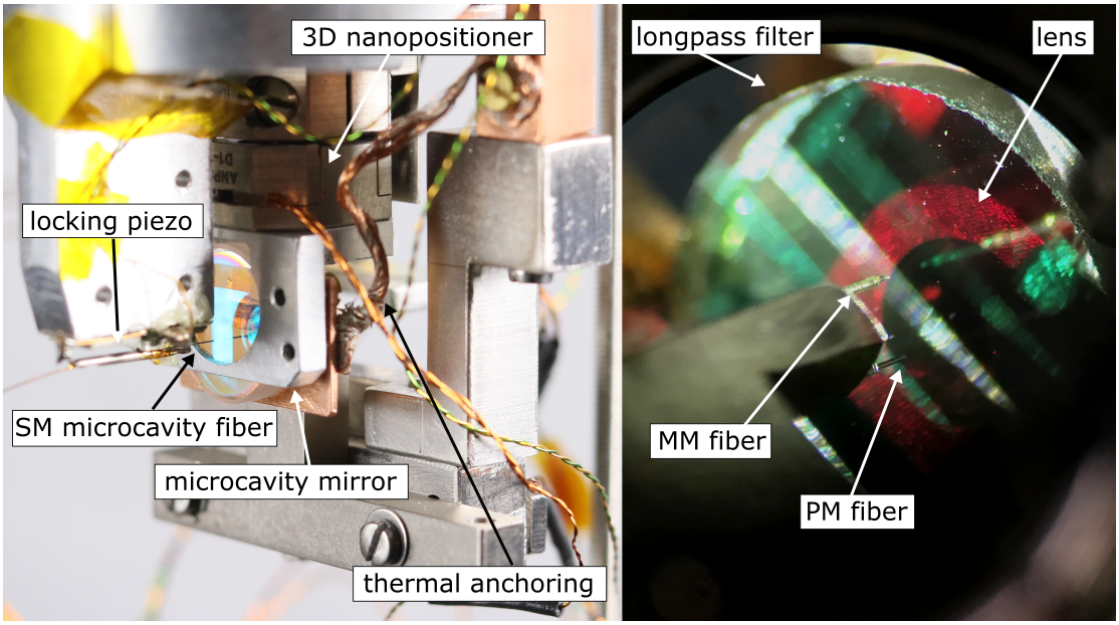

Figure 3.3.: *Left:* Image of experimental insert with the microcavity consisting of a SM fiber with concave end facet and a half inch mirror with the diamond membrane sample. The membrane is lateral positioned in the microcavity waist by a nanopositioner stage, which controls also the coarse lengths, while the stabilization is realized with a shear piezo ing the fiber. *Right:* Coupling optics for access through the mirror side of the microcavity. The light is focused with a lens (red shape in filter) to the . A longpass filter, which cuts at 650 nm, prevents green excitation light to enter the detection path.

ers, scopes or the spectrometer. In that way, automatic measurement routines can be executed like the measurement of the microcavity length or finesse. A more detailed description can be found in the appendix A.11.

3.3. Diamond Membrane Sample

The diamond membrane was produced by Athavan Nadarajah in the group of Steven Prawer, details for the fabrication can be found in Piracha et al. [2016a] and Piracha et al. [2016b]. The process starts with a single crystal diamond (SCD) slab, which is implanted with helium ions to create a thin damage layer in a depth of approximately 1.7 µm. By annealing at a temperature of 1300 °C for one hour, the amorphous layer is converted to a graphite-like carbon layer. The diamond slab is overgrown using Microwave Plasma Chemical Vapor Deposition (MPCVD) to produce a high quality single crystal layer. A diamond frame with smaller lateral dimensions then the single crystal substrate is milled

by laser cutting from another slab of diamond (single crystalline or polycrystalline) with a thickness of 150-300 µm. The geometry of the frame can be designed to create for example several windows with a round shape. In the next step, the frame is aligned to the overgrown substrate and put again into the MPCVD reactor to fusion growth both, frame and overgrown substrate. The graphite-like carbon layer is etched off and the single crystal membrane fused to the frame is lifted off. In the last step, the overgrown layer is thinned using Inductively Coupled Plasma Reactive Ion Etching (ICP-RIE) with Ar/Cl_2 to etch the damage layer. The diamond peak at 1333 cm^{-1} in the Raman spectra of the fabricated membrane show comparable characteristics as for the single crystal bulk substrate.

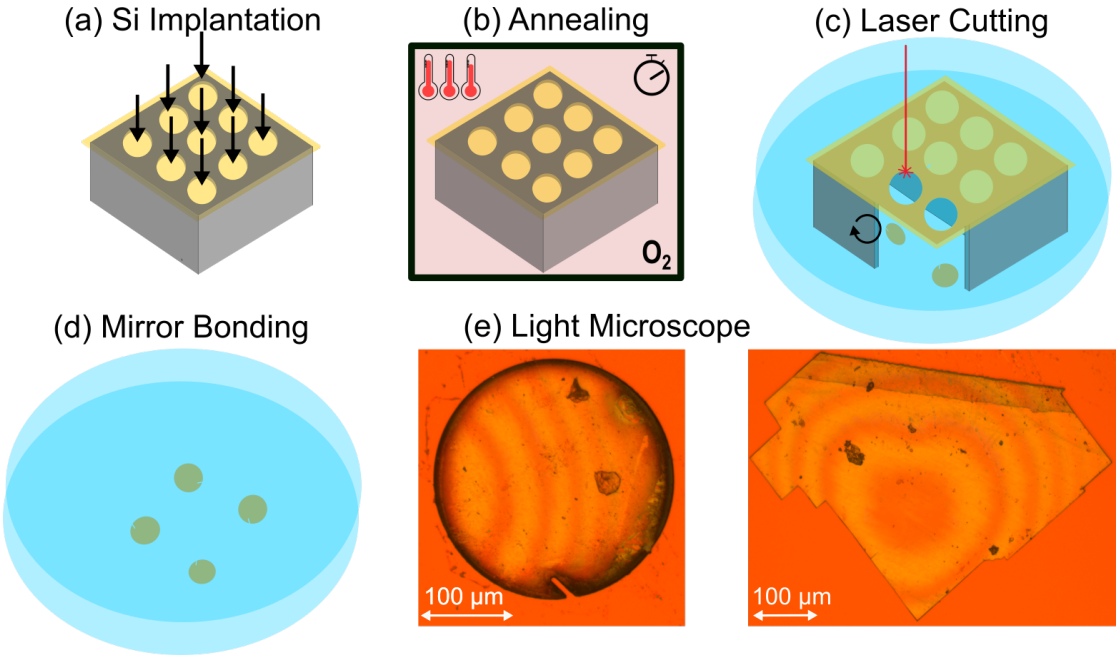

Figure 3.4.: Diamond Membrane Application Process (a): The membrane sample is implanted with silicon atoms (implantation details in A.2). (b): Annealing at different temperatures to heal up the diamond lattice and form SiV^-. (c): Cutting of the circular windows with a CO_2 laser. The membrane needs to rotate to face up the not implanted side, so that the SiV^- position matches with an antinode of the intracavity light field. (d): Membrane samples bonded to mirror. (e): Microscope image of the the (2,2) windows and the Broken Window Diamond Sample (BW) on the mirror. The edge of the window is much darker then the edge of the BW due to a layer of graphitized carbon from the laser cutting.

The fabrication method allows to create ultra-thin membrane windows of a thickness of about 350 nm to 6 µm. with single crystalline quality and low strain.
The diamond membrane sample, used in this thesis, has a thickness of (1.48 +/- 0.05)

µm (exact thickness depends on window, see table A), with nine circular windows with a diameter of 270 µm and a roughness of ≈ 5 nm. Base material is a diamond slab (type IIa, orientation (100)) and the scaffold is made of polycrystalline diamond. For easier handling, the sample is mounted on two silicon wavers (150 µ m and 500 µ m thick) with a size of 20 mm times 20 mm.
After receiving the membrane from Melbourne, it is send to the group of Jan Meijer, where six windows are implanted with silicon. Details of the implantation process can be found in Lühmann et al. [2018]. The ion energy is 110 keV to reach a target depth of 74 nm below the membrane surface simulated using SRIM. This depth is selected to match the SiV^- position with the first antinode of the intracavity light field seen from the plano concave mirror side. The silicon implantation doses in every window is varied in several steps between 10^{14} ions/cm^2 and 4.3×10^8 ions/cm^2 (see appendix A.2).
After implantation, the diamond membrane was sent back to Melbourne, where it was annealed at 1000 °C for three hours, acid cleaned for 20 minutes and O_2 annealed at 500 °C for four hours. Further confocal measurements are performed, which show in spectra the typical SiV^- and lateral different intensities due to the implantation region. In the lower implantation region, some SiV^- are blinking in the order of 20 to 150 ms (appendix A.3). Unfortunately, three membranes got broken during these measurements.
Finally, the membranes are applied to the mirror. An asymmetrical slit is laser cut into the corner of the membrane, to identify if the implanted side faces the mirror (such that the antinode of the intracavity light field matches the SiV^- depth). Three windows are cut out by a CO_2 laser over the mirror, so that they fall onto the mirror and bond to it by van der Waals forces. Additionally, a piece of the broken piece[2] is applied to the mirror with a tweezer, referred in the following as BW. The piece broke out of the membrane, so that it also includes some of the implantation spots from a regular window (first ten doses, reconstruction of the original position in A.4). It has additional implantation spots and an edge with ingrown SiV^-, which originate from silicon contamination in the fusion chamber during the fabrication process.
After first experiments with the membranes inside the microcavity, the sample is sent to the group of Christoph Becher. Unfortunately, during the shipment to Saarbrücken, two windows fell off from the mirror. The remaining samples are characterized by confocal microscopy. In broadband Raman spectroscopy at the edge of the membrane windows, the sp2 raman signal is found, which indicates that the diamond at this region is graphitized [Zaitsev, 2001]. The ZPL of the SiV^- is found at 738 nm with a room temperature linewidth of 5 nm. Also bleaching behavior is present in every implantation region and a

[2] ... which look a like a comic diamond!

flat $g^{(}2)$ correlation measurement curve (in the regions with lower implantation doses), which indicate, that no single emitters are found with the confocal microscopy. In the BW, a waveguide effect can be observed. Scattered light from the implantation spots with higher doses is also detected, when measuring at regions with lower implantation doses.

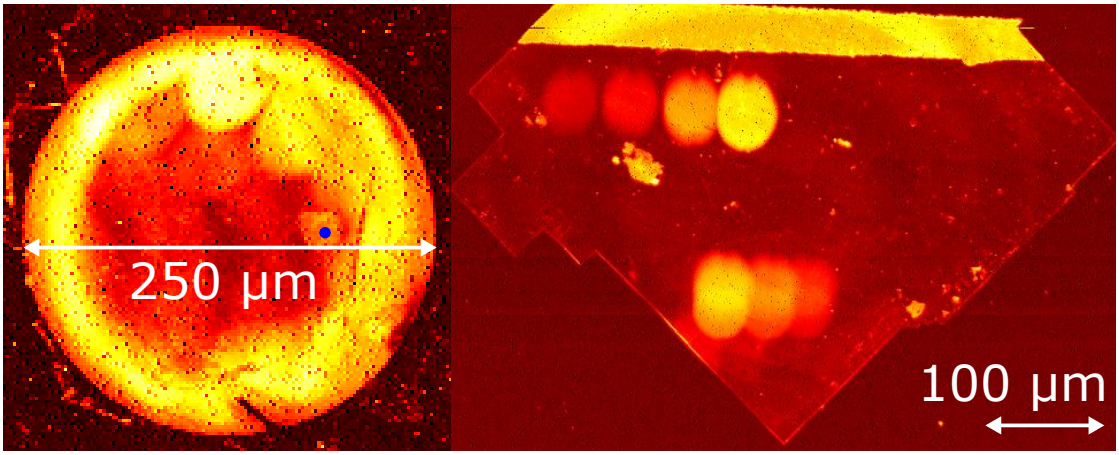

Figure 3.5.: Spectroscopy measurements performed in the group of Christoph Becher with a confocal microscope. Excitation with 520 nm laser light and detection in a range of 730-750 nm. *Left:* Photoluminescence (PL) of window (2,2) from figure 3.4 is affected by graphitized carbon from laser cutting. The implantation spots in the center are visible. *Right:* Confocal spectroscopy of the broken window piece. The implantation spots are bright in accordance to the implanted silicon doses. The upper edge includes ingrown SiV^-, which shine very bright.

4

Bare Microcavity

This chapter describes the characterization of the microcavity without any diamond sample. Parts of the measurements are performed with samples already on the mirror, but due to the large difference in magnitude (half inch mirror and membranes in the range of a few 100 µm) it is very easy to find bare positions on the mirror. After receiving the fiber and mirror from David Hunger's group, it was assembled and the microcavity was built into the experimental insert. This chapter provides a characterization of the microcavity (section 4.1) including important parameters like length, finesse and linewidth. In the second section 4.2, the behavior at cryogenic temperatures is shown, while the last section shows length stabilization at both room and cryogenic temperatures.

4.1. Characterization at Room Temperature

On of the most important properties of the microcavity is the length between fiber tip and mirror as well as the finesse, which is determined by the fiber and mirror coating and the lengths due to clipping losses. Both parameters lead to the microcavity linewidth, see formula 2.8. The length is of particular importance, because it has to be avoided to drive the fiber into the mirror, which can destroy the fiber itself or the high reflective coating layers on both sides.
The length is controlled with one axis of the nanopositioner stack (details in 3.2). The axis can be driven in the continuous stepper mode (with a frequency up to 1 kHz), to change the coarse lengths, and bring fiber and cavity mirror very close to each other. At room temperature, when the experimental insert is open, it is very convenient to monitor the fiber tip with a light microscope and control the position of the mirror before the fiber tip. As a rule of thumb, the mirror can be moved close to the fiber tip, until the reflection of the tip in the mirror is going to be blocked by the fiber itself (like in the left side of figure 3.2). The stepper are piezoelectrically driven by the controller with a sawtooth voltage, which works with a slip stick principle, while the moving table is spring-clamped at rest. The achieved expansion of each sawtooth shaped pulse to the piezo is proportional to the applied maximum voltage. In that way, the length can also be tuned by the nanopositioner axis in smaller length steps. In the single step mode with lower step voltage, very small length deviations in the nanometer range can be achieved (typical 50 nm at room temperature and 10 nm at cryogenic temperature[1]).
By applying a DC offset to an axis, either digital with the ANC controller or analog with the switch box (see 3.2), the nanopositioner can obtain a continuous sub-step-size resolution. The analog input is used to scan the axis voltage with a ramp (for traveling ranges at different temperatures, see appendix A.10).
In order to measure length and finesse with the DL, the cavity length is scanned with an analog ramp (usually 5-50 Hz, with 60 Vpp, which covers the complete travel range at room temperature). The laser is coupled in via the fiber and the transmitted light is collected by the MM behind the mirror, connected to a PD. The reflected light from the microcavity travels back through the transfer fiber to the optical setup, where it is guided to a second PD. The polarization of the laser is set with a half and quarter wave plate (see figure 3.1) and the reflected light is separated by a polarization beam

[1] details and the slip stick principle in `https://www.attocube.com/application/files/7115/5360/4699/attoPremium_Line.pdf`

splitter. The scanning ramp triggers a scope which is used to display the signal from the reflection and transmission PD, see figure 4.1.

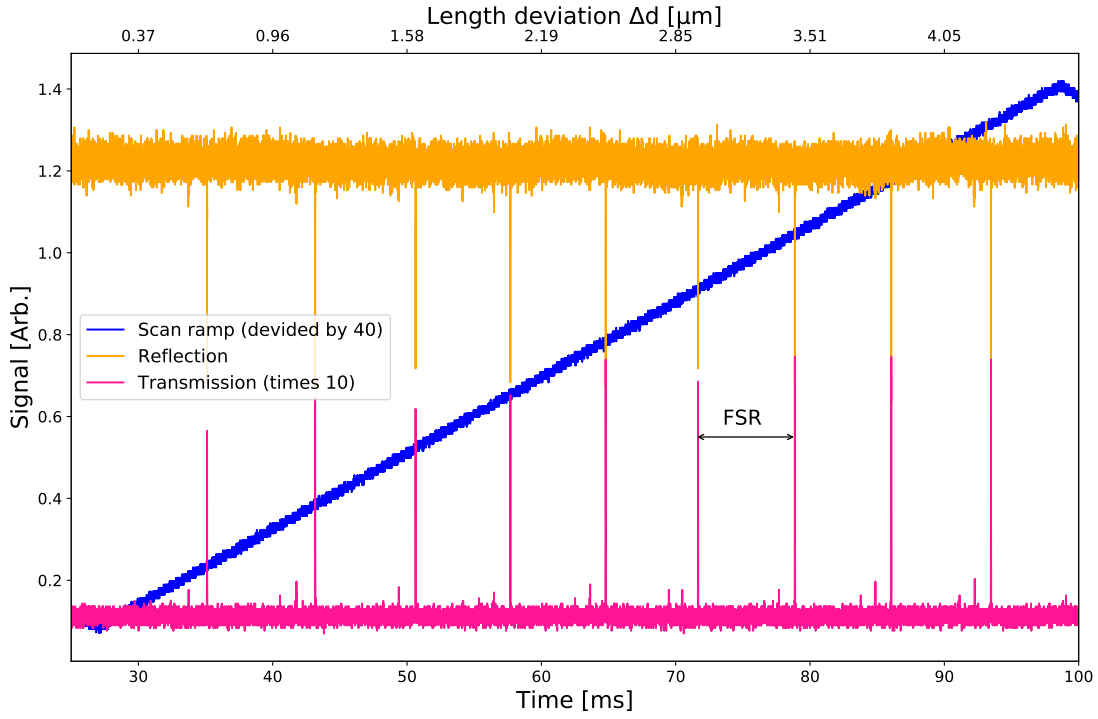

Figure 4.1.: Microcavity length scan, the relative signals are changed to fit into the same plot range. The fundamental transverse mode is visible as the highest peak/dip in the reflection/transmission signal and defines the FSR_λ in wavelength of the cavity. Beside that, some higher order transverse modes can be seen. The scanning voltage ramp can be transformed to length deviation by a calibration of the axis (see appendix A.10). The cavity is probed with the DL and the finesse at this length is F = 845.

It is convenient to scan the cavity length and determine the finesse by the recorded transmission signal (or reflection signal). This can be done, by fitting a Lorentzian function to the resonance peak, like shown in figure 4.2. The finesse is then obtained by the ratio of the gap between the peaks (the FSR) and the FWHM of the fitted Lorentzian function. By scanning over a number of resonances, the finesse can be determined by the collected statistics, neglecting a possible change in the finesse for the (small) scanned lengths.

Beside the finesse, the microcavity length must be measured in a reliable and reproducible way. There are several ways to determine the absolute length. Two possibilities are presented in the following two subsections.

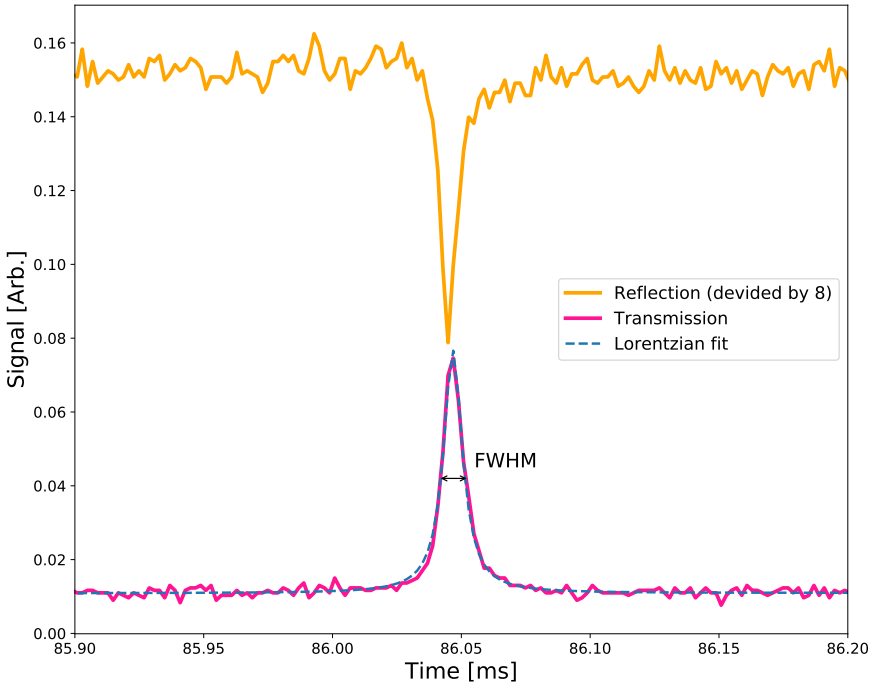

Figure 4.2.: Lengths scan over a single resonance of the microcavity in transmission and reflection. The signal corresponds to the seventh peak in figure 4.1. The transmission signal is fitted by a Lorentzian function to measure the cavity finesse by the FWHM.

Length determination by laser

In this method, the length of the microcavity is scanned, but different probing wavelengths are needed. The DL wavelength is detuned over a longer range by the grating (usually from 737 nm to 732 nm). A complete ramp is recorded for every probed wavelength to find the center positions of every peak by a Lorentzian fit. In that way, the peak positions can be set in relation to the wavelength and with the FSR, which is equal to the half of the probed wavelength, the absolute microcavity length can be calculated. At room temperature, the full offset scan range of the axis is long enough to cover several resonances (nine in 4.1). A length is calculated for every resonance and the statistical error is determined by the standard deviation.
This method suffers from scanning the offset many times, because of the nonlinear behavior of the piezo, especially in the lower voltage range (see appendix A.17) and for a ramp with negative slope. This effect is not compensated in the calculation of the length and finesse because many resonance peaks are evaluated during the measurement and the value/error are obtained by the average/standard deviation.

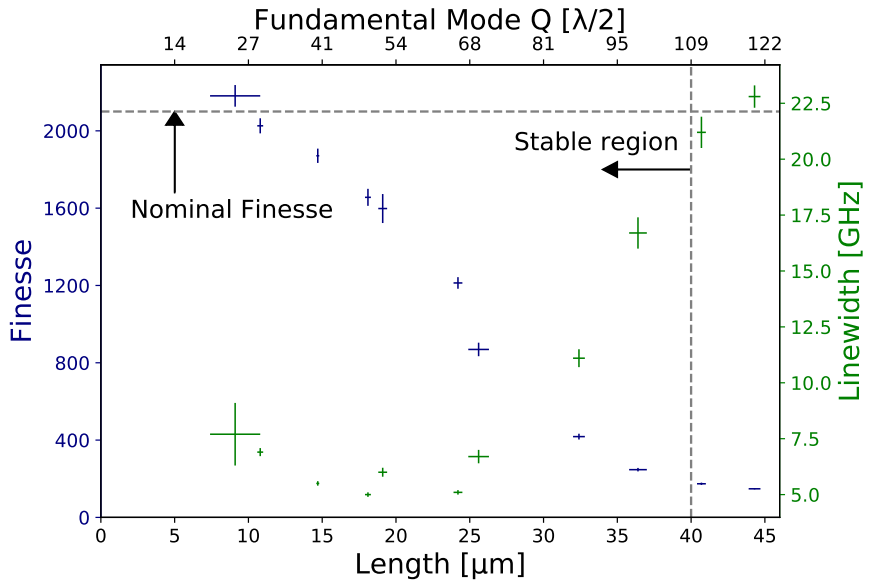

Figure 4.3.: Finesse of the bare microcavity (blue) for different lengths at room temperature. The upper x-axis show the length as a function of the axial mode order, measured with a wavelength of 737 nm. The cavity supports stable operation up to 40 µm, limited by the ROC. With finesse and length, the linewidth of microcavity can be calculated by formula 2.8, which is shown in green. For a length smaller then 10 µm, the maximum finesse of 2200 is reached and the linewidth is mostly affected by the length.

The described methods for the determination of finesse and length are used to measure the data presented in 4.3. The finesse shows the typical behavior for fiber cavities, which is for example also measured in Hunger et al. [2010] or Benedikter et al. [2015]. The finesse stays constant at the maximum of $\mathcal{F} = 2100$ for small lengths. This value is also expected by the fiber and mirror coating: a transmission of 1480 ppm at 736 nm leads to $\mathcal{F} = 2120$ with formula 2.6. For microcavity length $>$ ROC/2 a linear drop of the finesse and transmission is observed due to dominating clipping losses and for length $>$ ROC the transmission vanishes completely and the microcavity is not stable (for ROC determination, see appendix A.9). Beside this, the microcavity can couple so several higher order TEM [Benedikter et al., 2015]

Another method for measuring the length is to couple two lasers into the microcavity and measure the transmission with a single offset scan. This can be done by a small modification in the laser setup (figure 3.1): the Rb laser at 780 nm from another lab is coupled out and overlaid with DL at 737 nm. Both are fiber coupled to the microcavity and the transmission is measured with a PD. The advantage of this way is, that the offset needs to be scanned just one time and the hysteresis effects cancels out. The

fundamental modes can be associated to the two lasers by choosing different input powers which manifests in different transmission heights. After assigning the modes to the wavelengths, a remaining problem is the amount of fundamental mode orders, which lay inside the range spanned by the two wavelengths. For example for a length of 7 µm, the difference in the fundamental mode order is close to one, but for 30 µm, it is $\Delta q = 4.5$. This can not be obtained by one scan, so the method can be only used in combination with the one-laser method from above: after the coarse length is determined, a more precise value can be measured with two lasers.

Length determination by white light cavity spectrum

The most accurate way for determining the microcavity length is by a fiber coupled broadband light source (see appendix A.7 for emission spectrum). The microcavity serves as a spectral filter of the light and the transmitted spectrum can be measured by a fiber coupled spectrometer (see A.8). The center wavelengths of the fundamental resonances are fitted by a Lorentzian function (a typical transmission spectrum in shown in 4.4). The microcavity is resonant for a wavelength, if a whole-number ratio of half of the wavelength fits into to its lengths and form a standing wave. Therefore the length is:

$$d = q \cdot \frac{\lambda_1}{2} = (q+1) \cdot \frac{\lambda_2}{2} \tag{4.1}$$

where q denotes the fundamental mode order (TEM00q). For different resonant wavelengths ($\lambda_1 > \lambda_2$), which lay next to each other and differ only by one fundamental mode order, the absolute q and therefore the length can be obtained by:

$$\begin{aligned} q \cdot \frac{\lambda_1}{2} &= (q+1) \cdot \frac{\lambda_2}{2} \\ q \cdot (\frac{\lambda_1}{2} - \frac{\lambda_2}{2}) &= \frac{\lambda_2}{2} \\ q &= \frac{\lambda_2}{\lambda_1 - \lambda_2} \end{aligned} \tag{4.2}$$

An advantage of this length determination is, that there is no need to scan the cavity length, so a piezo hysteresis is not involved. The measurement can be done during

seconds, limited by the power of white light passing the microcavity and reaching the spectrometer. Due to the large lack of spatial coherence, only around 20 µW are coupled into a MM connecting white light source with the fiber breakout box. The fiber-fiber coupling at the breakout box lead to additional coupling losses (MM to PM), so only a small amount of light passes the cavity, which results in the low intensities measured by the spectrometer. An improved fiber coupling of the white light source can lead to much lower exposure times.

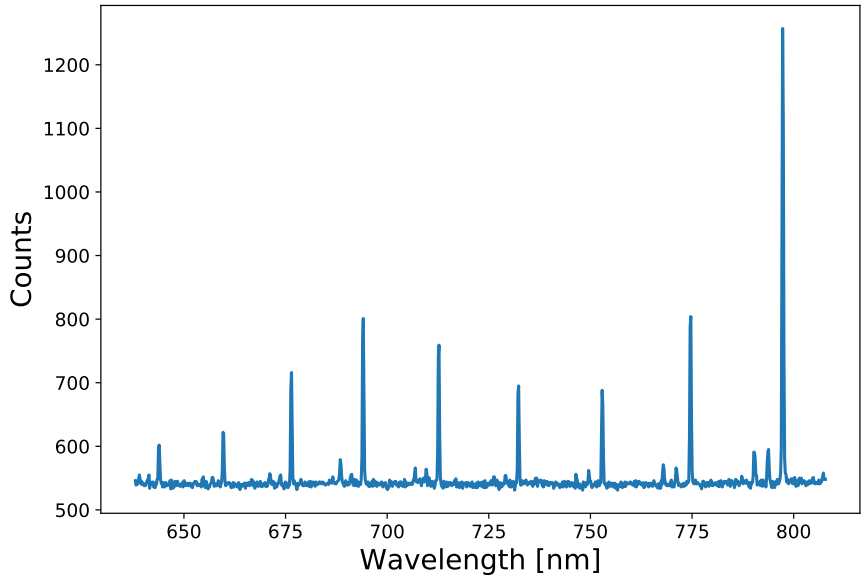

Figure 4.4.: White light spectrum of the bare microcavity. The exposure time of the spectrometer is 10 s. White light is coupled from the fiber and the transmitted light is collected after the mirror with the MM and send to spectrometer. The measured lengths is 13.4 µm, the fundamental mode order is q = 34 for the highest wavelengths of 797 nm and q = 42 for the lowest wavelength of 634 nm.

The length measurement doesn't include other cavity effects, like the penetration of the light field into the mirror or the Gouy phase. By the exact spectral determination of the resonant wavelength it is possible to measure the microcavity length with a accuracy $<$ 100 nm. This can be confirmed by changing the microcavity length in steps of half of a given wavelength and comparing the length result. Figure 4.6 shows such a measurement at lower temperature.

The temperature dependence of the unlocked microcavity length is shown in figure 4.5, which shows a long term measurement over 14 hours during the night. The experimen-

tal insert was open and the temperature in the lab is not stabilized and mostly affected by the air condition of the institute building. A few centimeters away from the insert, the temperature was measured with a USB temperature sensor (Yoctopuce) every five minutes and a transmission spectrum is recorded by the spectrometer. The spectra are plotted next to each other while displaying the time at the x-axis (upper part of figure 4.5). The white light source was switched on during the complete measurement, but its influence due to heating of the fiber can be neglected because of the very low light power reaching the microcavity. The temperature and lengths, calculated by the white light spectra, are shown in the lower plot of figure 4.5. The first six hours are linearly fitted and the corresponding slope of the length and temperature deviation is used to calculate the microcavity length response to temperature. For increasing temperature, the length becomes smaller. The number is set in relation to the typical linewidth ($\kappa/2\pi$) at this length (see fig. 4.3):

$$\frac{\Delta d}{\Delta T} = \frac{0.05\ \mu\mathrm{m/h}}{0.19\ \mathrm{K/h}} = 0.26\ \frac{\mu\mathrm{m}}{\mathrm{K}} = 30.1\ \frac{(\kappa/2\pi)}{\mathrm{K}} = 210\ \frac{\mathrm{GHz}}{\mathrm{K}} \tag{4.3}$$

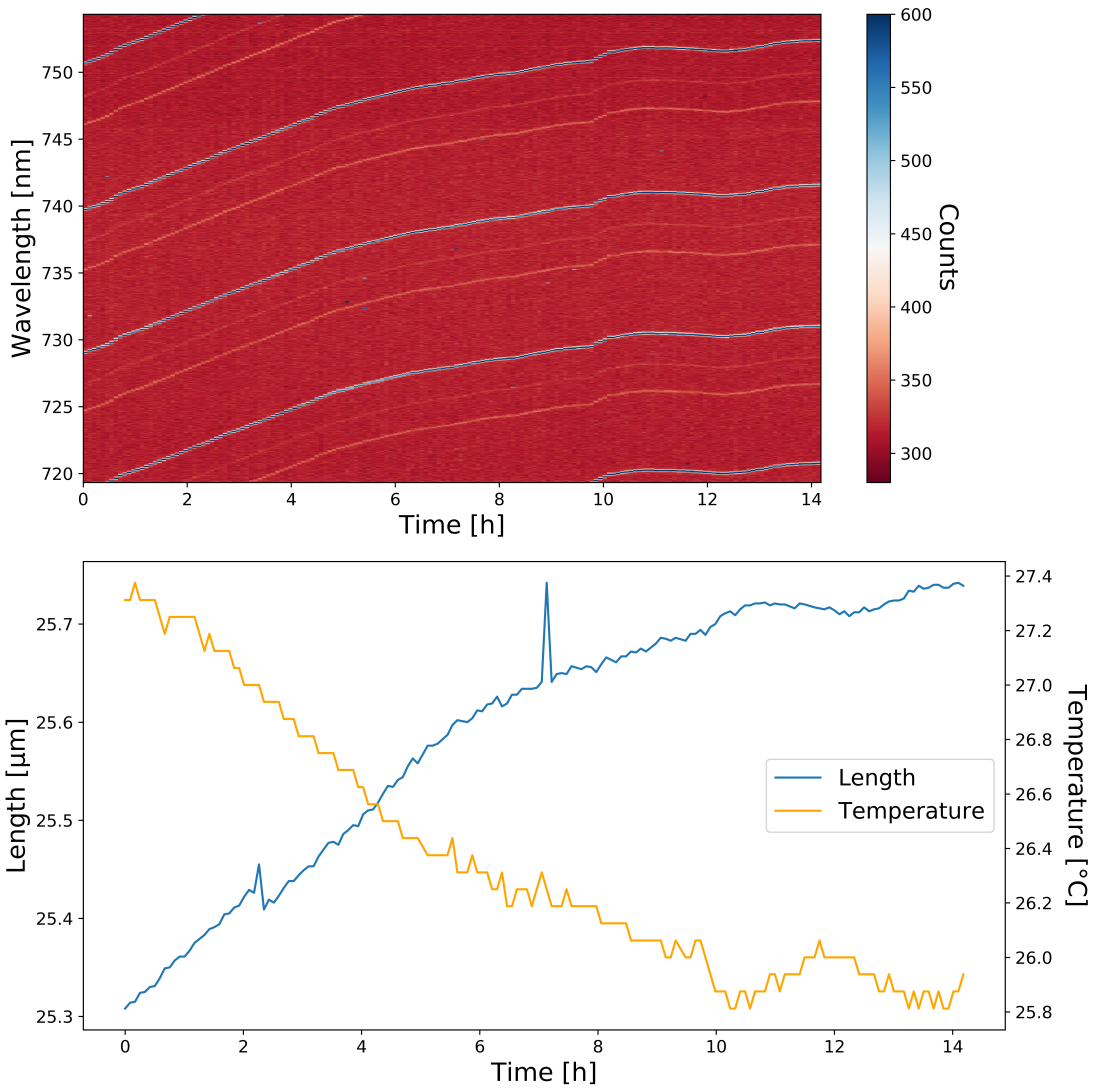

Figure 4.5.: *Upper part:* White light microcavity spectra, recorded every five minutes for 14 hours during the night. The experimental insert was open and not temperature stabilized, the temperature was measured in the proximity of the microcavity. The white light spectra are fused together to show the microcavity resonances over the time. The fundamental modes are visible as blue lines with a distance of $FSR_\lambda \approx 11$ nm, like expected from the length higher order transversal modes are white. *Lower part:* Calculation of the length for every spectrum and the corresponding temperature. By the slope of linear fits of the range between zero and six hours, a microcavity length response to temperature change of 0.26 µm/K is measured. The drop in the length after more then two hours is caused by the upper fundamental mode, which moved outside the spectra and can't be used for the length calculation. An outlier between six and eight hours is obtained by a wrong fit in the length calculation.

4.2. Performance at Lower Temperature

The microcavity was cooled down two times to LN and three times to LHe temperature. For all cooldowns, the microcavity signals in reflection and transmission were recovered by compensating the thermal drift. During the cooldown (first to LN in the pre-cooled cryostat, then to 4 K by transferring LHe), the experimental insert drifts typically over few 100 µm in one direction, so the microcavity length was set to 1-2 mm (by position readout of nanopositioners) to avoid that the fiber crashes into the mirror. After the temperature settles to the expected value, the mirror is brought closer to the fiber tip by observing the reflected light of the DL send to the microcavity through the fiber. Resonances appear as dips in the reflection signal for lengths smaller then the ROC. Then the microcavity can be scanned over a resonance to optimize the outcoupled transmission light after the mirror. This is done by positioning the MM into the focus of the collection lens with the second nanopositioner stack. Because of the very small optical path lengths of the beam inside the experimental insert (microcavity length + approx. 6.6 mm from mirror to MM), it is very easy to correct for thermal drifts after large temperature variations.
For low temperatures, the step sizes and scan ranges of the nanopositioners become smaller (see appendix A.10). For example, at room temperature, typically nine resonance peaks appear in the length scan (see 4.1), which reduces at 4 K to about three resonances. The nonlinear behavior of the piezo expansion for applied voltage due to hysteresis effects at room temperature, seem to be attenuated at lower temperature (appendix A.10).
The length determination by white light source, introduced in 4.1, is used to measure the microcavity length for a series of spectra shown in figure 4.6. Starting at a length of 7.5 µm (q = 19), the microcavity length is decreased in steps of the free spectral range on the wavelength scale FSR_λ for $\lambda = 780$ nm. This is done by driving the nanopositioner in the single step mode with low voltage. Each step shorten the length, which shifts the resonances to the direction of smaller wavelengths. By setting the offset of the axis to the right voltage, a resonance peak can be placed successively at 780 nm, where a white light spectrum is recorded and the length is measured. In that way, the microcavity length can be changed stepwise by a lengths of (780/2) nm = 390 nm. The mean difference and standard deviation of the measured length is $\Delta d = (0.392 \pm 0.011)$ µ m, which matches with the expected value. The discrepancy of 20 nm can emerge from inaccuracies in the fitted Lorentzian function to the white light spectra or uncertainties in the spectrum from the spectrometer.

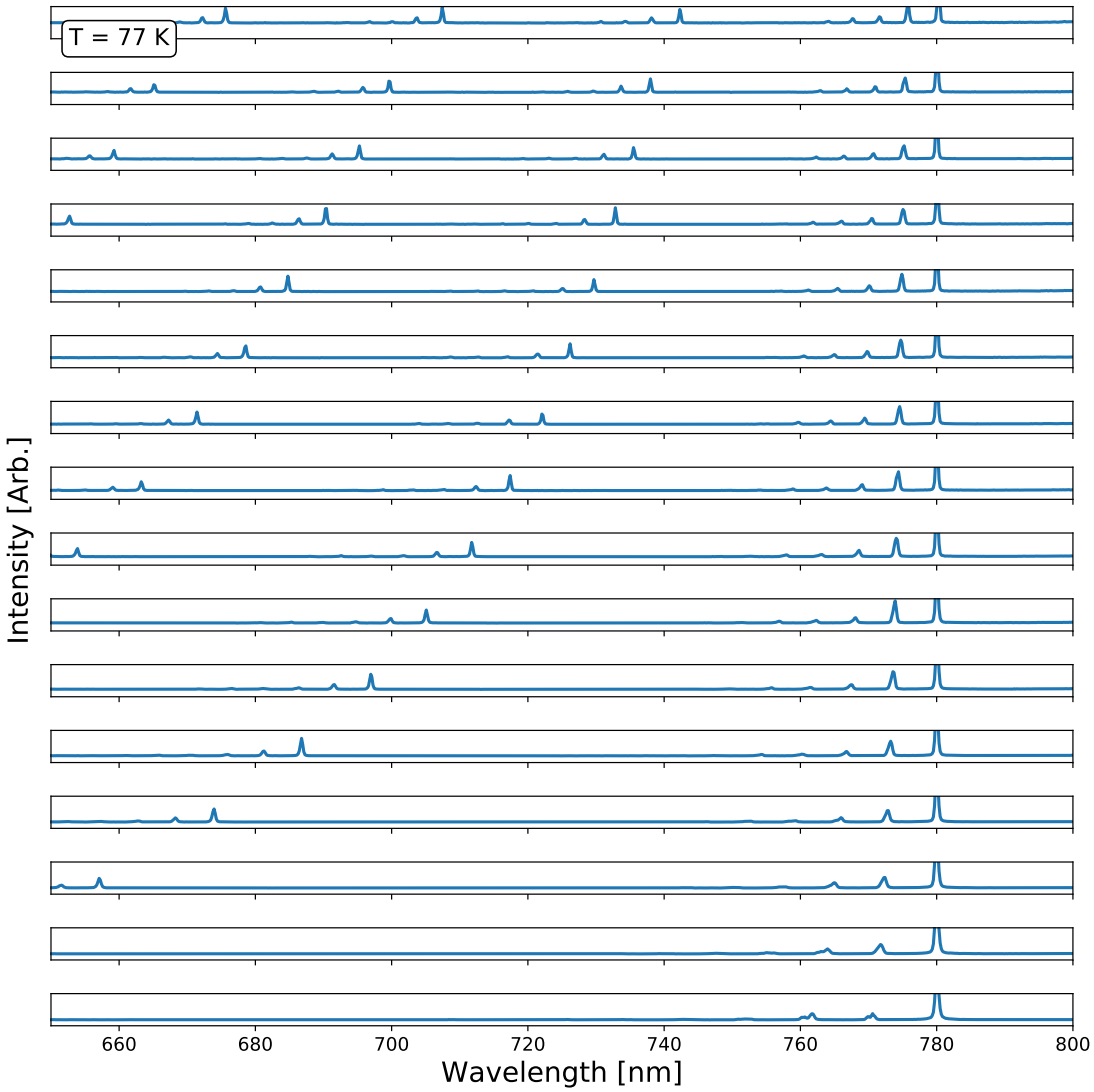

Figure 4.6.: Microcavity transmission for white light, starting in a length of 7.5 µ m with fundamental mode order q = 19 (first spectrum) to a minimum length of 1.3 µ m with q = 3 (lowest spectrum) in steps of one $FSR_{\lambda=780\text{nm}}$. In the first spectrum, four TEM_{00} modes are visible, while the lowest spectrum shows only one due to the large FSR_λ for short lengths. Different peak heights are recorded because of the wavelength dependent emission from the white light source (see appendix A.7).

An accurate scan of the microcavity length by the nanopositioner piezo in steps of 0.1 V from 20 V to 60 V is shown in figure 4.7. For such a map, a transmission spectrum is measured at different piezo voltages (microcavity lengths) displayed on the x-axis. All theses spectra are put next to each other while the measured counts are visualized by a

color at a pixel defined by a voltage and a wavelength. The spectra at approx. 20, 35 and 55 V correspond to the last three single spectra of 4.6. The map shows the linear dispersion for length deviation by the piezo expansion and the resonant wavelength of the microcavity. For a piezo offset of about 45 V, fiber and mirror get in contact. So increasing the voltage does not change the length anymore and the modes stay at the same wavelengths. Despite the 15 µm in diameter plateau, which was milled to the fiber tip before the concave feature was produced, the fiber kisses the mirror not in a length of zero µm due to small miss alignments of fiber and mirror and the geometry of the fiber dimple.

The smallest microcavity lengths that is resonant fo the SiV^- ZPL could be determined to 1.6 µm. This corresponds to a fundamental mode of q = 4 and is a comparable result to the measurements in Benedikter et al. [2017] with a similar setup. This lengths corresponds to a minimum microcavity waist of $\omega_0 = 1.35$ µ m (eqn. 2.10) and a mode volume of $V_{mode} = 2.3\ \mu m^3 = 5.8\ \lambda^3$ (eqn. 2.11).

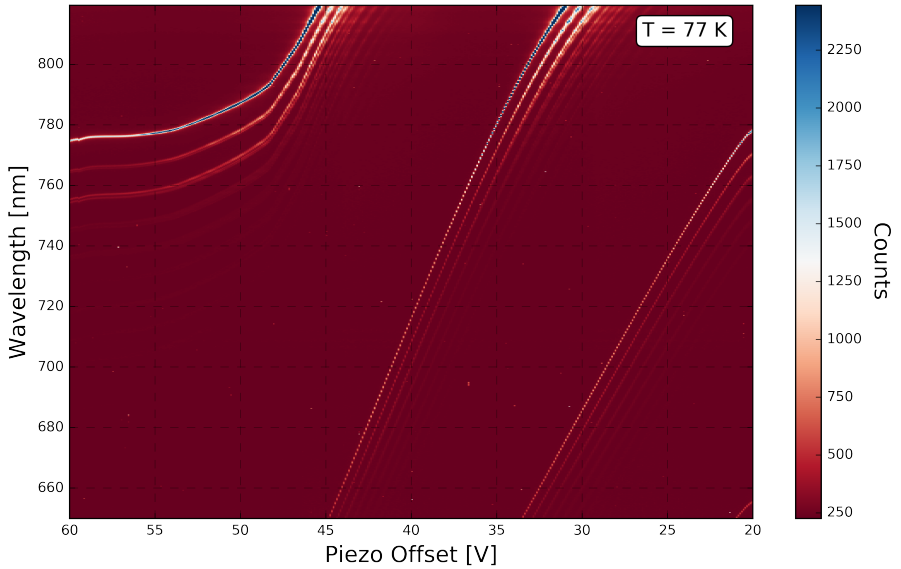

Figure 4.7.: White light microcavity spectra, showing the fundamental modes $q = 3, 4, 5$ (for 780 nm) from left to right with increasing length. For offset voltages bigger then 45 V, the fiber starts kissing the mirror, so the resonances settle and become independent to the offset.

4.3. Length Stabilization

If the microcavity is used to enhance the emission from a particular transition of the SiV^-, the length has to be stabilized to support the corresponding wavelength. So the length can be locked to a frequency reference (another laser at a far detuned wavelength to prevent interaction with the SiV^-) to compensate length fluctuations or drifts over a longer time period. The long spin coherence time of the SiV^- is only archived at very low temperatures (< 100 mK [Sukachev et al., 2017]), so the length stabilization must also perform under these conditions. For example, if the microcavity should enhance the C transition of the SiV^- with a nearly lifetime limited linewidth of 136 MHz [Rogers et al., 2014b], the microcavity must be locked to ≈ 1 pm for a assumed lengths of 2 µm. For the microcavity used in this thesis with a finesse of $\mathcal{F} = 2100$, this corresponds to a stabilization of 0.2 GHz = 0.6 % of the linewidth $\delta\nu$.
The lock of the microcavity is accomplished by monitoring the transmission of the DL and use the flank of the transmission signal as error signal. This is fed to a Proportional–Integral–Derivative (PID) controller adjusting the length by a shear piezo which carries the fiber tip (see 3.2). The locking circuit is shown in figure 4.8. The reflection signal of the microcavity could in principle be also used for the lock, but the long fibers connecting optical table and experimental insert lead to large polarization fluctuations in the baseline of the reflection signal. To avoid these fluctuations, polarization maintaining fibers (PM) can be used. By stress rods, incorporated around to the fiber core, they maintain a linear polarization over the fiber length. But for splitting the back reflected light coming out of the fiber from the incoupled beam, a polarization beam splitter in combination with a quarter waveplate is used: First, the laser light is reflected by a polarization beam splitter, which results in linearly polarized light in horizontal direction. This is transformed into circular polarization by the quarter waveplate and coupled by the fibers to the microcavity. The reflected light passes the waveplate again and gets linear polarized, but into the vertical axis to pass the polarization beam splitter and propagate to the PD measuring the reflection signal, see 3.1. A circular polarization is not maintained in the PM fibers connecting optical and microcavity, resulting in large fluctuations of the reflection signal on the range of minutes. This problem can be solved by a optical circulator, which separates the initial and reflection beam before the fiber breakout box. Despite an optical circulator, the reflected light has still to propagate through the transfer fiber inside the cryostat, from the breakout box to the microcavity and back but the fluctuation could be mitigated.

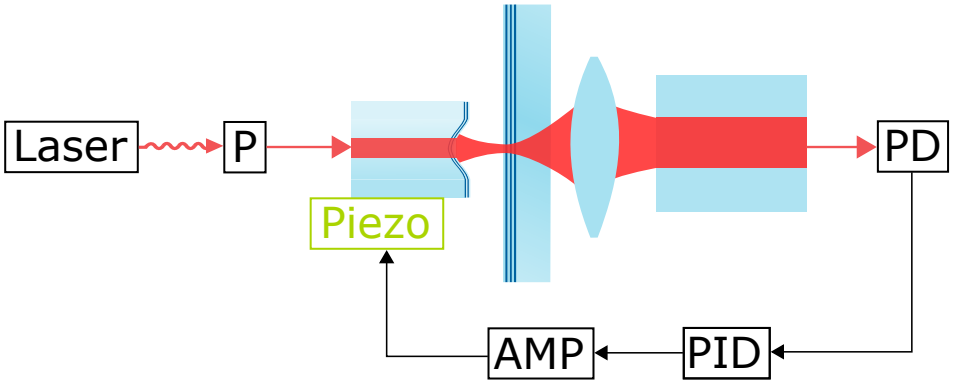

Figure 4.8.: Circuit for length stabilization of the microcavity by a side-of-fringe lock with the transmission signal. The red wavy line indicates free space light propagation, while the solid lines denote propagation in a fiber. P: polarization control, PD: photodiode, PID: proportional–integral–derivative controller, AMP: amplifier.

To generate the transmission signal, the laser is coupled in through the fiber and collected after the mirror to the MM, which is directly fiber connected to the PD. A DigiLock 110 from Toptica is used as a PID controller, programmed from the standard user interface by USB connection to the experiment PC. The output (+/- 2 V) can be amplified (Piezomechanik SVR 350-1 or TEM MiniPia 101) up to +/- 250 V, to cover the complete travel range of the locking piezo of 0.5 µm at room temperature. The locking piezo (one layer from PI P123.03T) is a bipolar shear piezoelectric actuator with a very high resonance frequency of 1.75 MHz (for a piezo not carrying any weight) in shear direction to avoid additional vibrational excitation.

The length stabilization is done by a side-of-fringe lock with half of the peak height of the transmission signal as reference point. Instead of other locking-techniques, this method cannot distinguish between a fluctuation in the laser intensity or the length, because both would change the transmission signal in the same way. Because of this, the laser power and the fiber coupling has to be stable enough. Another disadvantage is the asymmetric capture range, which is limited to half of the microcavity linewidth, where higher lengths fluctuations can not be resolved. For example in the above mentioned case for 2 µm (finesse $\mathcal{F} = 2100$), half of the linewidth (35.7 GHz) would correspond to a lengths deviation of 65 pm.

Lock at Room Temperature

To keep the environment similar and perform the lock under experimental conditions, the room temperature lock is done with a closed experimental insert, which is inside the empty cryostat. A typical lock signal is shown in figure 4.9. First, the vibrations of the unlocked microcavity is measured. This is done by a of 200 scans of the transmission peak by the locking piezo (350 Hz, 22 Vpp with amplifier), which is fitted by a Lorentzian function to extract the center position. The linewidth $\delta\nu$ of the microcavity is calculated by length and finesse (eqn. 2.8) and transformed to a length deviation δd by [Demtröder, 2011]:

$$\frac{\delta\nu}{\nu} = \frac{\delta d}{d} \tag{4.4}$$

The left side of 4.9 shows the obtained center positions in frequency related to the linewidth and in length deviation. The unlocked microcavity length fluctuates in a range of 250 pm Root Mean Square (RMS), which equals to 1.3 times the linewidth at a length of 12 µm. At this point, the finesse is close to the maximum of 2100. The resonance scans are recorded over half an hour, so large temperature drifts are not visible in this measurement, despite the missing temperature stabilization.
At room temperature, the voltage range of the PID controller is large enough to scan the microcavity over one resonance. Hence the length stabilization is performed here without the amplifier, which acts as a low pass. To quantify the lock, the locked transmission is measured and shown in the right side of figure 4.9. From a scan of the transmission peak, the transformation of PD voltage to a frequency/length is calculated. This is only valid, if the transmission signal doesn't fluctuate more than half of the linewidth, because a frequency on the other flank of the transmission peak would be mistakenly associated with a smaller frequency. The locked transmission signal fluctuates on the range of 31 % of the cavity linewidth, so the length variation could be reduced from 250 pm to 60 pm RMS.
By equations 2.8 and 4.4, the linewidth in the spatial domain can be expressed as a function of the finesse:

$$\delta d = \frac{\delta\nu\lambda d}{c} = \frac{\lambda}{2\mathcal{F}} \tag{4.5}$$

So with increasing finesse, the linewidth (in length) becomes narrower and therefore, the microcavity reacts more sensitive to noise. For the lock at room temperature, the finesse is almost close to the maximum, so it can be expected that the lock works also at smaller microcavity lengths.

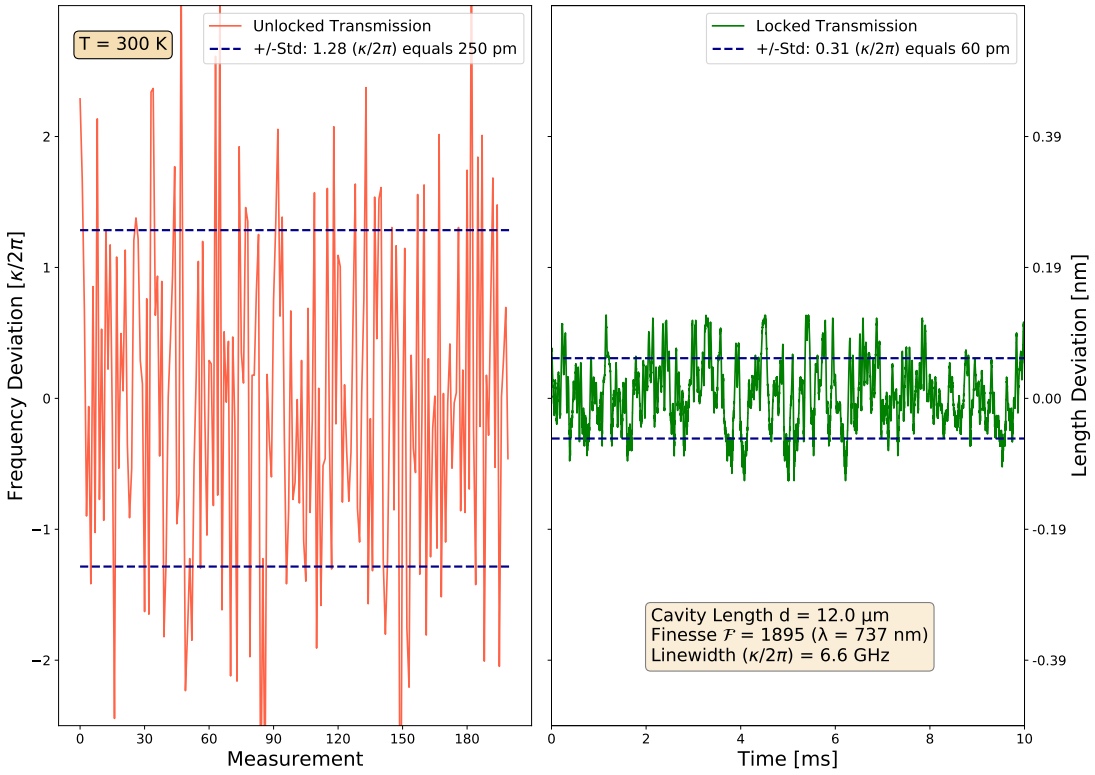

Figure 4.9.: Length stabilization of the microcavity at room temperature. The properties of the microcavity are shown in the text box in the right plot panel. *Left:* Series of 200 microcavity scans around a transmission peak (details in the text). The resonance center position is expressed as frequency deviation in terms of the linewidth $\delta\nu = \kappa/2\pi$ and the corresponding lengths deviation (right axis). The graphs show the fluctuation of the unlocked microcavity length. *Right:* microcavity transmission signal over a time period of 10 ms for the locked case. The lock suppresses the lengths fluctuations by a factor of four.

Lock at LHe Temperature

The microcavity length is also locked at LHe temperature by a side-of-fringe lock with the transmission signal. During these measurements, the experimental insert is surrounded by LHe in the main bath of the cryostat, which continuously evaporates and is exhausted to the He transfer line. Neglecting the introduced heat from controlling the piezo and the low optical laser power ($\leq$ 1 mW) used to lock the microcavity, the temperature is very well stabilized to 4 K. Due to the constant temperature, the microcavity length does not drift on the scale of hours, which is confirmed by long white light spectra similar to the measurement shown in figure 4.5.
Because of problems with the DL, the external Rb laser at 780 nm is used. The transfer fiber between the laboratories is directly fiber-fiber coupled to the PM inside the cryostat. This wavelength is still inside the stopband of the microcavity coating with a transmission of 3033 ppm (maximum finesse of 1000). With equation 4.5, locking should be easier with lower finesse.
In these measurements the cryostat is used like a bath cryostat to keep the temperature constant a 4 K. For this operation, LHe has to be transferred one to two times per week. During the transfer, the temperature can be increased up to 30 K due to the introduced heat from the warm He gas in the beginning of the transfer. After about half an hour, the temperature typically settles back to for 4 K.
Vibrations from the environment occur, due to the cryostat operation. The gas handling system of the cryostat has a loud fan, which can lead to length fluctuations. The LN shield surrounding the main bath must be filled to keep the evaporation rate of the LHe from the main bath low. The unlocked transmission is recorded by setting the microcavity with the locking piezo resonant to the flank of a transmission peak (fig. 4.10 left). This is again only valid, of the fluctuations are not higher than half of the linewidth. With this method, the microcavity length does nt need to be scanned (like in the room temperature measurement), which can lead to additional excitations depending to the scan frequency and amplitude.

The PD voltage is transformed to a length deviation like explained above in 4.3. At the same length of 34.6 µm with a relative low finesse $\mathcal{F} = 186$, the microcavity is locked (fig. 4.10 left). The fluctuation of the locked transmission is suppressed almost by a factor of three to 90 pm. By comparing the unlocked and locked transmission, it is visible, that the deflections $\geq$ 400 pm are compensated by the lock.
The microcavity lock is also tested at 4 K for a length of 22.2 µm ($\mathcal{F} = 624$) and a

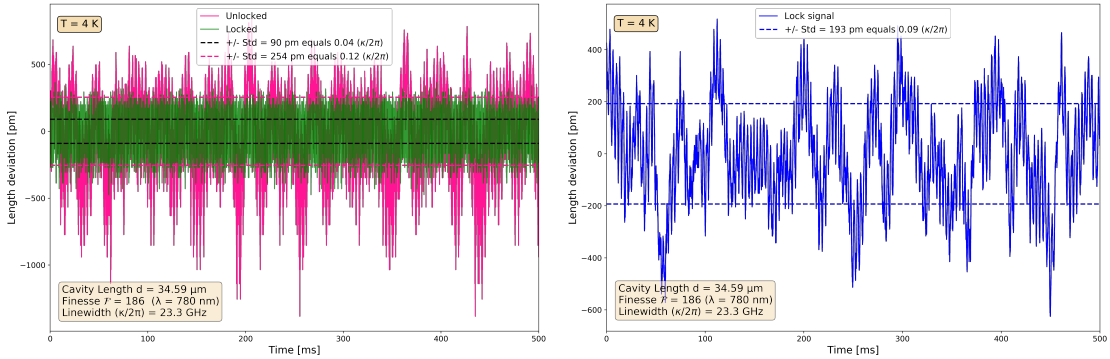

Figure 4.10.: Microcavity length stabilization at 4 K. *Left:* unlocked and locked transmission over half a second. The standard deviation of the length variation is also expressed in terms of the microcavity linewidth. The lock reduces the fluctuations by a factor of three. *Right:* Corresponding lock signal expressed in length deviation. The lock is not compensating for all flucutations, because the standard deviation is smaller then the value of the unlocked transmission.

length of 13.5 µm ($\mathcal{F} = 792$). At these lengths, the unlocked transmission signal is fluctuating in the range of half of the corresponding linewidth, so the measurement can not be taken for a characterization of the vibrations. The lock there performs worse (RMS length variation ≥ 100 pm) and is not filtering the higher defections any longer. To cool the He^3-He^4 refrigerator to temperatures below 4 K, a rotary pump is used to exhaust the 1 K pot to a low temperature [Balshaw, 1996], which is placed in the cryostat insert four stages above the experimental insert (see picture A.7 in appendix). A second bigger rotary pump is used to pump the He^3-He^4 dilution. Both pumps are directly connected to the top of the cryostat insert with huge KF tubes, which transfer the vibrations of the pumps. To test their influence of these pumps, both are switched on. As expected, the lengths fluctuations are much higher with the running pumps. By coupling another DL running at 854 nm with much lower finesse, the length vibrations are measured to be > 1 nm. One can mitigate theses effects by placing the pumps in a other room and using a vibration isolation of the tubes.

Length Fluctuations

The system seems to be very stable with 250 pm RMS in the unlocked case. Brachmann et al. [2016] reported that their fiber-based microcavities at ambient conditions on an optical table, have an average noise level of 300 pm to 1 nm RMS. So the microcavity used in this thesis, has even at 4 K less vibrations. One reason for this could be the

installation of the experimental insert, which is attached to the baseplate of the cryostat insert. It that way, it is hanging from the top of the cryostat and not mounted to an optical table with direct contact to impact noise. The stages of the cryostat insert are connected by thin metallic tubes (see appendix A.7), which can facilitate additional length noise.
Using the dilution refrigerator as a bath cryostat leads to the advantage, that for keeping the temperature at 4 K, no pump needs to run, like in a continuous flow cryostat. For operating at 4 K, the insert is just surrounded by LHe. This may explain, that between room temperature and 4 K, no additional RMS length noise is generated. Riedel [2017] showed with a miniaturized microcavity, residing in a sample cage, which is attached to a long steel skeleton in a helium bath cryostat, RMS fluctuations of 24 pm for 0-200 Hz, with no major contributions of acoustic noise at higher frequencies. By contrast, in a pulse tube cryostat with passive stabilization, Bogdanović et al. [2017] measured a RMS length displacement of 500 pm to 800 nm for a fiber-based microcavity depending on the cryostation pulse cycle. For precise measurements, the cavity needs to be synchronized with the 1 Hz cycle operation.
To analyze further the length vibrations, the locked and unlocked transmission together with the lock signal (figure 4.9 and 4.10) are Fourier transformed and shown in figure 4.11. The spectral distribution of the fluctuations show that at 4 K additional frequencies are excited compared to the room temperature measurements. Some frequencies, for example the peak around 280 Hz and frequencies below 50 Hz are much more pronounced at LHe temperature.

This leads to the assumption that the measurement of the unlocked length vibrations at room temperature (presented in figure 4.9), exhibits too much noise (or an upper bound value). This could be caused by performing the measurement with the locking piezo being scanned, which may add some length fluctuations due to the scanning voltage ramp. By recording the transfer function of the microcavity (open-loop), by sweeping the locking piezo frequency and recording the magnitude and phase, the lowest frequency is found, before the system starts ringing [Janitz et al., 2017]. This is measured to be around 5 kHz, which determines the maximum lock bandwidth.

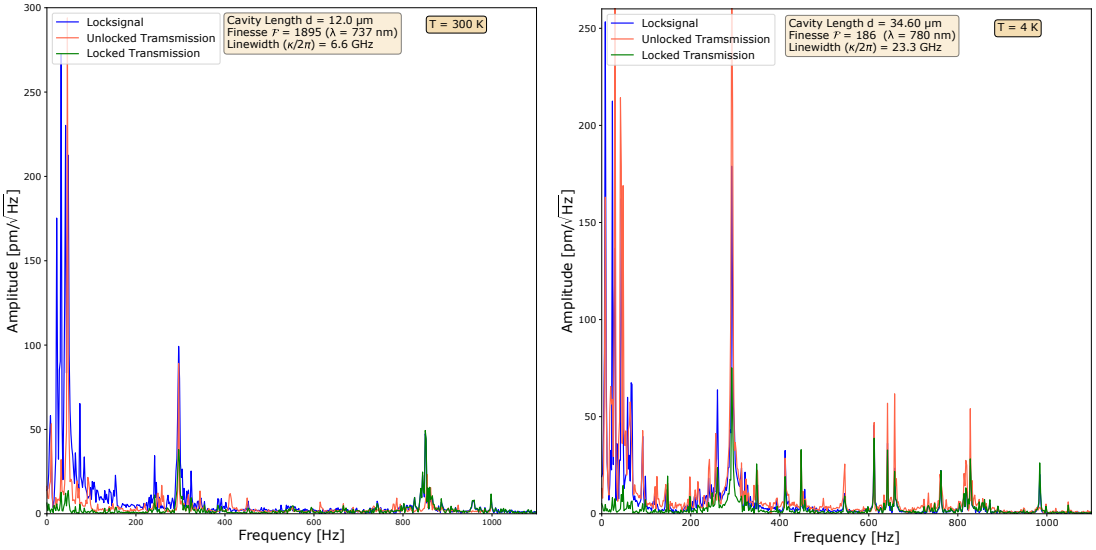

Figure 4.11.: Fourier transformation of the microcavity length stabilization. The noise spectral density at room temperature (left, shown in figure 4.9) is compared with 4 K (right, shown in figure 4.10). At LHe temperature, some of the lower frequency vibrations become more pronounced and additional higher frequencies are excited. The Lock compensates the vibrations < 200 Hz and is suppressed at higher frequencies because this would lead to additional excitation.

Possible Improvements

van Dam et al. [2018] simulated for NV, that with a finesse of 8000, RMS vibrations on the level of 0.1 nm can lead to ≈ 40 % emission into the ZPL (for appropriate diamond thickness and losses at the surface). To improve the lock, one can think about the following points:

- Design of a new experimental insert:
  - A compete monolithic architecture can suppress the noise by 2-3 orders of magnitude [Brachmann et al., 2016]
  - The microcavity optical axis can be aligned perpendicular to the cryostat insert. This may reduce the excitation along the axis through the metallic tubes
  - Mounting the half inch mirror not on the 3D nanopositioner stack, which has probably a low characteristic vibration frequency. A passive vibration isolation stage can be used to mount the fiber

  - A finite element analysis program like ANSYS can be used to simulate the mechanical modes of the experimental insert with the microcavity to improve the design [Janitz et al., 2017]

- Use other locking techniques like the Pound-Drever-Hall stabilization scheme [Drever et al., 1983] by frequency modulating the probed laser light. This method has a symmetric and increased capture range spanned by the sidebands from frequency modulation. This can also be done with the cavity transmission light and with modulated sidebands lower than the cavity linewidth (which can be in the range of 10 GHz), like shown by Brachmann et al. [2016]

- The coating of the microcavity can be designed, to give the possibility to lock with a laser wavelength at the left or right flank of the stopband with lower finesse. It should be ensured, that the locking laser does not interact with the emitters inside the cavity, e.g. by choosing a higher wavelength.

5

Microcavity with Integrated Diamond Membrane

This chapter contains the measurement with the hybrid system of microcavity and incorporated diamond membrane. By long lateral scans over the macroscopic mirror, the microcavity can be used to include the different diamond membrane samples. The surface of the diamond membrane introduces an addition loss channel, which depends strongly on the surface roughness. The losses directly affect the linewidth and thereby the finesse. In the worst case, the membrane causes a complete collapse of the microcavity transmission signal, because all of the light is lost. Measurements are depicted in the first section of this chapter.

After the first two windows (1,2) and (1,3) were investigated, the sample mirror was sent to the group of Christoph Becher at the University Saarbrücken for confocal microscopy measurements. Unfortunately during the shipment from Mainz, the two windows fell from the mirror and got lost. So only the window (2,2) and the broken diamond piece remain on the mirror. Because of the carbon debris on the window (2,2), the broken window is used for the measurements of the dispersion relation (second section of this chapter) and the SiV^- *(next chapter).*

5.1. Transmission and Finesse

The membrane inside the microcavity has direct influence on the reflection and transmission signal when the microcavity is probed with the DL laser. Beside the losses of the cavity by diffraction and absorption in the mirror and coating substrate, the additional layer on the mirror introduces a new loss channel of the cavity, which depends strongly on the surface roughness. Besides this, the diamond material is also absorbing a small fraction of light. Figure 5.1 shows a typical length scan with diamond membrane at LN temperature with three resonances visible in the reflection and transmission signal. Because of the very short air gap, the fiber tip is slightly touching the membrane at the end of the scan range. This can be recognized by the reflection signal, which is dropping for about the last 20 % of the scan voltage ramp.
The scanned resonances are split into two peaks. For a cavity without a membrane, the splitting of a fundamental cavity resonance into a polarization doublet can be explained with elliptical mirror surfaces as the dominant source [Uphoff et al., 2015]. The concave mirror has the shape of an elliptic paraboloid with different ROC along the two principal axes.

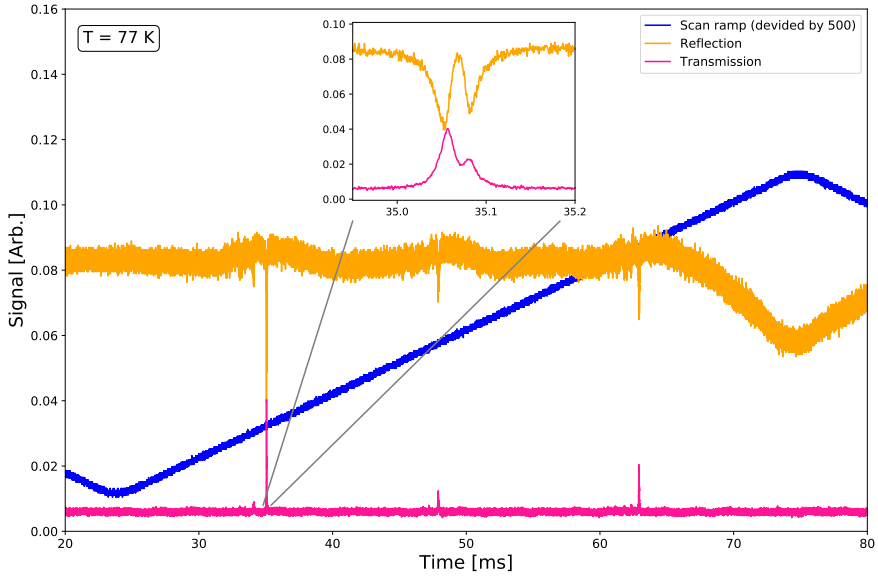

Figure 5.1.: Length scan with membrane incorporated to the microcavity at 77 K. The air gab is very short, so the tip is touching the mirror after the third resonance, which leads to a drop in the reflection signal. Due to the membrane, the resonances are split into 62.3 ± 6.5 GHz, 125.9 ± 14.7 GHz and 96.5 ± 12.2 GHz. Their finesse is (from left to right) $\mathcal{F} = 683 \pm 4; 322 \pm 3$ and 571 ± 6.

These polarization splittings are typically observed in cavities with much higher finesse [Uphoff et al., 2015]. Polarization splitting is not observed at the mirror and appear only at some positions on the membrane. It is probably connected to the flatness gradient of the membrane, which varies. Because of this, the polarization splitting is only observed at some lateral positions on the diamond membrane, like shown in fig. 5.1. Another reason could be a birefringence, which is released in the diamond membrane.
The membrane also has an influence on the cavity waist. The waist of the diamond $\omega_{0,D}$ and on the mirror can be calculated [van Dam et al., 2018]. Due to the thin diamond membrane, the effect is very small and is neglected in the following. The mean absolute deviation between the two waists is smaller then 0.1 µm.
Beside the polarization splitting, the membrane reduces at some lateral positions the transmission signal dramatically. It can even lead to a complete suppression of the transmission. This is measured by scanning the microcavity length continuously and changing the lateral position of the mirror by the nanopositioner stack. In that way, a scan along a lateral axis can be performed. Figure 5.2 shows the observed transmission signal, measured on two membrane windows. The edge of the window surface has a darker color, which is amorphous carbon from the laser cutting (detected also by confocal microscope). The carbon debris prohibits the light field from evolving inside the microcavity and no transmission can be observed. By this clear drop in the transmission signal, the nanopositioner readout can be aligned to the microscope images from the windows, shown in 5.2.
Scans in lateral directions can be done over the complete travel range of the nanopositioner (over millimeters). By observing the fiber tip with a light microscope next to the experimental insert, the microcavity can be set to arbitrary positions on the mirror. The movement axis of the steppers are not perfectly aligned with respect to the fiber tip surface. By this tilt, the microcavity length is not constant when the lateral position is changed. Because of this, a lateral scan also includes a deviation in the length. This strongly depends on the way how the mirror is put into the holder and fixed by the four screws. The steepest tilt is measured to be a 1-2 µm length deviation for a lateral scan of 100 µm in on direction.
Figure 5.2 also shows the influence of the membrane on the measured finesse. For a high strong coupling of SiV^- and microcavity, a high finesse is required (see theory 2.3), so the losses by the membrane should be as low as possible. The main losses raise due to scattering at the interface between air and diamond inside the microcavity, strongly depending on the surface roughness σ_{DA}. A high density of color centers in the cavity waist can also lead to a reduced finesse [Häußler et al., 2018].

The finesse is measured at different lateral positions on the windows in regions with lower implantation doses, shown in 5.2. For this, the DL is set to emit at 736 nm and the microcavity transmission signal is used. Like the height of the transmission signal, the finesse also depends strongly on the lateral position and can vary in the range of the microcavity waist. First, the finesse is measured next to the membrane at a length of 14 µm for comparison. This yields a finesse of 1300-1400, which is lower than expected by the measurements performed before in figure 4.3. The finesse depends on the exact position on the mirror and can be lowered by surface contamination. Another reason is that the sample is not positioned in the same manner like the mirror, which was used to measure the data in 4.3. So a different angle between fiber tip and mirror could lead to lower finesse values even at the bare mirror.

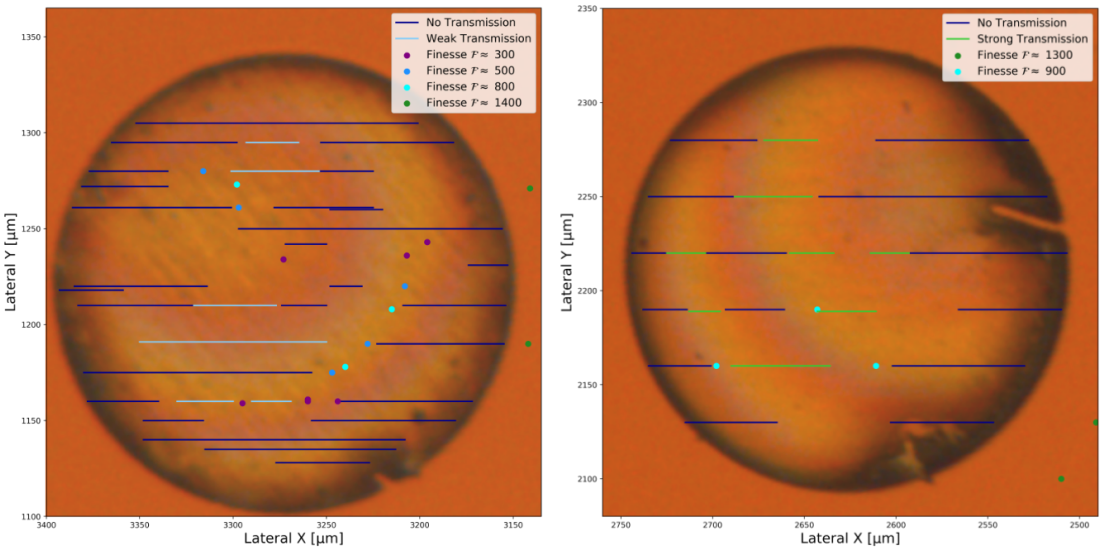

Figure 5.2.: Transmission of membrane windows (1,2) and (1,3) on the right side. Long lateral scans are recorded by continuously scanning the microcavity length over a few FSR and observing the transmission peaks. The measured positions from the nanopositioner readout are plotted together with the light microscope picture acquired before the sample mirror is integrated to the setup. The membrane contains regions where no transmission can be observed, specially at the edge of the windows with the carbon debris from laser cutting. The finesse is measured for a microcavity length around 14 µm, which is measured on the bare mirror (darker green).

After the mirror finesse and length is measured on the bare mirror, some lateral positions on the windows are examined. In diamond window (1,2) (left of fig. 5.2), the finesse spreads widely between 300 and 800 at different lateral positions. At theses positions, the transmission signal is also higher compared to the scans with a weak transmission in 5.2. For window (1,3) (right of fig. 5.2), the finesse is reduced to ≈ 900. The losses in general can be estimated by 2.6, which leads to (symmetric mirror coating):

$$L = \frac{\pi}{\mathcal{F}} - T \tag{5.1}$$

With T = 1480 ppm (for 736 nm), the losses at the bare mirror can be calculated. Due to clipping losses at this lengths, the finesse is not at the nominal value expected from the reflectivity. The losses on the bare mirror can be used to calculate the losses on the membrane windows:

- Bare mirror: losses of 937 ppm and 764 ppm for finesse of 1300, 1400 (wavelength of 736 nm)
- Membrane window (1,2): losses of 8990 ppm to 2447 ppm (min finesse of 300 and maximum measured finesse of 800); where 8226 ppm to 1683 ppm can be attributed to the influence of the diamond membrane
- Membrane window (1,3): losses of 2011 ppm (finesse of 900), where 1074 ppm can be attributed to the membrane

The better finesse values for membrane (1,3) leads to the suspicion, that the back side of the diamond membrane has a lower surface roughness. Membrane (1,3) is the only one which rotated after laser cutting and landed on the correct side with facing up the lift-off side. Maybe this has a surface roughness below 5 nm, which was measured with the lift-off side facing up. In the microscope picture 5.2, the right membrane (1,3) looks smoother then the membrane (1,2) on the left side.
After the diamond membrane windows (1,2) and (1,3) are incorporated into the micro-cavity, the sample mirror is removed from the experimental insert and examined again with the light microscope. Figure 5.3 shows the overlay of the two recorded microscope pictures before and after the measurements. It is visible, that the two investigated samples moving on the mirror over a few tens of micrometers. It is also rotated in respect to the previous position while keeping the interference fringe structure of bright and dark stripes on the surface. The two not investigated samples, window (2,2) and the broken

window piece, stayed at the initial position. When the mirror and fiber tip are brought too close to each other, electrostatic force between the two dielectric materials diamond and glass can push the diamond membrane away. This suggests, that the bonding between the diamond membrane and the mirror is imperfect. This could be caused by the laser cutting of the membranes out of the diamond scaffold. The created amorphous carbon debris falls down to the mirror and prevent the membrane from bonding fully to the mirror. It was found that for microcavity lengths > 5 µm, the membrane stayed at the same position. Smaller lengths can be achieved by slowly decreasing the lengths in very small steps, but a shift in the position can still happen.

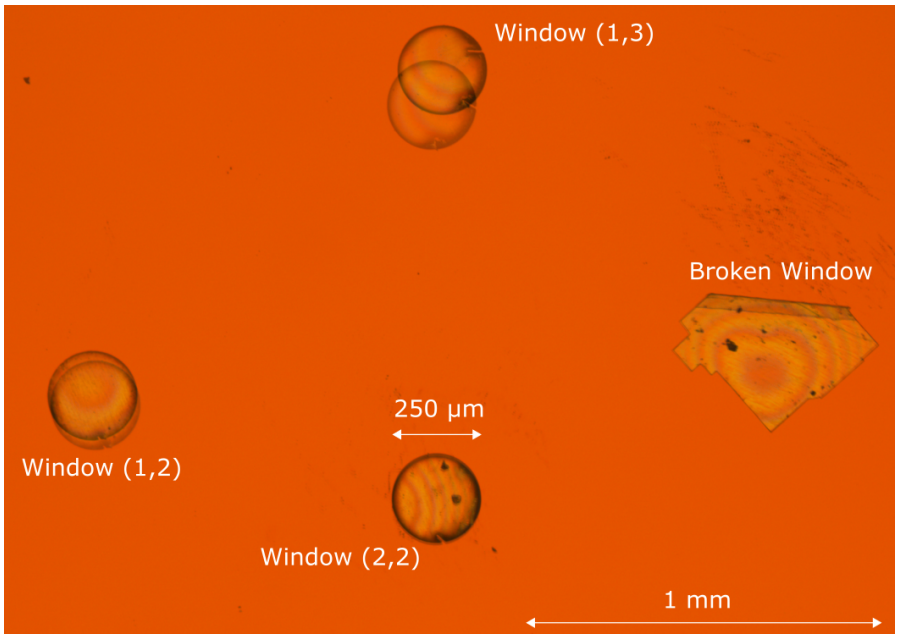

Figure 5.3.: Overlayed light microscope pictures before and after the diamond membrane sample were investigated with the microcavity. The two windows (1,2) and (1,3), which were incorporated into the microcavity moved over a few ten micrometer and rotated, while samples which were not examined remained at their position.

5.2. Dispersion Relation

The hybrid system of two cavities features a non-trivial dispersion relation, which is introduced in the theory section 2.2.2. The straight lines (see figure 5.4), which represent the wavelength of the fundamental mode as function of the cavity lengths, become wavy with parts of steeper (”air-like” modes) and shallow (”diamond-like” modes) slope.
To measure the dispersion relation of the microcavity with and without the membrane, white light is coupled in, while a spectrometer measures the transmission signal. Both devices are coupled to the fiber breakout box on top of the cryostat. For the white light generation, a compact broadband light source is used, which covers the complete stopband of the microcavity (insert of figure A.8). Due to better coupling of the white light source to the transfer MM fiber, the light is launched through the MM and focused by the aspheric lens to the macroscopic mirror. The transmission light, guided to the PM fiber is coupled via a second MM to the spectrometer.
A scan of the microcavity length with the corresponding transmission spectrum is in the following shortened by Length Dependent Transmission Spectrum (LDTS). A typical LDTS on the bare mirror is depicted in 5.4, showing the linear dispersion relation between microcavity length (x-axis) and resonant wavelengths (y-axis).

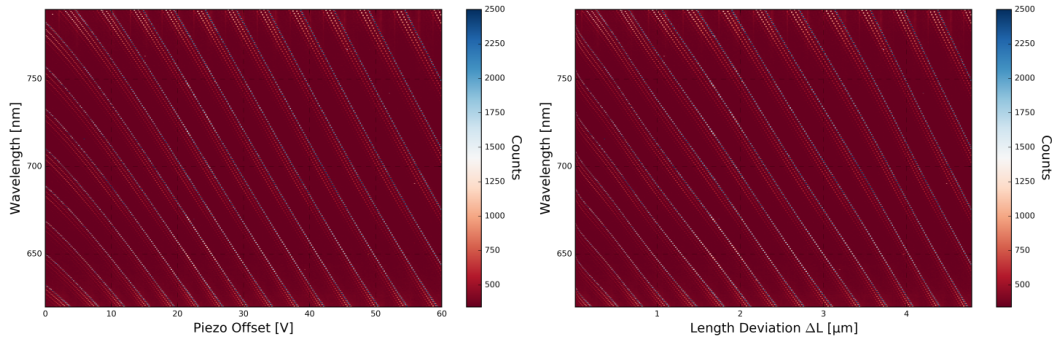

Figure 5.4.: *Left:* Dispersion relation of the bare microcavity at room temperature. The microcavity length is 11.5 µm for an offset of zero and decreased to 6.8 µm for an offset of 60 V. Only in this figure, the map goes from longer to shorter microcavity length, which leads to falling lines, where the microcavity is resonant. *Right:* The same measurement for the corrected calibration of axis offset to lengths deviation (see also appendix A.10). The non-linear behavior of the piezo for low voltages is transformed to straight lines, which are expected by the linear dispersion relation of a cavity.

From the scan, the FSR in wavelength can be directly measured. Like for probing the microcavity with laser light, the membrane has a strong influence on the transmission spectrum of white light. Furthermore the spectrum differentiates a lot in compari-

son with the bare mirror (4.4). For some longitudinal q values, nearly all modes are suppressed and the fundamental mode is barely visible. Other mode groups are more pronounced. The FSR is not constant anymore, varying on the order of nanometers. Like for the measurements with the DL form the last section, the membrane reduces the transmission signal also for the white light by scattering and absorption.
The hybrid modes are fitted by the 1D model eqn. 2.12, shown in fig. 5.5. The length of the LDTS is scanned in 0.1 V ≈ 8 nm steps over the complete length range.

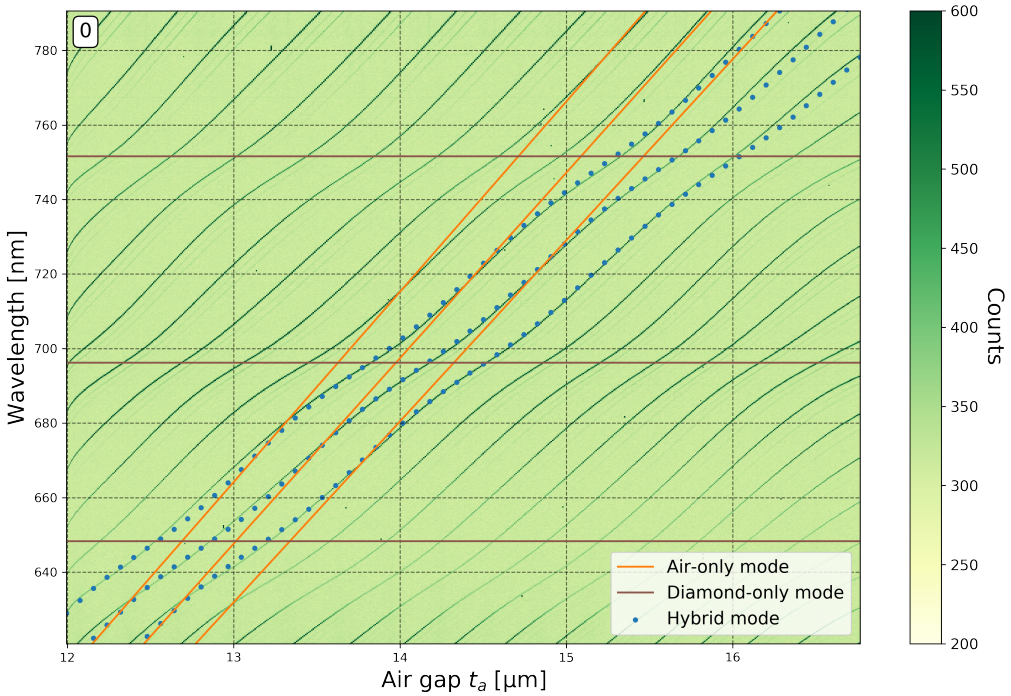

Figure 5.5.: Hybrid dispersion relation of microcavity length and resonant wavelengths. The LDTS is measured at position zero on map 5.6. The hybrid modes are fitted by egn. 2.12, revealing an air gap of t_a = 11.98 µm, a diamond thickness of t_d = 1.96 µm and a mode order of (53.2,54.2,55.2), plotted as blue dots. The modes for a bare cavity with an air gap of t_a are plotted in orange by eqn. 5.2 (q_a=(39.1,40.1,41.1)). The modes emerging in a cavity, formed only from the two surfaces of a diamond are plotted in red from eqn. 5.2 (q_d=(13.1,14.1,15.1)).

By fitting the function to the hybrid dispersion relation, important parameters of the system like the length of the air-gap t_a, diamond thickness t_d and the order q of the fundamental TEM_{00q} can be figured out. This is done in 5.5 with blue dots representing the values from the fit function for a better overview. Equation 2.12 is describing the coupled modes very accurately in a range of 680 nm to 750 nm. For higher wavelengths,

the model differentiates from the measurements, following rather the first higher order TEM and not the fundamental mode.
The hybrid fit leads to a diamond membrane thickness of t_d 1.96 µm, which is higher than the expected (see table in A). The air gap t_a = 11.98 µm is plausible, because the microcavity length was adjusted to a value in the range of 14 to 16 µm at the bare mirror, and then, the mirror is moved laterally, to incorporate the membrane into the microcavity.
With these values, the diamond-only resonances λ_d and air-only resonances λ_d can be calculated [van Dam et al., 2018]:

$$\lambda_a(q_a) = \frac{2t_a}{q_a} \qquad \lambda_d(q_d) = \frac{4n_d t_d}{2q_d - 1} \tag{5.2}$$

The spacing of these modes lead directly to the air gap lengths t_a and the diamond thickness t_d [Janitz et al., 2015]:

$$\Delta\lambda_a = \frac{\lambda^2}{2t_a} \qquad \Delta\lambda_d = \frac{\lambda^2}{2n_d t_d} \tag{5.3}$$

The corresponding air-only and diamond-only modes are plotted into fig. 5.5. The mode order of the air cavity q_a and the diamond cavity q_d add up to the hybrid mode order q = q_a + q_d. The total microcavity length results in $d = t_a + t_d$ = 13.94 µm for a zero length detuning. A full three-dimensional model, which considers the wavefront curvature inside the cavity and the full dielectric mirror stack, would give a more precise description [Janitz et al., 2015].
All diamond membranes show interference fringes in the light microscope pictures (fig. 5.3, 5.2 and 5.6). They can be associated with a fluctuating thickness of the membrane. One can also imagine that the interference pattern emerges by an additional air layer between membrane and mirror, so that the light has to pass a coupled system of air-diamond-air cavities. However this would have an significant influence on the dispersion relation and is not observed at any position on the BW piece. Hence it is assumed, that a varying thickness gradient leads to the fringes.
This is also confirmed by the measurement of LDTS on several positions on the BW shown in figure 5.6. The corresponding LDTS are collected in figure 5.7. The LDTS can be attributed to the different kinds of modes at the SiV^- ZPL wavelength of 737 nm, introduced in the theory 2.2.2:

- **"air-like" modes**: steeper slope at 737 nm. This is measured for LDTS (1)-(3) in 5.7 and the positions correspond to the darker fringes in the light microscope image of the BW in 5.6
- **"diamond-like" modes**: shallow slope at 737 nm. This is closely measured in LDTS (5)-(6) in 5.7 and (0) in 5.5. The positions correspond to the bright parts in 5.6

In that way, the diamond-like mode can be selected by the appropriate diamond thickness. This mode is better suited for coupling SiV^-, because the light field is more concentrated inside the diamond-cavity, which leads to a better coupling to the microcavity.
van Dam et al. [2018] showed that an anti-reflection coating of the diamond surface can remove the mode mixing. The dispersion becomes linear with a less steep slope than for the empty cavity case. This would lead to a compromise between low losses and a electric high field intensity inside the diamond membrane.

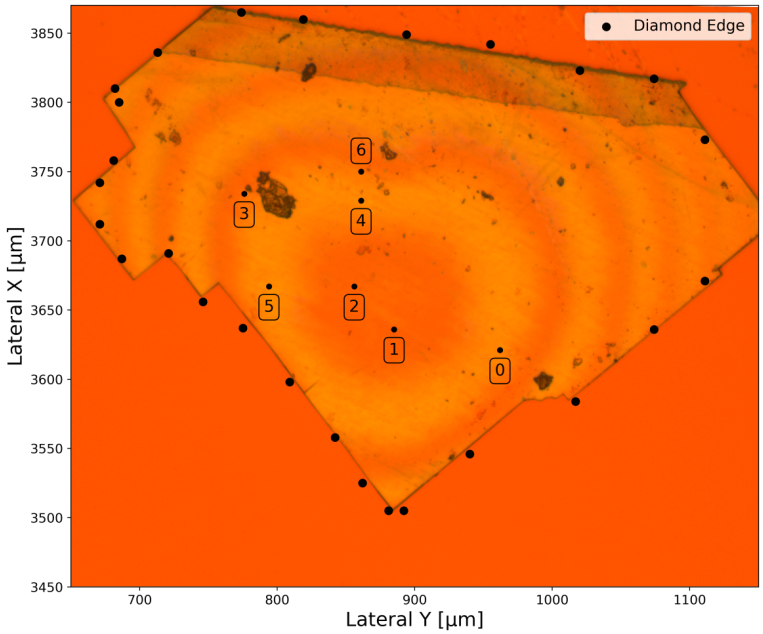

Figure 5.6.: Light microscope of the BW sample and overlay of the positions, where the dispersion relation is measured. The map is aligned by the transitions from membrane to bare mirror.

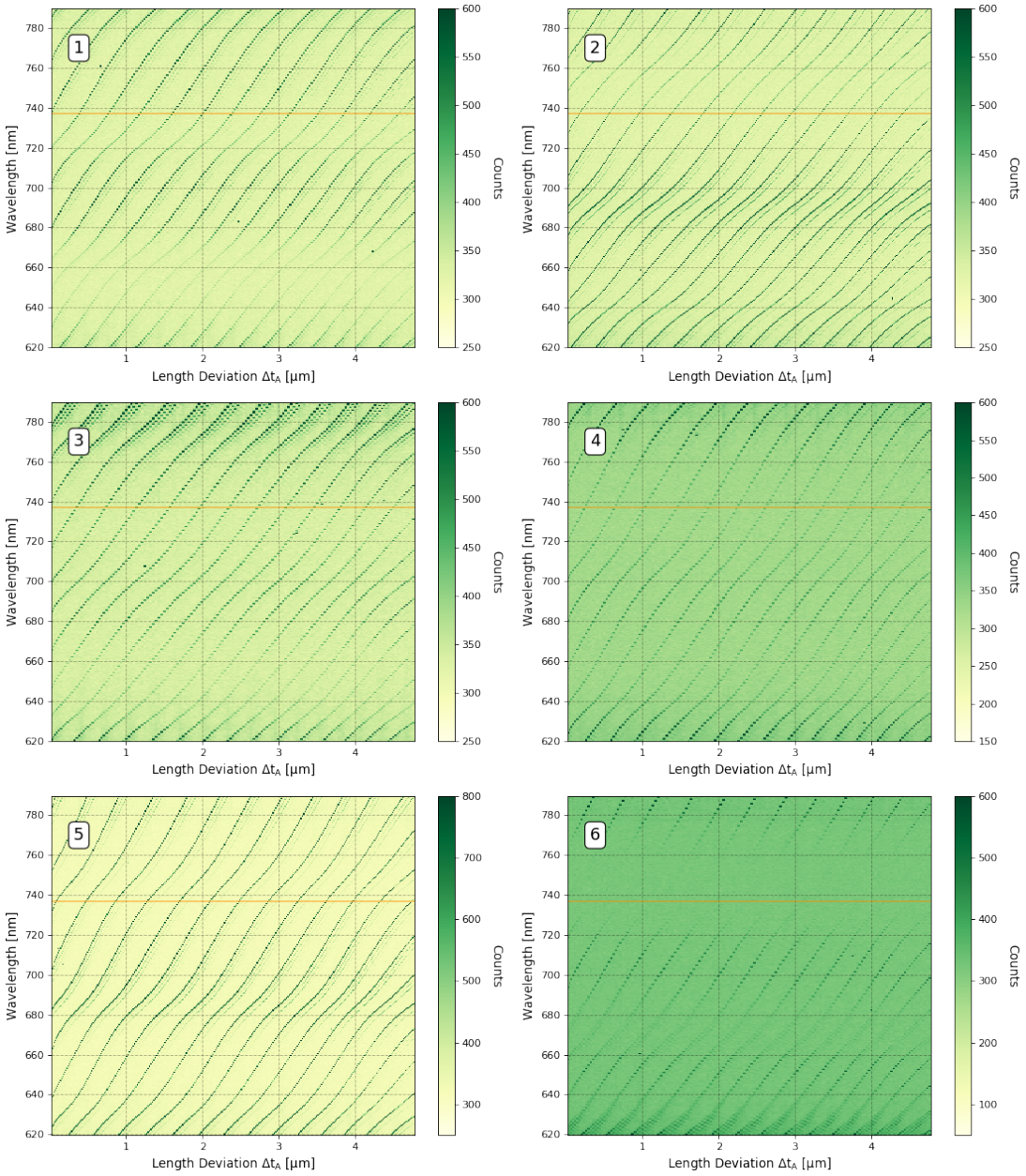

Figure 5.7.: Dispersion relation of the hybrid system of the microcavity and the diamond membrane. The positions on the diamond membrane corresponding to the LDTS is shown in figure 5.6, related by the numbers in the upper left. The microcavity length is detuned in a range of 16-9 µm, which changes the air gap Δt_A. The SiV^- ZPL at 737 nm, indicated by the orange line, shows the diamond and air like character at this position on the diamond membrane.

6

Silicon Vacancy Centers Coupled to the Microcavity

This chapter provides the measurements of the SiV^- *ensembles in the diamond membrane coupled to the microcavity. Before the sample mirror was integrated into the setup,* SiV^- *were detected with confocal microscopy by Morgane Gandil in Christoph Becher's group at the Saarland University. Single* SiV^- *were not found in the lower implanted region, despite some single bright spots in the confocal scans. During the transport from Mainz to Saarbrücken two sample fell off from the mirror. Because of the debris on the the remaining laser cut membrane window, only the BW piece is used for* SiV^- *measurements.*
First, SiV^- *are searched at room temperature. This leads to the extension of the setup by a longpass filter (first section). Next, the sample is cooled to LHe temperature. During the cooldown and heatup process, the* SiV^- *emission is also measured at temperatures in between (section two). A saturation of the* SiV^- *ensembles is measured for different implantation doses (section three) and a lifetime reduction for a resonant microcavity is shown in the last section.*

6.1. Photoluminescence at Room Temperature

Figure 6.1 shows one of the first Length Dependent Transmission Spectrum (LDTS) after finding the SiV^- emission inside the diamond membrane BW sample. The piezo expansion is calibrated (see appendix A.10) to transform the applied voltage to a microcavity length deviation (x-axis). In that way, the microcavity is scanned over several FSR, which leads to the modulated appearing of the SiV^- ZPL at 738 nm, which corresponds to a deviation of $\Delta L = (738/2)$ nm $= 369$ nm. The coating of the microcavity has a transmission of 71 % at the off-resonant excitation at 532 nm. Because of that, the green light can also pass the microcavity (finesse of ≈ 2) and the SiV^- excitation is modulated by this cavity effect. The LDTS shows more counts at lower wavelength due to residual background emission from the fiber, because of the green excitation.
It is found that launching green light form the fiber for PL spectra is more convenient, while in principle, it can also be done through the MM. However the MM has a much larger core diameter (50 µm instead of 5 µm mode field diameter for the SM fiber). For coupling green light in by the MM through the aspheric lens, the beam waist diameter on the membrane can be mapped minimally to the diameter of the MM. So it is limiting the available light intensity in the area of the mode volume of the microcavity.

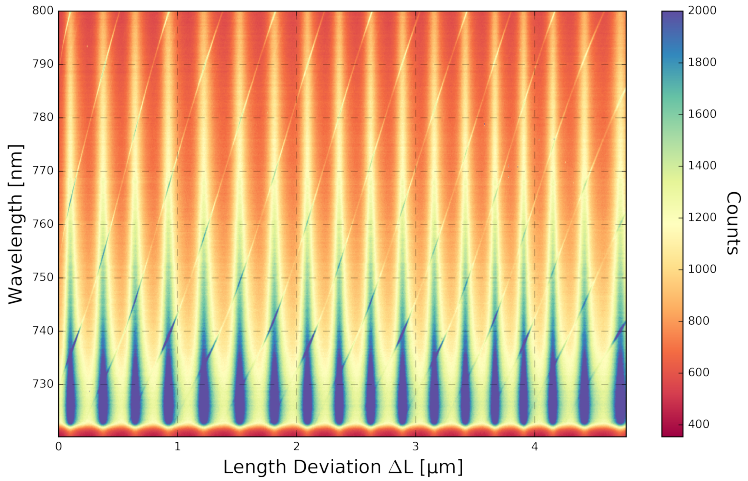

Figure 6.1.: SiV^- PL emission at room temperature. The LDTS is recorded with a longpass filter cutting at 715 nm in front of the spectrometer. The SiV^- ZPL at 738 nm is strongly overlapped with the parasitic background emission of the detection fibers, which contributes with the same amount to the signal from 715 nm to 725 nm.

Comparing this with the PM fiber (NA of 0.13 leads to an acceptance angle of θ = arcsin(NA)=7.5 degree), the spot size of the green light for a typical microcavity length of 20 µm on the membrane is ≈ 5 µm. Ignoring the (small) cavity effect, the power density scales quadratically with the spot diameter, so the off-resonant excitation is much stronger for launching the light from the fiber side.
Usually, an off-resonant excitation power of 2-6 mW is used before the fiber breakout box (see appendix A.6). The fiber-fiber coupling (both, transport fiber from optical setup to cryostat and fiber inside the cryostat are PM fibers with comparable core diameters), the splicing of the PM transfer fiber to the SM fiber and the length dependent mode matching of the microcavity lead to additional losses. If the microcavity is resonant for 532 nm light, it can pass and get to the detection setup. During traveling through the fibers, the green light leads to additional emission of impurities in the fibers, especially in the detection MM fiber (further investigation in appendix A.9). Thus, the emission background from the fibers is very dominant in fig. 6.1, modulated by (532/2) nm, which are of the comparable intensity as the SiV^- emission.
The easiest way to prevent that the excitation light enters the detection path, is to choose an asymmetric DBR coating of the cavity. In our case, a second stopband must be added to the mirror coating to cover 532 nm with a high reflectivity. Then, the light is blocked, which results in a much lower background and a excitation much less depending on the microcavity length.

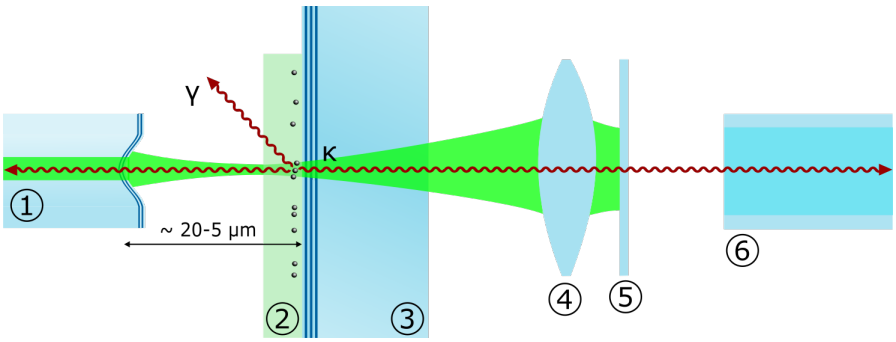

Figure 6.2.: Optical path in the experimental insert with integration of the longpass filter. For PL, the green off-resonant excitation light is coupled in from the fiber (1) and exciting the SiV^- ensembles inside the membrane (2) bonded to the macroscopic mirror (3). The red SiV^- emission is focused by an aspheric lens (4) on the MM (6) to the spectrometer. A longpass filter (5) prevents the green light from entering the MM fiber. Figure is not drawn to scale.

A new coating is expensive and time-consuming and the diamond membrane can not be transported from mirror to mirror. So the way around is an addional longpass filter integrated to the mirror side of the microcavity, sketched in figure 6.2.
The filter is cutting at 650 nm and suppressing the green excitation at 532 nm to a transmission of 100 ppm (optical density of 4). This reduces the fiber background emission a lot and the SiV^- signal can appear in a very clear manner in the LDTS, like shown in 6.3. The previously observed fiber emission is not visible any longer. For these measurements, a longpass filter at 715 nm right before the spectrometer is used. This filter is not necessary any longer after integrating the longpass at 650 nm directly to the experimental insert.

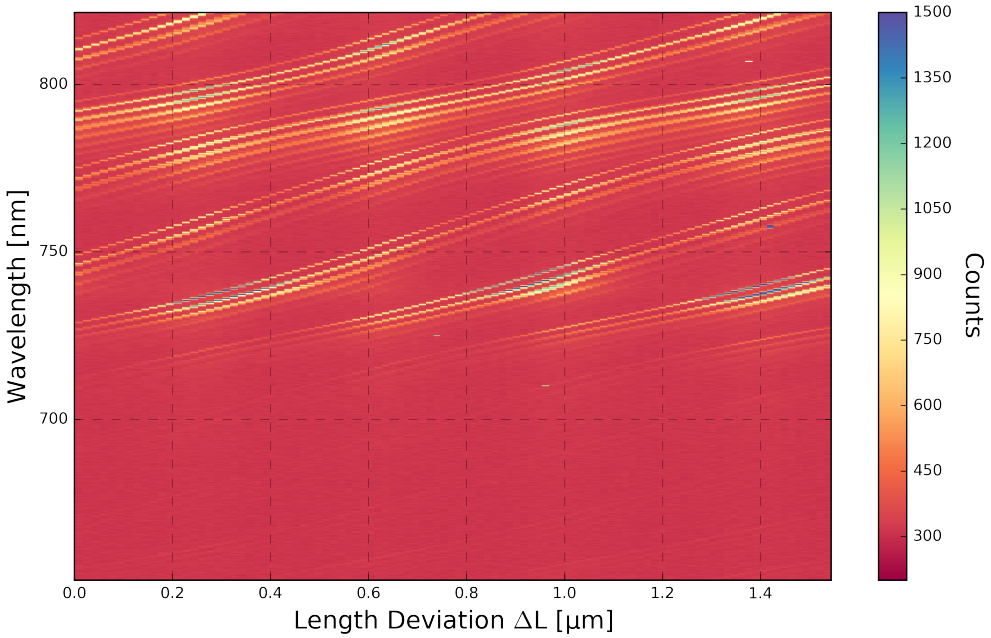

Figure 6.3.: SiV^- emission at room temperature after the longpass filter is placed into setup. The previously observed background emission from the detection MM after the microcavity disappeared. The SiV^- are emitting around their ZPL at 738 nm with a very broad spectrum. The LDTS is recorded in the spot with the highest implantation density.

Shown in 6.3, the emitters are coupling to the fundamental mode as the brightest line at the SiV^- ZPL and to several higher order TEM. The wavy nature of the dispersion relation, characterized in chapter 5, is visible.
Red shifted from the ZPL, some emission from 740 nm to 820 nm is visible. This would fit to the PSB emission of SiV^-. In the regions with high implantation doses, this signal

becomes more pronounced, while it is not completely vanishing at not implanted regions. Hense, there could be contributions from the daimond crystal itself.
To make sure, that the emission at 738 nm arise from the implanted SiV^- and not from other impurities in diamond like the GR1 vacancy at 741 nm [Jahnke, 2015] (or impurities from the different used fibers), several positions on the BW diamond piece are investigated for the emission peak at 738 nm. The corresponding map is shown in the left side of figure 6.4. The background of the map shows a confocal microscope image of the sample recorded at room temperature. The implanted spots are appearing as bright circles, while their intensity is indicating the implantation doses (see appendix A.2). The positions, where an emission at 738 nm is found match also the spots of the confocal microscopy, while in the not implanted membrane parts, no emission peak appears.
The room temperature LDTS is integrated along the length (x-axis) to obtain a full spectrum, shown in the right of fig. 6.4. The center of a fitted Lorentzian function leads to a center position at 739 nm with a linewidth of 6.2 nm. The single spikes in the spectrum can arise from not reproducible spikes from the CCD camera, suggeting tgese are cosmic counts. This effec becomes more pronunced especially for longer exposure times (> 10 s). For SiV^- ensembles at room temperature, the linewidth can be in the range of 6 ± 1 nm [Neu, 2012]. The red shift of the center by about 1 nm can arise from the crystalline environment and may indicate a higher strain in the membrane sample. For strongly strained environments, for instance in nanodiamonds, shifts of the ZPL from 730 nm to 750 nm have been observed [Neu et al., 2011].

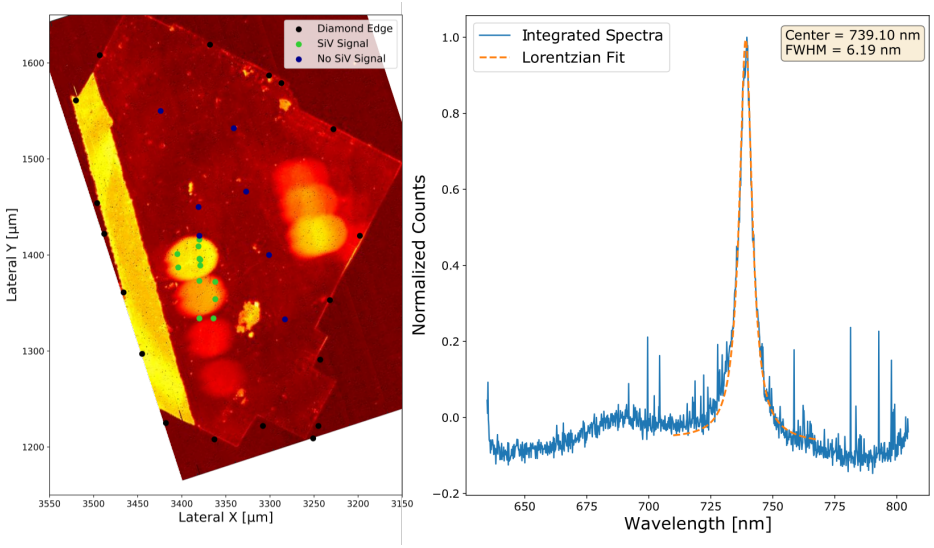

Figure 6.4.: *Left:* confocal microscope scan of the BW diamond sample. The overlapped map shows some lateral points, where the microcavity transmission signal is investigated. The two images are aligned by the membrane edge, which is found by the membrane influence to microcavity dispersion. The green points, where a clear emission peak around 738 nm is measured, coincide with the bright implantation spots, where in the not implanted region, no emission at 738 nm appears. *Right:* Summed spectra of a LDTS to measure the SiV^- ZPL. The line is slightly shifted to the red with respect to values fond in literature [Jahnke, 2015], featuring the room temperature typical broad linewidth.

6.2. Fine Structure at Lower Temperature

To reveal the finestructure of the SiV^- into four narrow sublines, which represent an unambiguous spectral fingerprint of the SiV^- [Neu et al., 2013], the insert with the BW sample on mirror is cooled down.

Between room temperature and LHe temperature, also LDTS at 150 K, 80 K and 60 K are measured. All are shown in 6.6. Despite the values at LN and at room, all of the temperatures in 6.6 are measured by a temperature sensor, which is installed to the highest stage of the cryostat insert (see A.7). It is the only temperature sensor, spanning a range of 4 K $<$ T $<$ 250 K, while the two other sensors only measuring in the range $<$ 6.5 K. For temperatures, where the insert is not completely immersed in the cryogenic fluid, it can be assumed, that a slight temperature gradient is obtained between the stages. Because of this, the temperature values in 6.6 are rounded to the tens, except the LHe, where all temperature sensors are displaying a value around 4 K.

At lower temperature, the cavity needs to be scanned in appropriate small steps over the SiV^- emission, to reveal the complete linewidth. This is shown in figure 6.5. Only

the TEM_{00q} of the microcavity is scanned over the SiV^- ZPL in small steps. At higher temperatures (for 150 K and 300 K), this is not possible, due to the larger linewidth. Here, the spectra are extracted with a tube shape interval around the ZPL, which has same slope like the resonant cavity line. By this way, it is ensured, that only the emission into the fundamental mode is considered.

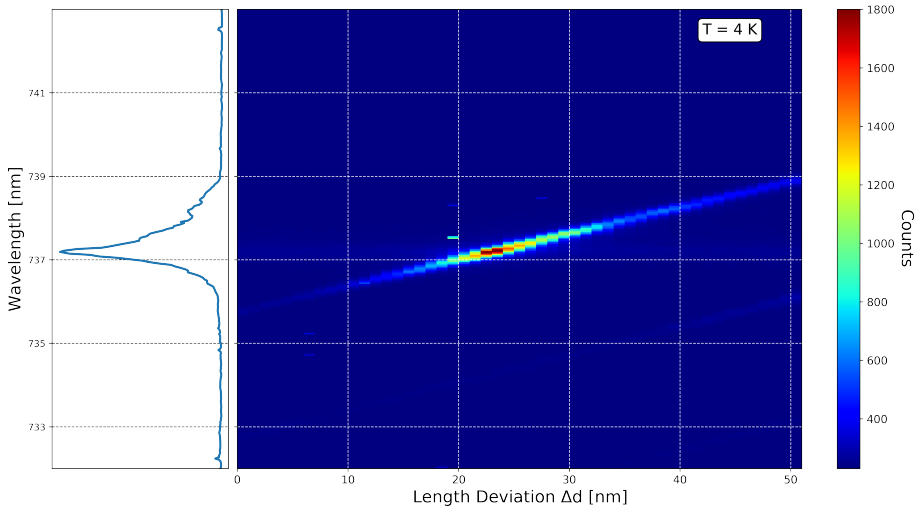

Figure 6.5.: Integration of LDTS over the scanned length range, chosen to overlap only the TEM_{00q}. The microcavity linewidth is at this length ($\approx$ 10 µm) is much narrower then the inhomogeneously broadened SiV^- linewidth. The integrated spectrum for the length deviation of 0 to 50 nm is shown in the left panel. The x-axis represents the intensity in arbitrary units.

The LDTS from 6.6 are used to sum up an integrated spectrum, like shown in 6.5, to end up with the complete SiV^- spectral emission, plotted and fitted in fig. 6.7. From the fits, the center positions with the line splitting and the linewidth can be extracted, revealing their temperature dependence in 6.7.
To resolve the SiV^- linewidth, the detection resolution of the spectrometer must be sufficiently high. The spectrometer has a resolution of 0.06 nm ($\approx$ 33 GHz at 737 nm) according to the specifications (grating with 1200 l/mm). This is lowered due to the transmission outcoupling be the MM, which is fiber coupled to the spectrometer. For a higher resolution, one can think about installing a SM fiber to collected the transmitted signal, because the 3D nanopositioner stack allows for very accurate coupling.

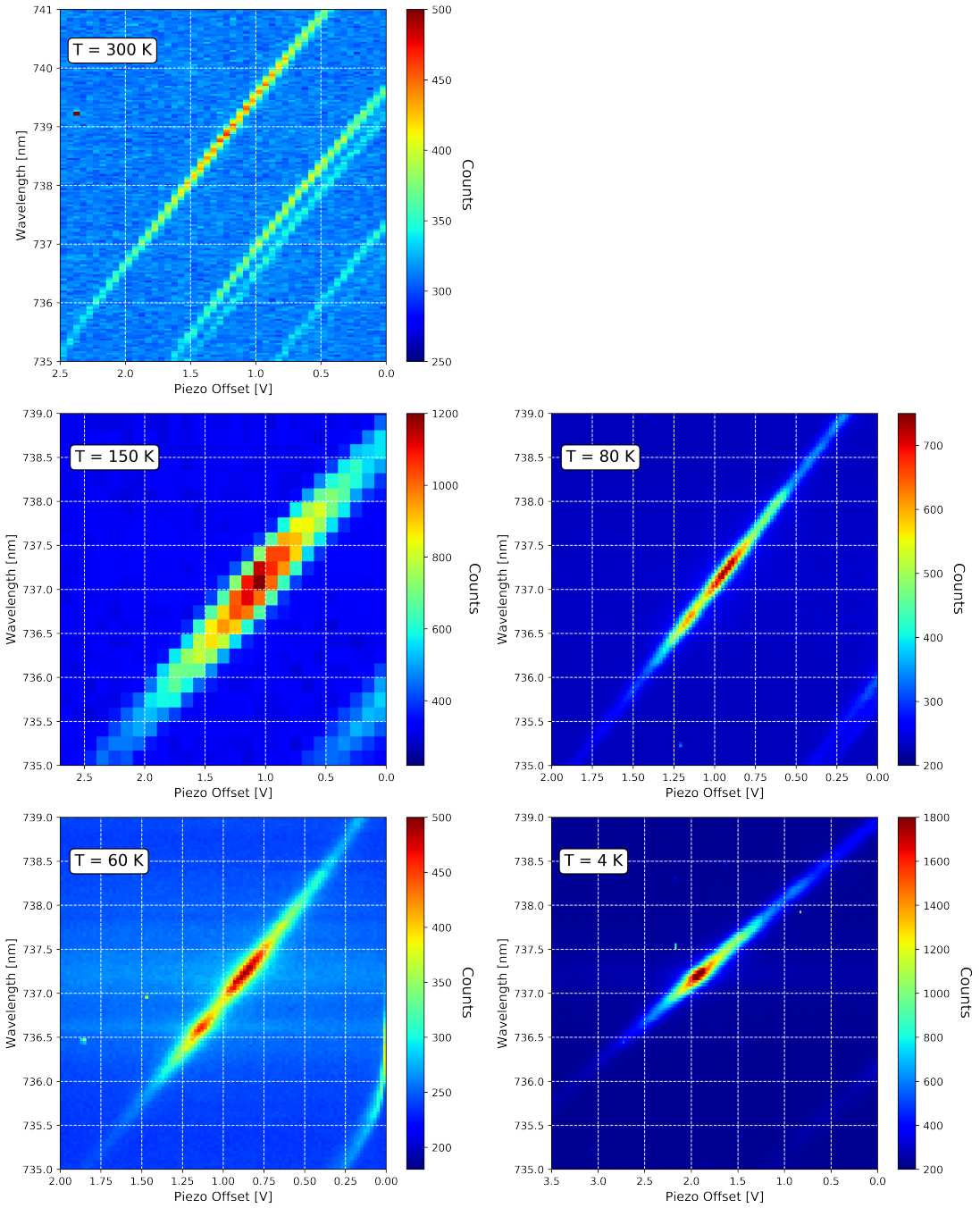

Figure 6.6.: SiV^- ZPL at different temperatures. With decreasing voltage applied to the nanopositioner, the microcavity length is increasing. At room temperature, the scan range of the nanopositioner axis is much longer. Because of the broad emission, also higher order resonances appear in the LDTS. The broad emission at 300 K narrows with decreasing temperature until it is split into a doublet around 100 K. Only one peak is left at 4 K. The first two LDTS are recorded by a grating with lower resolution. All spectra are measured in the two highest implantation spots (BWs0,1 in fig. 6.9).

By sending the DL (linewidth in the range fo 100 kHz) through the resonant cavity and detection MM to the spectrometer, a wavelength resolution in the range of 0.2 nm is measured. According to the literature values for the excited state splitting, this should ne enough to resolve the splitting into the doublet of 260 GHz $\approx$ 0.47 nm (figure 2.3).
All measurements are done with an unlocked microcavity. Because of this, the vibrations contribute to an effective linewidth broadening of the cavity. The vibrations of the unlocked microcavity are measured in chapter 4 to be 250 pm. For a microcavity length of 10 µm, this transforms to a RMS wavelength of 0.02 nm $\approx$ 11 GHz. However, because of this low vibration level, the microcavity don't need to be locked for scanning the SiV^- linewidth.
To extract the SiV^- center λ_0, the linewidth $\delta\lambda$ and splitting (ΔE_g and ΔE_u) from the measured integrated spectra from 6.6, a fit containing four single Lorentzian functions L is used (c accounts for the center, f the FWHM and a the amplitude):

$$L(\lambda, c, f, a) = a \cdot \frac{(f/2)^2}{(f/2)^2 + (\lambda - c)^2} \tag{6.1}$$

The four-fold peaks are split by the ground state splitting ΔE_g into a doublet and each of is split again into a doublet by excited state splitting ΔE_u (level scheme in 2.3). The four peaks are labeled from A to D with increasing wavelength:

$$\begin{aligned} L4(\lambda, A, B, C, D, \delta\lambda, \lambda_0, \Delta E_g, \Delta E_u, off) = \; & off + \\ & L(\lambda, \lambda_0 - \frac{1}{2}(\Delta E_g + \Delta E_u), \delta\lambda, A) + \\ & L(\lambda, \lambda_0 - \frac{1}{2}(\Delta E_g - \Delta E_u), \delta\lambda, B) + \\ & L(\lambda, \lambda_0 + \frac{1}{2}(\Delta E_g - \Delta E_u), \delta\lambda, C) + \\ & L(\lambda, \lambda_0 + \frac{1}{2}(\Delta E_g + \Delta E_u), \delta\lambda, D) \end{aligned} \tag{6.2}$$

A unitary linewidth $\delta\lambda$ of all four peaks is a valid approximation, due to the inhomogeneously broadened lines. In a low strained diamond, the higher energy lines have a slightly broader linewidth due to thermalization between the two excited states [Rogers et al., 2014b].
For the room temperature spectrum, a single Lorentzian peak from function 6.1 is used.

The fits at 60 K and at 80 K lead to a consistent ground state and excited state splitting. Both splittings are temperature dependent [Jahnke et al., 2015], but this can be neglected due to the close temperature values. The fit 6.2 results in a ground state splitting of $\Delta E_g^{60,80K} \approx 0.75$ nm = 397.5 GHz and excited state splitting of $\Delta E_u^{60,80K} \approx$ 1.41 nm = 778.4 GHz. The spectrum at 4 K is fitted by a single Lorentzian function 6.1. The right flank may originate from the PSB or by the ZPL of SiV^- formed by other silicon isotopes (^{29}Si or ^{30}Si), with a red-shifted ZPL [Becker, 2017]. The peaks from the transitions A and B are not any longer visible, due to the low temperature, which freezes out the phononic transitions to the upper level (the excited state splitting of 260 GHz corresponds to a temperature of $\approx$ 12 K [Jahnke, 2015]).
The much higher doublet splitting values from 60 K and 80 K are a strong indication for strain in the diamond membrane. Sohn et al. [2018] and Meesala et al. [2018] showed with implanted SiV^- in a nano-electro-mechanical cantilever system, where strain can be applied by a DC voltage: strain along the SiV^- axis shifts the ZPL and strain transversal to the SiV^- axis leads to higher ground and excited state splitting. The fitted values indicate, that both strain effects appear in the diamond membrane, while the transversal strain is more dominant. The ZPL follows the expected blue shift during cooldown [Jahnke et al., 2015] until it settles at 736.9 nm. This matches very well to the cubic dependence to the temperature. The fitted function 736.9 nm + $6.67{\cdot}10^{-8} \cdot T^3$ [nm/K] is shown in 6.7. The linewidth dependence on temperature has, as well as the ZPL position, a cubic dependence [Jahnke et al., 2015]. The fit is shown with the corresponding measured linewidths in 6.7. The fit function 0.6 nm + $1.63{\cdot}10^{-7} \cdot T^3$ [nm/K] describes the temperature behavior of the linewidth, which devolves for temperatures below 70 K into a linear dependence. Due to inhomogenous broadening and strain, the splitting is with 0.48 nm = 265 GHz much broader at 4 K, compared to the literature value.

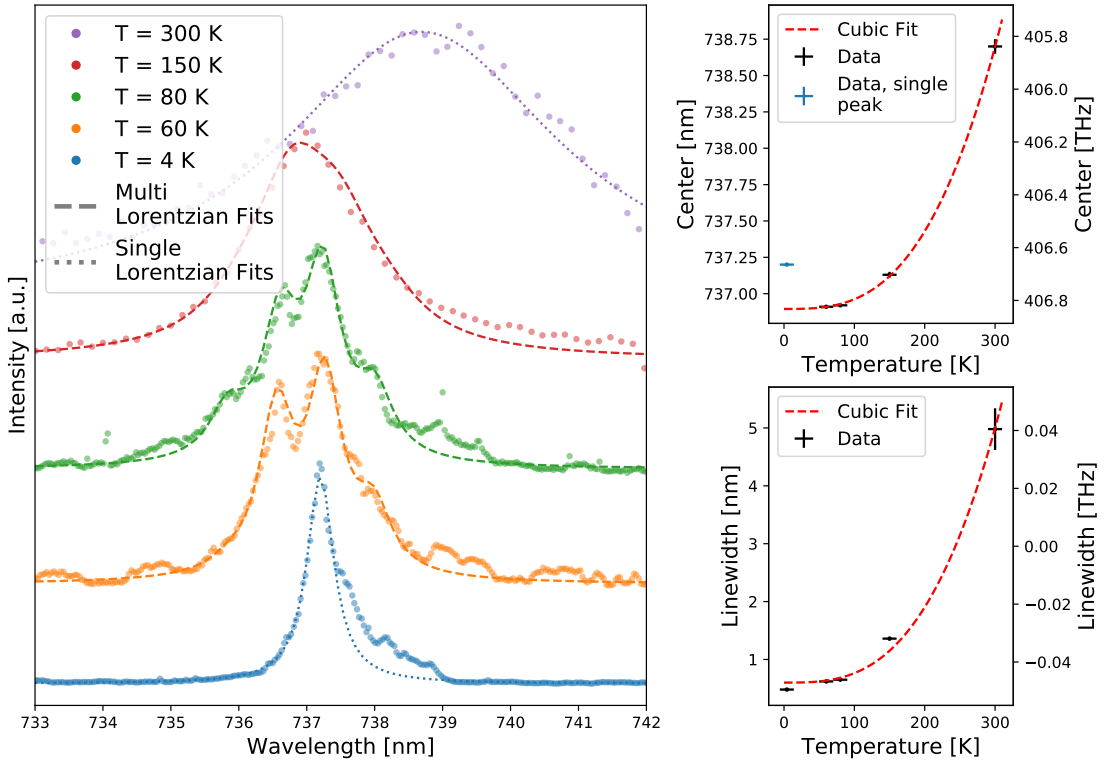

Figure 6.7.: *Left:* ZPL of SiV^- ensembles at different temperatures in the two highest implantation spots (BWs0,1 in fig. 6.9). The spectra are fitted by a multi Lorentzian function (see text) to regard the SiV^- splitting into four peaks at lower temperature. At 4 K and at room temperature, a single Lorentzian fit is used. The corresponding LDTS are shown in fig. 6.6. The fits are used to extract the ZPL center and the linewidth, which are plotted on the *Right:* SiV^- ZPL center position and linewidth. The data is in good agreement with the cubic temperature dependence from the literature [Jahnke et al., 2015]. At 4 K, only the C-D peak appears in the spectrum, so a center position can not be found. For the linewidth, the temperature behavior becomes linear for $T < 70$ K.

In-grown Silicon Vacancy Centers

The BW diamond sample contains also a region at the edge with in-grown SiV^-. They originate from silicon in the chemical vapor deposition chamber, where the membrane was fusion to the diamond scaffold (see also fig. A.4). A typical LDTS at the edge is shown in figure 6.8. It shows not the common dispersion relation between lengths and resonant wavelength. The same behavior is observed at other positions at the BW edge. It is supposed to be connected to the surface roughness at this area, because this part most probably has a much higher RMS surface roughness than the membrane. This

would explain, why there is no cavity effect in the LDTS. This would mean, that this is the small part of SiV^- fluorescence, which is transmitted by the mirror (about 0.5 %). The amount of SiV^- is not known, but from their high intensity in the confocal microscopy 3.5, it can be estimated that the density is much larger than in the implantation spot with the highest doses[1]. Assuming an annealing yield of 1 %, the in-grown SiV^- ensemble would have a density higher than 10000 $SiV^-/\mu m^2$. The ingrown spectrum is also fitted by eqn. 6.2, shown right in figure 6.8. The ZPL is shifted to nearly the same value from the implanted SiV^-, indicating some strain along the SiV^- axis [Meesala et al., 2018]. In contrast, the in-grown ground state splitting reveals a value of $\Delta E_u^{4K,grown} \approx 0.45$ nm = 248 GHz, which matches very well the literature value. This could be explained by much fewer transversal local strain, which is present in the region of the in-grown SiV^-. The linewidth is with $\delta\lambda \approx 0.33$ nm = 182 GHz smaller then the implanted SiV^- linewidth and features inhomogenous broadening due to the high SiV^- density.

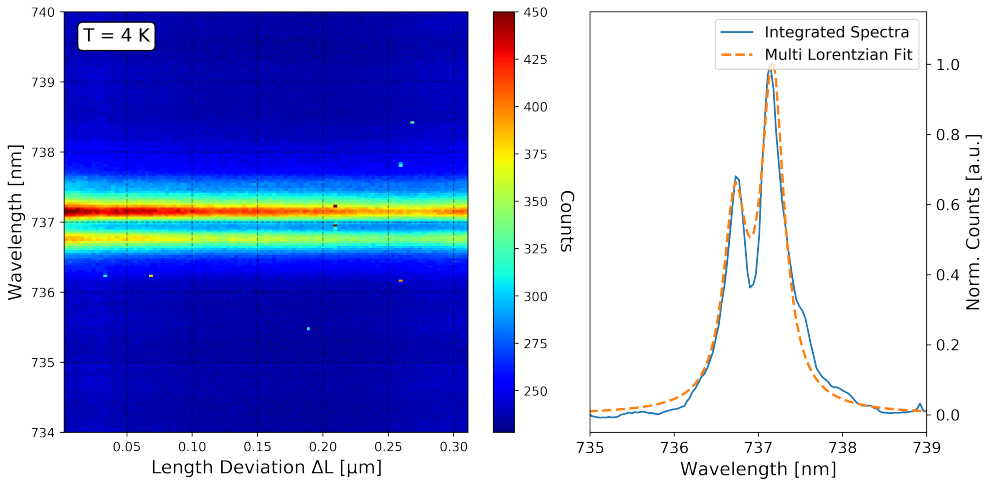

Figure 6.8.: ZPL of in-grown SiV^- ensemble in the edge of the BW. *Left:* no cavity effect is visible in the LDTS, probably due to a bad surface quality, which causes too much losses. *Right:* normalized spectra, integrated over the complete LDTS with a multi Lorentzian fit 6.2. The excited state splitting into a double is very clear and with $\Delta E_u \approx 250$ GHz in good agreement with the literature [Jahnke et al., 2015].

[1] One can also suppose, that the hight surface roughness diminish the total interal reflection, like for SiV^- in nanodiamonds.

6.3. Saturation Effects in Silicon Vacancy Center Ensembles

A similar map like at room temperature (fig. 6.4) is measured at LHe. During the cooldown, one of the lateral nanopositioner axis, which holds the sample mirror, got stuck. Because of this, int was only possible to scan along one lateral axis. In every implanted region, a SiV^- ZPL is found, where the signal strength corresponds to the implantation dosis. The SiV^- signal strength for a resonant microcavity strongly depends on the exact position on the diamond membrane, affected by the surface roughness and contamination. Furthermore, the membrane thickness determines, if a diamond-like oder air-like mode is dominating at this position, which changes the rate of photons leaving the cavity through the plane mirror to the detection path.
A different ensemble SiV^- density has an influence on the laser saturation power of the SiV^- ensemble, needed for off-resonant excitation. To measure this, LDTS for different excitation powers are recorded in the implantation spots BWs0 and BWs3b. The spectra are integrated (fig. 6.5) and the height of the obtained Lorentzian distribution is shown in figure 6.10. The signal height in BWs0 with the highest implantation dosis is linear to the excitation power. The data is measured in a microcavity lengths of about 10 µm, which leads to a cavity waist on the mirror of about 2 µm (formula 2.10).

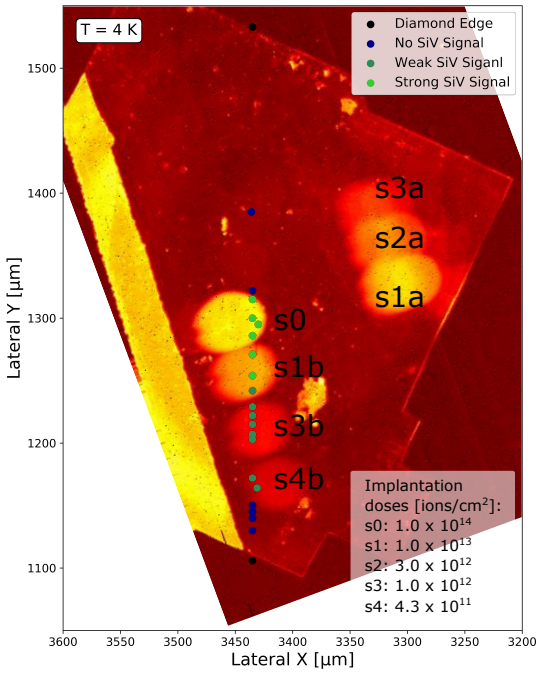

Figure 6.9.: SiV^- emission on BW at 4 K. A SiV^- signal is found in the four highest implanted b-spots. Because of a stucked nanopositioner axis, only one lateral direction can be used. In a second cooldown, an SiV^- signal is also measured in the right spots s1a-s3a. The corresponding implanation doses is shown on the right, lower legend. The background image is measured by confocal microscopy (see also A.4).

In BWs3b, where the SiV^- ensemble density is two orders of magnitude lower, a saturation is visible. The amount of SiV^- inside the microcavity can be estimated for both implantation spots:

- BWs0: 10^{14} ions/cm^2 = 10^6 ions/µm^2 $\xrightarrow{1\,\%\,\text{yield}}$ 10^4 ions/µm^2 $\xrightarrow{\text{waist}}$ $\approx 10^5$ SiV^-
- BWs3: 10^{12} ions/cm^2 = 10^4 ions/µm^2 $\xrightarrow{1\,\%\,\text{yield}}$ 10^2 ions/µm^2 $\xrightarrow{\text{waist}}$ $\approx 10^3$ SiV^-

Here the spreading of the implantation depth is not considered (simulated with SRIM in A.2: straggle of 17.6 nm around the position of the intracavity light field antinode inside the membrane). To extract the off-resonant excitation power needed for saturation, the measured data can be fitted by [Demtröder, 2000]:

$$\text{Counts}(P) = \frac{C_{inf} \cdot P}{P_{sat} + P} + \alpha \cdot P \tag{6.3}$$

C_{inf} accounts for the count level in the limit of high excitation power, P_{sat} leads to the power needed for saturation and the last term account a linear background. The ensemble with lower SiV^- density saturated for a off-resonant excitation power of 2.4 mW. The excitation power is measured before the fiber breakout box. Losses behind can occur due to the fiber-fiber coupling (both are PM fibers with comparable core size), the splicing of the transfer PM inside the cryostat and the microcavity SM and the mode matching to the microcavity.

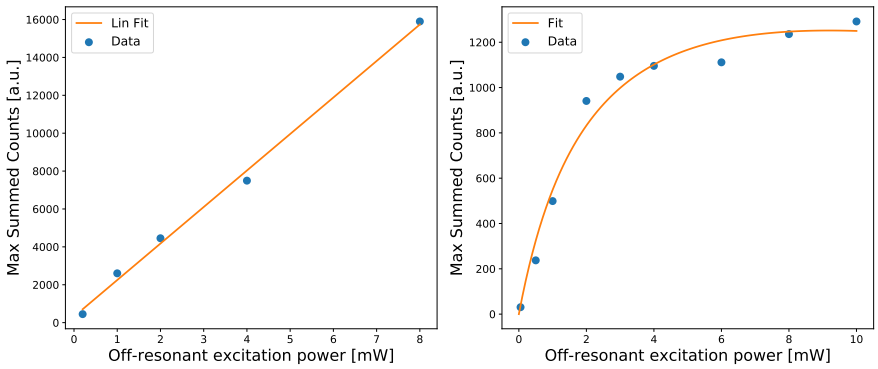

Figure 6.10.: SiV^- ensemble saturation at 4 K. *Left:* Excitation in the highest implantation spot (BWs0 in fig. 6.9) shows no sign of saturation with attainable optical laser powers. *Right*: Excitation in a spot with lower SiV^- density (BWs3b in fig. 6.9) reveals a saturation for an off-resonant excitation power higher than 2.4 mW. Excitation wavelength is 532 nm.

6.4. Purcell-reduced Lifetime of the Silicon Vacancy Center Ensemble

Incorporating an emitter into the cavity, reduces the lifetime of the excited state, if the cavity is resonant to the transition (see theory sec. 2.3). For a strong Purcell-enhanced emission into the cavity mode, high finesse and a low mode volume are required (eqn. 2.20). Both conditions can be fulfilled in the microcavity, with the Purcell-factor as figure of merit for quantifying the performance of the system. For the application as an efficient light-matter interface, a well coupled emitter to the cavity is needed to construct for example a reliable readout of the SiV^- spin state [Nguyen et al., 2019b].
In order to determine the Purcell-factor, the SiV^- ensemble lifetime of the excited state can be measured for a resonant and off-resonant microcavity. The measurement is done for LN temperature. In that way, the SiV^- ZPL is sufficiently narrow enough and the lifetime is not as short as at room temperature, which makes the requirements to the timing resolution of the measurement electronics lower. At room temperature, the SiV^- lifetime is usually around 1.1 ns [Jahnke et al., 2015]. Lowering the temperature leads to a saturation at 1.55 ns for temperatures below 100 K [Jahnke, 2015]. The lifetime is affected by the local environment in the diamond lattice due to strain and can vary around these values.
The lifetime measurement setup is as follows: for the off-resonant excitation, a pulsed green laser (PicoQuant LDH-P-FA-530B[2]) is used, which has a pulse width lower than 100 ps. In that way, the laser pulse has a falling flank, which is much faster then the SiV^- lifetime. This enables to extract the excited state lifetime out of the exponential decay of the detected signal by an APD. The pulsed laser is fiber coupled to the fiber breakoutbox (overview in 3.1). The excitation light is launched through the SM of the microcavity, while fluorescence is detected from the mirror side. The detection MM is fiber coupled to the spectrometer. Before every time-resolved measurement, its is ensured, that the microcavity is matched to the ZPL. For the time-resolved lifetime measurement, the detection MM is connected to a small setup on the optical table, where the light is out-coupled, spectrally filtered and measured by a APD (Perkin Elmer SPCM-AQR[3]). To prevent blending of the APD, the setup is completely closed by blackout material. For spectral filtering of the excitation light, three filters are used: one to the experimental insert integrated longpass filter cutting at 650 nm (figure 6.2) and two filters inside the

[2] pulsed diode laser,emitting at 531 ± 3 nm with < 1 nm spectral width at 40 MHz, repetition rate of 31.25 Hz to 80 MHz
[3] 100 cps dark count, 50 ns dead time, about 65 % photon detection efficiency at 737 nm

detection box: a longpass filter cutting at 715 nm and a bandpass filter, transmitting at 720 nm to 738 nm. It that way, it is ensured that only light in the spectral window from 720 nm to 738 nm can get to the highly sensible APD.
On the electronic side, a time-correlated single photon counting system (PicoQuant PicoHarp 300[4]) is used. The pulsed laser controller (PicoQuant PDL 800-D) is connected to the first channel to synchronize the fired laser pulses, while the APD is connected to the second input. The APD BNC output is sending a TTL signal between 0 V and 5 V. This is converted by a home-built TTL to NIM converter (logical zero is 0 mA, 0 V at 50 Ω, logical one is -12 mA to -32 mA, -0.6 V to -1.6 V at 50 Ω). Additionally, the laser trigger signal is attenuated by 8 dB, to be at the same level height like the APD signal. The signal height should be the same for both channels to ensure a good operation of the counting system. The PicoHarp is controlled by a PC.
To estimate the timing resolution of the complete system, a calibration measurement is done. The green, pulsed laser is strongly attenuated and sent to the APD to record the laser pulse width along the same fibers that are used in the time-resolved lifetime measurement. Due to a higher single photon timing jitter of the APD, the laser pulse width can not be measured. The time resolution of the complete system is measured to be 0.86 ns. This should be sufficient due to the expected longer SiV^- lifetime. In the data analysis, a deconvolution of the signal can lead to even higher timing resolution.
The SiV^- ensemble lifetime is measured in the implanted spots s0 of the BW sample (see fig. 6.9). For the resonant case, the microcavity is set to enhance the emission at the A-B or C-D peak in the SiV^- spectrum. The counts for pulsed excitation is shown in 6.11. The C-D transition shows a similar behavior. For the resonant microcavity in a length of 12 µm, a count rate of 5 kcps is measured. At about 5 µm for an off-resonant microcavity, around 1.4 kcps are measured, mostly from the weak SiV^- fluorescence, which still passes the mirror to the detection path.
To extract the lifetime, the data is fitted by an exponentially modified Gaussian distribution (erfc denotes the complementary error function[5]):

$$\text{Counts}(t, A, \tau, \mu, \sigma, const) = \frac{A}{2\tau} \exp\left(\frac{1}{2\tau}(2\mu + \frac{\sigma^2}{\tau} + 2t)\right) \text{erfc}\left(\frac{\mu + \frac{\sigma^2}{\tau} - t}{\sqrt{2}\sigma}\right) + const \quad (6.4)$$

[4] two input channels (NIM -200 mV to -400 mV), 4 ps time bin width, electrical time resolution < 12 ps RMS
[5] defined as: $\text{erfc}(x) = 1 - \text{erf}(x) = \frac{2}{\sqrt{\pi}} \int_x^\infty e^{-t^2} dt$

In the fit function, A is a scaling factor, μ the center of the distribution and σ the variance of the Gaussian component. τ^{-1} is the rate of the exponential component, controlling the falling time of the right flank, which yields directly to the lifetime τ.

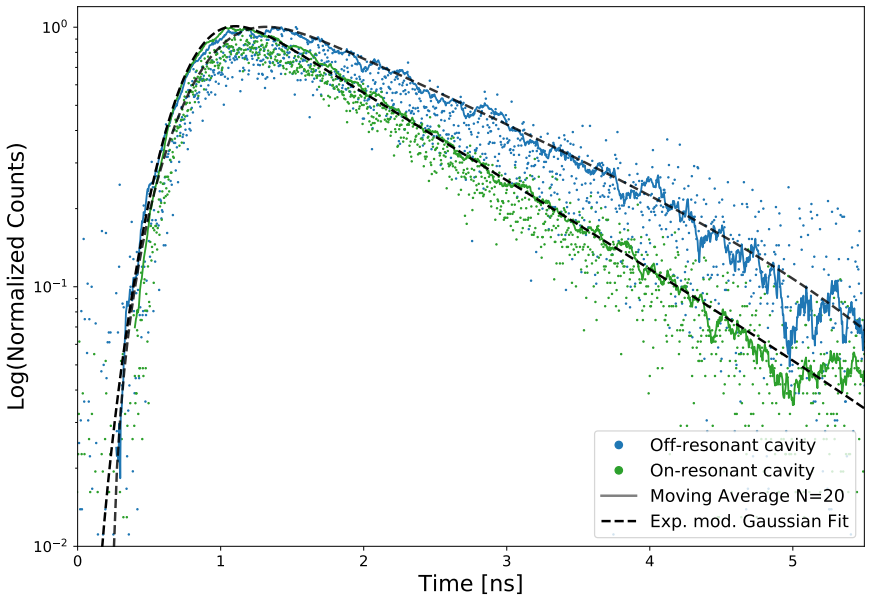

Figure 6.11.: Purcell reduced SiV^- ensemble lifetime for LN temperature. For the resonant measurement, the microcavity is set to enhance the A-B transition in a microcavity length of 12 µm. The off-resonant data is acquired in a length of 5 µm and a far-detuned microcavity. For a clear view, the recorded data in 4 ps bins, is plotted with a moving average over 20 data points. The data is fitted by eqn. 6.4, which yields the following SiV^- ensemble lifetimes: $\tau_{off} = (1.91 \pm 0.03)$ ns and $\tau_{on} = (1.30 \pm 0.01)$ ns.

As expected from the theory (sec. 2.3), the resonant cavity reduces the lifetime. From the resonant and off-resonant lifetime, the experimental Purcell factor can be calculated using eqn. 2.19:

$$F_P^{exp} = \frac{\tau^{off}}{\tau^{on}} = \frac{1.91 \text{ ns}}{1.30 \text{ ns}} = 1.47 \tag{6.5}$$

At the lateral position on the diamond membrane, where the lifetime τ_{on} is measured, a finesse of ≈ 520 is observed. With the lengths of 12 µm, this leads to a quality factor of the microcavity $Q_{cav} \approx 17100$ (eqn. 2.7) with a mode volume of $V_{mode} = 97.5\ \lambda^3$. The mode volume is calculated by eqn. 2.11 with a adapted cavity waist, which takes the influence of the diamond membrane into account, calculated by van Dam et al. [2018]. Due to the influence of the membrane, the waist on the mirror decreases by 2 % to 2.04

µm. The inhomogeneously broadened ensemble linewidth at LN is measured to be 0.65 nm (see 6.7). This results in a emitter quality factor of $Q_{em} = \lambda/\delta\lambda \approx 1100$ and in a effective quality factor of $Q_{eff} \approx 1060$ (eqn. 2.22).
With equations 2.20, where the effective quality factor is used, and 2.24, the expected Purcell-reduced lifetime should be much smaller, with Purcell factor in the range around $F_p \approx 1.05$. For this value, a realistic ZPL emission of $DW = 80$ %, a perfectly aligned dipole in the electric field, $\zeta = 1$ and a SiV^- quantum efficiency of $QE = 1$ has been assumed. In the calculation of ζ, the implantation depth has to be considered too, because this determines the correct position in the antinode of the electric field. The two latter assumptions are not realistic and lead to even lower Purcell factors. The QE of single SiV^- is usually in the range of a few percent [Neu et al., 2012] and is not measured in the experiments presented here.
The low Purcell factors leads to the presumption, that the microcavity is interacts with a subset of SiV^- and not with the complete ensemble. Assuming a much smaller emitter linewidth can lead to much higher Purcell factors, but it is challenging to calculate a estimation, because many of the parameters are unknown.
The lifetime is also measured for different other microcavity lengths. These result are not completely consistent from the expected behavior, but always well below the off-resonant case. There is no obvious effect, which would explain this behavior, because a shorter cavity leads to higher finesse and lower mode volume. Both should directly increase the Purcell factor and thereby reduce the SiV^- lifetime. While it is difficult to give a serious calculation for the concrete Purcell-enhancement, it can be assumed that a lifetime reduction and therewith a Purcell effect is demonstrated.

7

Conclusion: A Robust Platform for Diamond-Photonics Applications

This theses presents the coupling of SiV^- ensembles a microcavity. The coupling is preserved even at lower temperatures, so the opening question can be affirmed. The unambiguous SiV^- fingerprint in the spectral emission for lower temperatures is resolved and ensures that the signal is obtained from SiV^-. The microcavity on the experimental insert in combination with the collection optics for access to and from the cavity, can be denoted as extreme robust, which makes the operation under LHe conditions in high vacuum possible. The apparatus survived more than five cooldowns from an completely open configuration at room temperature to cryogenic tempteratures in vacuum. In every cooldown, the coupling to the microcavity can be quickly and reliably established. Due to the stable operation at cryogenic temperatures, the cryostat environment is well-suited for a variety of diamond-photonics experiments. The fast replacement of the sample mirror makes it very flexible for several diamond sample from nanodiamonds to membranes (see outlook 7.1). It can also be used for experiments with other color centers in diamond, like the NV or the tin-vancancy. Both are in a range of about 120 nm, which could be covered by the stopband of the cavity mirror coatings. This makes it even possible, to use the exact same cavity, for samples with different incorporated colors centers. Within 1-2 days, it is possible to change the sample mirror and cool the system down to LHe temperature.
For a new experimental insert design, one can consider the points already mentioned in sec. 4.3. For the Zeeman splitting into sublevels, coils for a magnetic field needs to be intergrated into the setup. On the other hand, the vector magnet of the cryostat, which is defect, can be repaired. With the magnetic field, the four transitions splits into eight transmissions in the spectrum [Rogers et al., 2014a], where the lower ground state doublet can be used as spin qubit [Sukachev et al., 2017]. A monolithic insert from OFHC (oxygen-free thermanl high thermal conductivity) copper allows the operation at Millikelvin, which makes it possible to observe the long SiV^- spin coherence times in high quality diamond samples. For this measurement, the problem of thermal connection of the diamond sample to the insert has to be solved. The glass substrate is a bad heat conductor below 4 K. For operation below 4 K, the helium gas needs to be pumped out, so there is no contact gas in the IVC. One solution could be to evaporate silver stripes on the mirror, which connects sample over the insert to the baseplate of the cryostat insert.

It is not succeeded to find single SiV^- signal in the low implanted diamond regions so far. One reason is, that the microcavity can not reliable be set to very low length, which would lead to a strong SiV^- signal. The other major reason are the residual background counts from the fibers, which are used to access the cavity. The background emission depends on the fiber core and cladding material, where pure silica fibers tend to be the best option. The emission spectrum is additionally temperature dependent. All this is measured for some fibers in the appendix A.9.
One of the direct next steps with a new diamond sample (and the actual or a new exp. insert) can be to search for single SiV^-. For this, the new sample (sec. 7.1) is implanted with a much lower ion doses to prevent an waveguide effect and create regions with a low SiV^- density. For the measurement, the detection setup is already extended by a second APD, appropriate spectral filters (table C) and a 50:50 beam splitter. A second-order intensity correlation function (g2 function) can be measured with the time-correlated single photon counting module, used in the lifetime measurements. For a better signal, the microcavity should be set to a very small lengths. An excitation closer to the ZPL can also increase the signal to noise ratio.
With single SiV^-, it would be very interesting to do photoluminescence excitation (PLE). Instead of exciting the SiV^- off-resonantly with the green light, here the DL is scanned over the ZPL and the PSB emission (> 740 nm) is detected. The wavelength of the DL can be monitored with high accuracy by the wavemeter, allowing to scan the linewidth in the tens of MHz regime. The microcavity can be set resonantly to peaks in the PSB spectrum [Dietrich et al., 2014]. Due to the low required power for resonant excitation of the SiV^- (below 20 nW [Jahnke, 2015]), the microcavity must not necessarily be resonant for the red excitation light (for a naive assumption, that the mirror of an off-resonant cavity would only transmit the light according to the coating, launching only a power of ≈ 13.5 µW into the microcavity is required).
As a benchmark for the quality of the diamond membrane, one can measure the SiV^- linewidth and splitting into the ground and excited state branch at 4 K with the microcavity. In parallel, one can use implanted spots in the diamond scaffold with the same implantation doses, to investigate the influence of the diamond membrane to the SiV^- properties. Both, $g^{(2)}$ and PLE measurements are promising with the new membrane samples (see 7.1). If they fully bond to the mirror, the microcavity can be set to very low length, only limited by the membrane thickness and the geometry of the fiber tip.

7.1. Outlook: New Diamond Membrane Samples and Bonding Method

Next to the membranes, SiV^- inside nanodiamonds can be incorporated into the microcavity like shown by Benedikter et al. [2017]. The nanodiamond samples used in these experiments suffer from several properties, which makes them not inappropriate for QIP applications, like a large spectral inhomogeneity, blinking or permanent bleaching. Recently, Bolshedvorskii et al. [2019] reported of a high-pressure, high-temperature synthesis to fabricate nanodiamonds with 10 nm size and single SiV^-. They feature non-blinking and a spectrally narrow emission with a narrow distributed ZPL. The low-strain nanodiamonds are investigated by Rogers et al. [2019] at 4 K, showing bulk-like spectral properties. The fine-structure of the SiV^- is observed with an inhomogenous ensemble linewidth below the excited state splitting and stable optical transitions. Nanodiamonds can be spin coated onto the planar mirror.
Two new diamond membrane samples are available for new measurements, shown in figure 7.1. The left sample is fabricated by Julia Heupel from Cyril Popov's group at the University of Kassel. The membrane windows are etched by masks into a CVD diamond slab (Seki Diamond). The membranes have a thickness in the range of 3-5 µm.

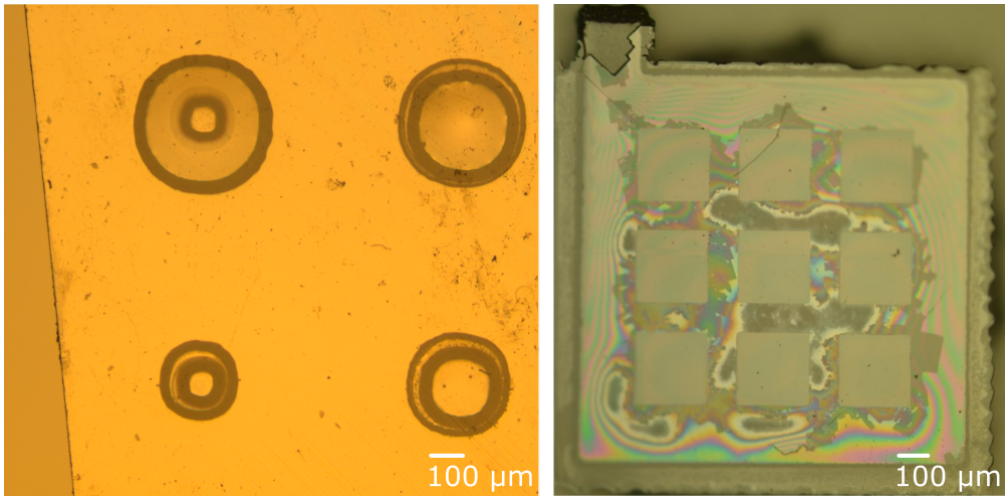

Figure 7.1.: *Left:* New membrane sample from the University of Kassel. Four holes are etched into the diamond to obtain membrane thickness in a range of 3-5 µm. The mask in the last etching step was aligned 90 degrees to the previous positions, which lead to a stairway-like structure. *Right:* New membrane sample from the University of Melbourne. The fabrication method is the same like for the membrane sample, used in this thesis. The rectangular windows have a comparable thickness of 1.3-1.7 µm.

The membrane in the lower left feature a RMS surface roughness of 0.5 nm, measured by atomic force microscopy. This low value is very promising and could lead to extremely low losses at the diamond air interface. Here the membranes with the complete scaffold structure is applied to the mirror. Due to the connection to the diamond slab, the sample can be bonded by a tweezer and methanol to the mirror.
The second membrane sample is similar to the sample used in this thesis provided by Nadarajah Athavan in Steven Prawer's group at the University of Melbourne. It features a comparable thickness of 1.3-1.7 µm with a RMS surface roughness of 0.8-2.0 nm on both sides. Low temperature spectra show a very small peak of in-grown SiV^-.
For the membrane application to the microcavity mirror, a technique developed by Philipp Fuchs from Christoph Becher's group (Saarland University) can be used (sketched in fig. 7.2). The membrane is glued with indium to a micromanipulator probe. Then, the membrane with an arbitrary form is cut out with a focused ion beam and transported by the probe on the mirror surface. All this is done in the vaccum to prevent contamination. If the membrane does not bond directly, it can be pushed by the probe. After the membrane is bonded, the indium part is cut out and removed. In that way, a fully bonded membrane allows for very short microcavity lengths detuning without the risk of electrostatic forces pushing the membranes away. This opens the door for high finesse and low mode volume range of a microcavity.

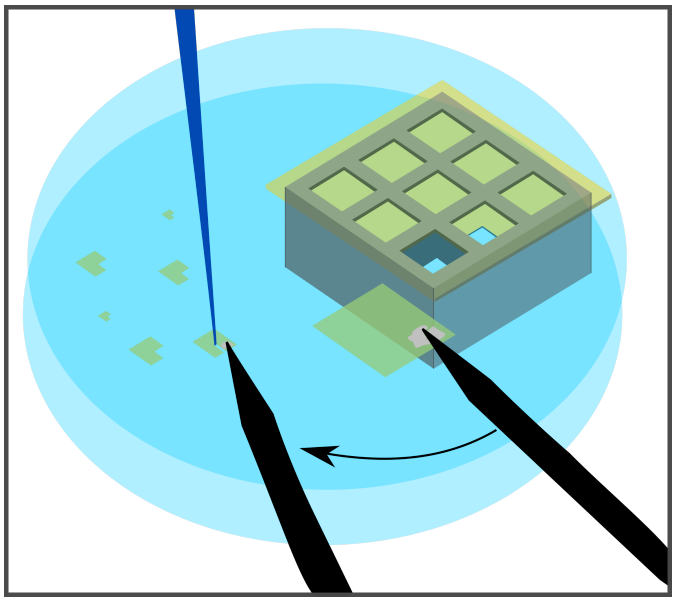

Figure 7.2.: Sketch of a new method for the membrane application to the macroscopic mirror. The complete application is done inside the vacuum chamber of a focuses ion beam apparatus. The membrane is glued by indium to the probe of a micromanipulator and cut out by the gallium ion beam. After attaching it to the mirror, the piece with indium is cut out and removed.

A

Appendix

A.1. Diamond Membrane Sample

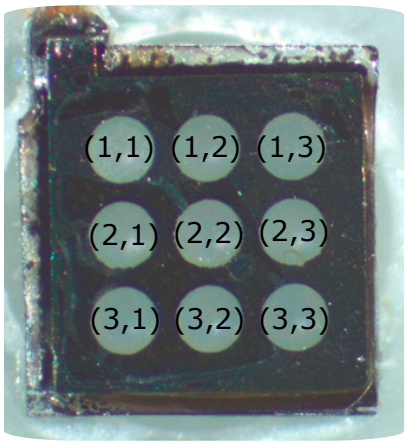

Figure A.1.: Diamond membrane sample with scaffold structure in Melbourne.

Window	Thickness [nm]	Error [nm]
(1,1)	1440	25
(1,2)	1420	30
(1,3)	1400	20
(2,1)	1390	25
(2,2)	1460	30
(2,3)	1420	20
(3,1)	1360	30
(3,2)	1400	20
(3,3)	1340	20

Table A.: Diamond membrane thickness measured in Melbourne.

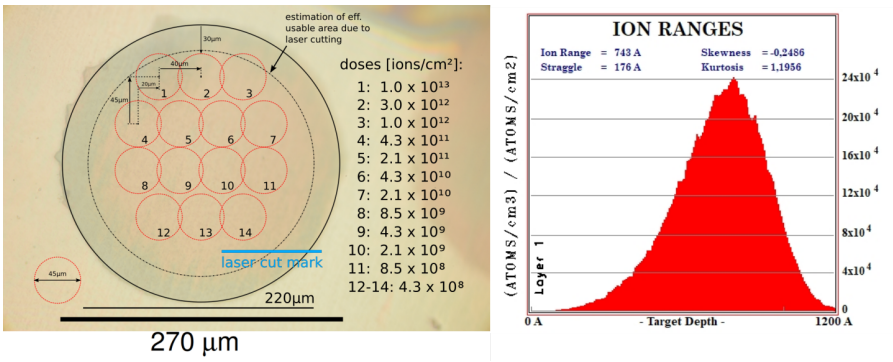

Figure A.2.: Diamond membrane implantation pattern on window and implantation depth of Si atoms into diamond simulated using SRIM. See explanation in section 3.3

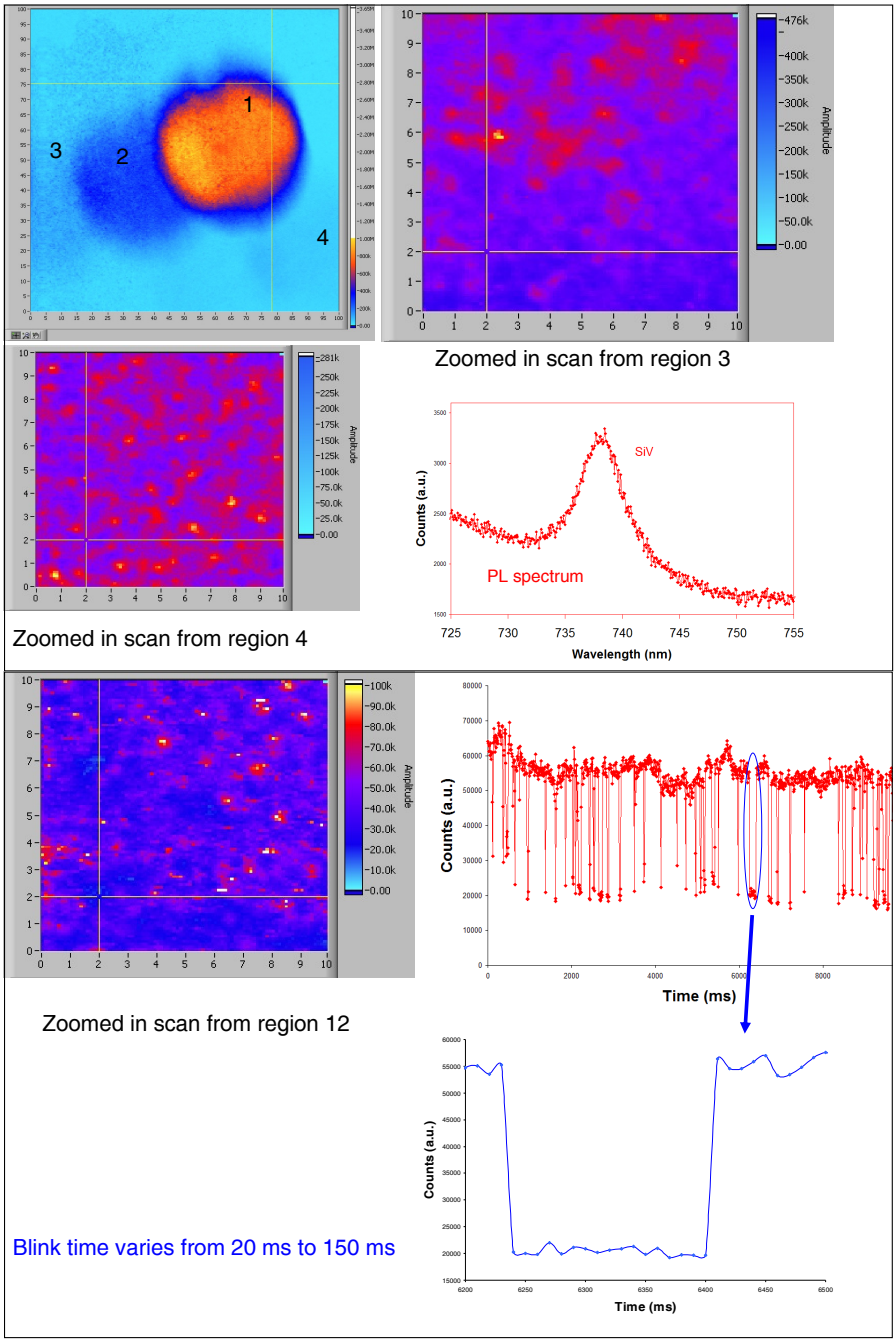

Figure A.3.: Pre-characterization of diamond membrane in Melbourne. A SiV^- ZPL at 738 nm is detected in the diamond windows, where the intensity can be associated with the implantation doses. The SiV^- feature blinking on the time scale of milliseconds.

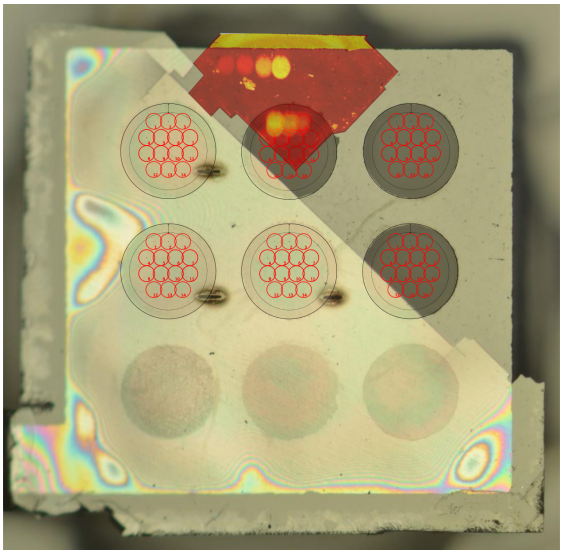

Figure A.4.: Reconstruction of the original position of the broken window piece in the diamond membrane.

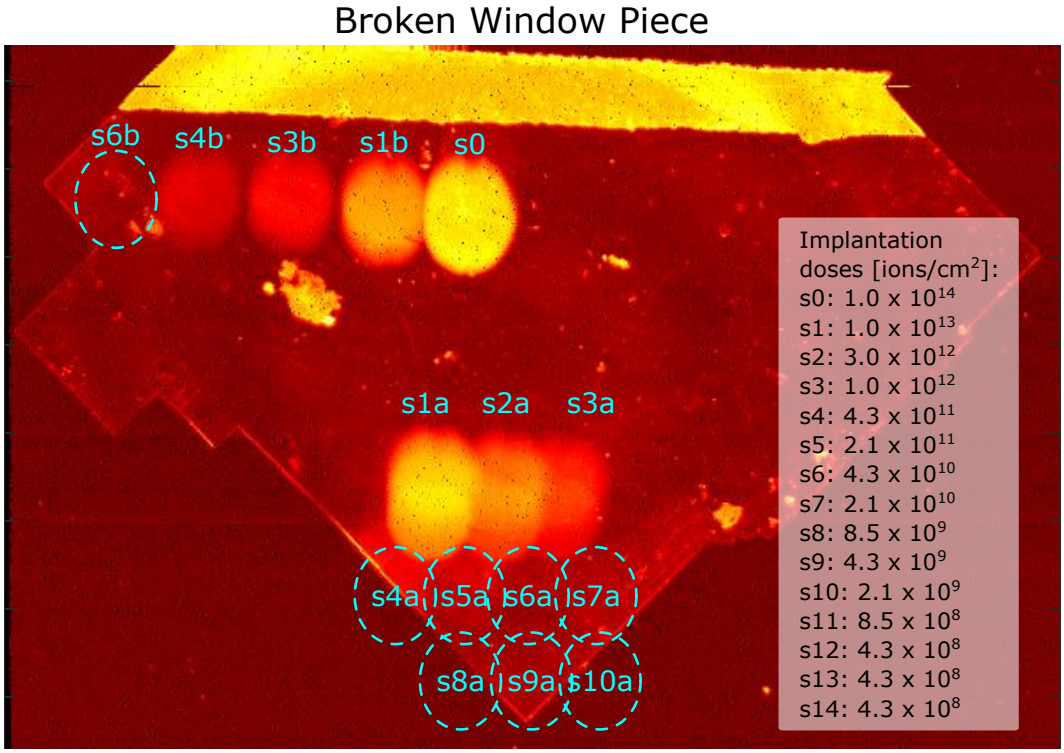

Figure A.5.: Overview of the implantation spots of the broken window piece with estimate of locations of the lower implantation doses.

A.2. Installed fibers

Port	Fiber type	Fiber name	Coupling efficiency	Purpose
P1	MM	Thorlabs FG050UGA	58 % for 737 nm	input/output from mirror side
P2	PM	Thorlabs PM630-HP	70 % for 737 nm	spare for port four
P3	PM	Thorlabs PM460-HP	70 % for 532 nm, don not transmit 737 nm	SiV^- excitation from mirror side
P4	PM	Thorlabs PM630-HP	85 % for 737 nm	Spliced to fiber of microcavity
P5	MM	Thorlabs FG050UGA	82 % for 852 nm	Spare for P1
Not connected	SM	NKT LMA-PM-5	not measured	not used

Table B.: Fibers installed in the cryostat for optical access to the microcavity.

A.3. Optical Filters

Manufacture	Name	Type	Blocking (OD > 5)	OD at 532 nm	Transmission (T > 80 %)	Optical density at 737 nm
Thorlabs	FELH0650	Longpass	200 – 641 nm	6.1	660 – 2150 nm	0
Semrock	FF01-680/42-25	Bandpass	<660 nm & >701 nm	6	660 – 701 nm	6
Semrock	FF01-716/43-25	Bandpass	<680 nm & >748 nm	6	694 – 737 nm	0,01
Semrock	FF01-715/LP-25	Longpass	<715 nm	7	724 – 1200 nm	0
Chroma	ET775/50x	Bandpass	<740 nm & >810 nm	5.5	755 – 795 nm	Approx. 6
Thorlabs	FEL0550	Longpass	<537 nm	5.9	550 - 2000 nm	0,05
Thorlabs	FLH532-4	Bandpass	200 - 512 nm, 552 - 1200 nm	0.04	532-533 nm	6,10

Table C.: Optical Filters used for the measurements presented in this thesis.

A.4. Fiber Breakout Box

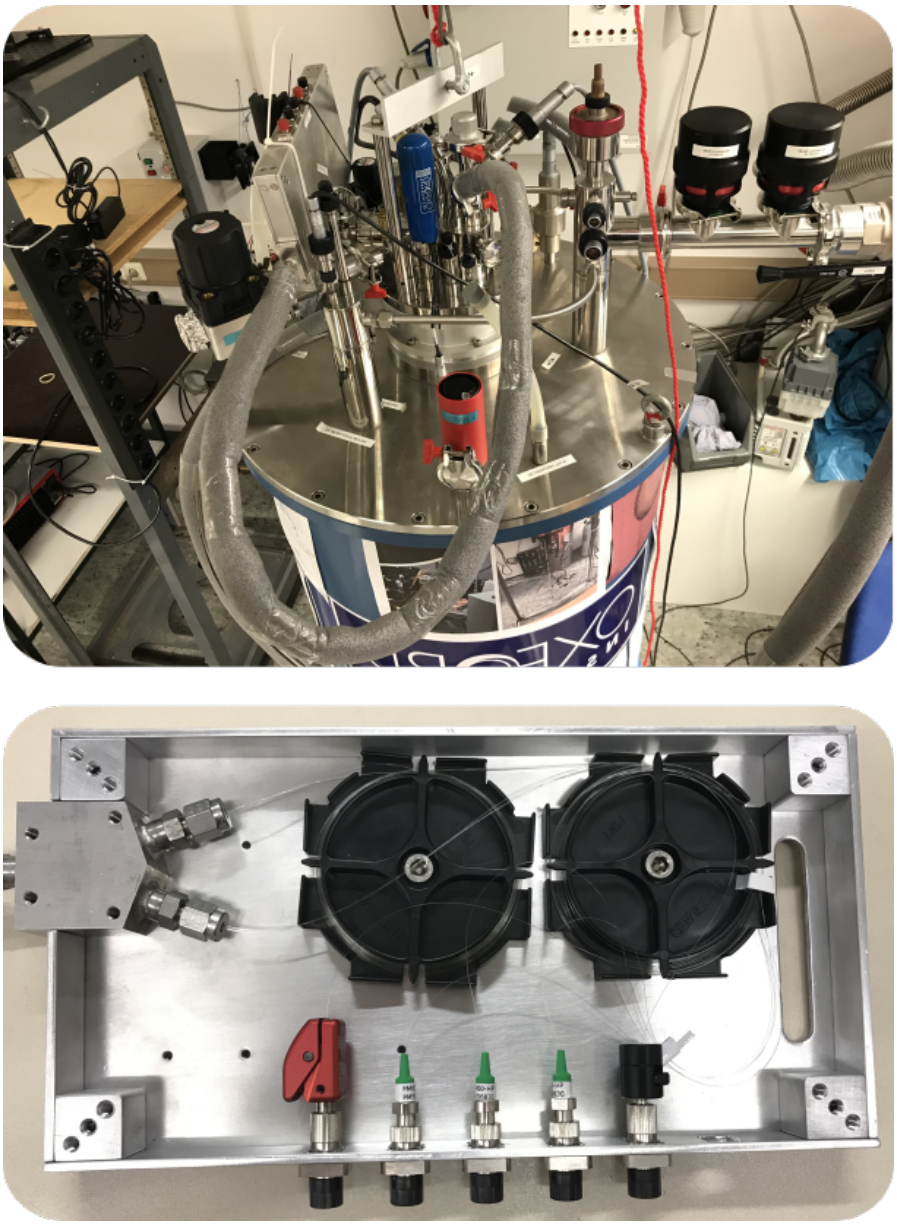

Figure A.6.: Photograph of the fiber breakout box at top of the cryostat. The fibers are guided through the isolated tube to an access port of the cryostat insert. The lower picture shows the inner part of the box. The fibers are glued into APC connectors, which allow access from standard fibers.

A.5. Dilution Refrigerator

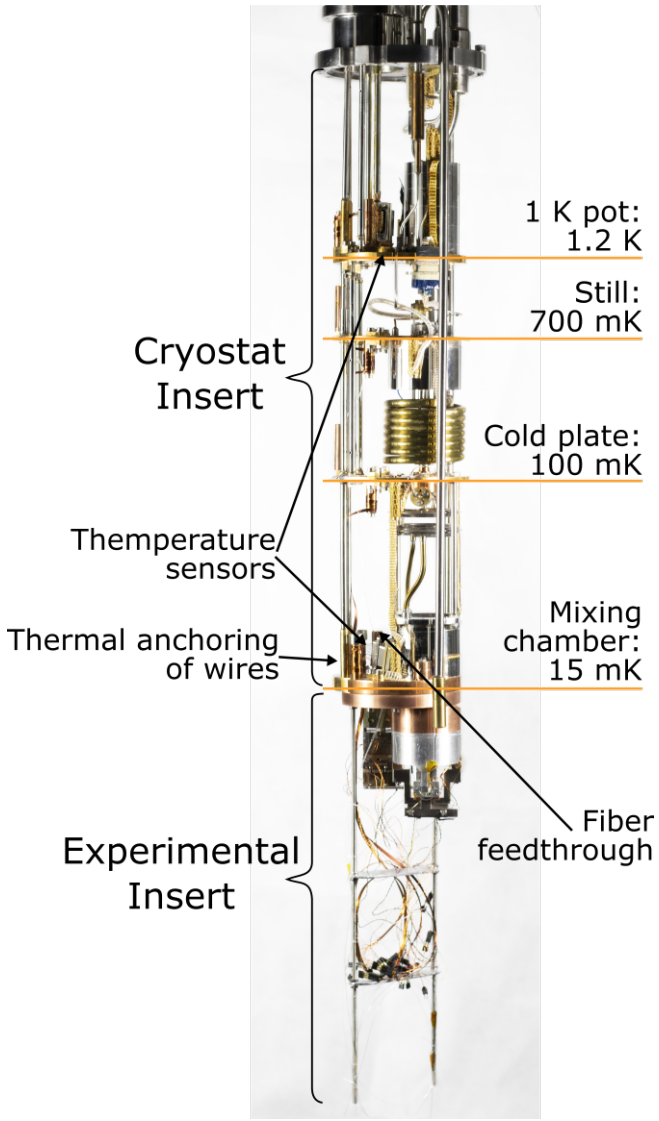

Figure A.7.: Photograph of the cryostat insert, with the experimental insert attached to the base of the He^3-He^4 mixing chamber. The nominal base temperature is 15 mK. In tests without an exp. insert, a lowest temperature of 23 mK has been demonstrated. Two temperature sensors are sitting at the highest level next to the 1 K pot and the absorption pump. The third sensor is positioned next to the mixing chamber.

A.6. Microcavity

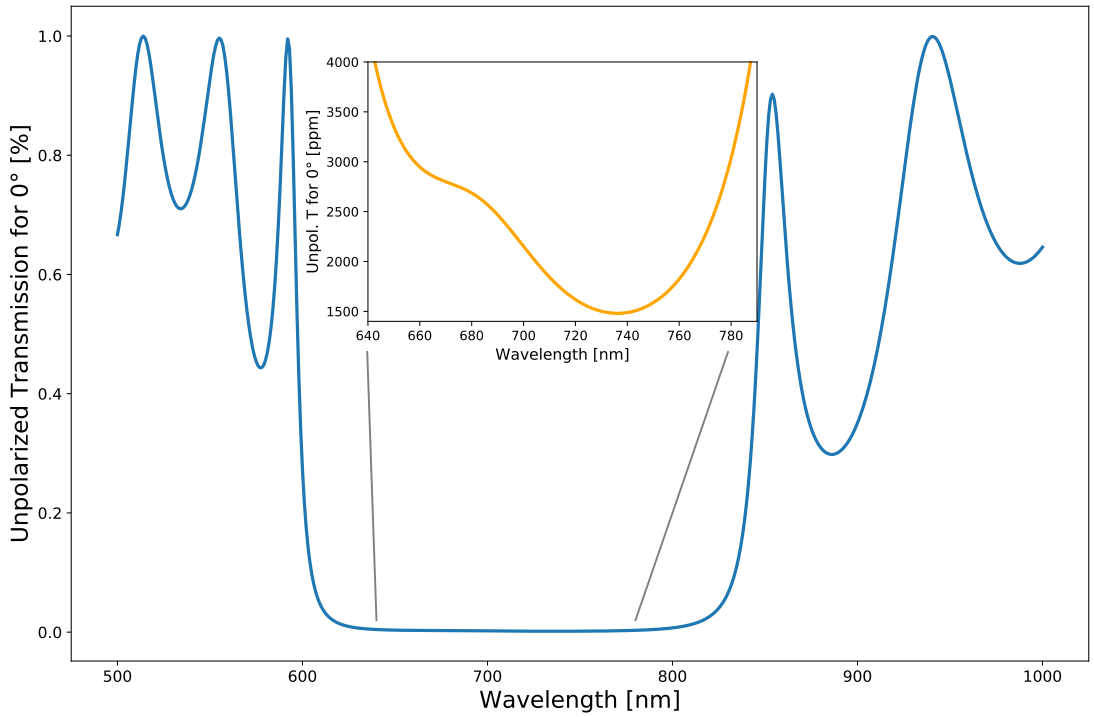

Figure A.8.: Transmission measurement of the DBR coating layer, produced and measured by Laseroptik Garbsen. The mirror substrate is fused silica and the stack is created by 18 layers of alternating titanium dioxide and silicon dioxide. Transmission in blue is measured for unpolarized light with an angle of incidence of zero degrees. The insert shows a part of the stopband in detail with a minimum transmission of 1480 ppm at 736 nm.

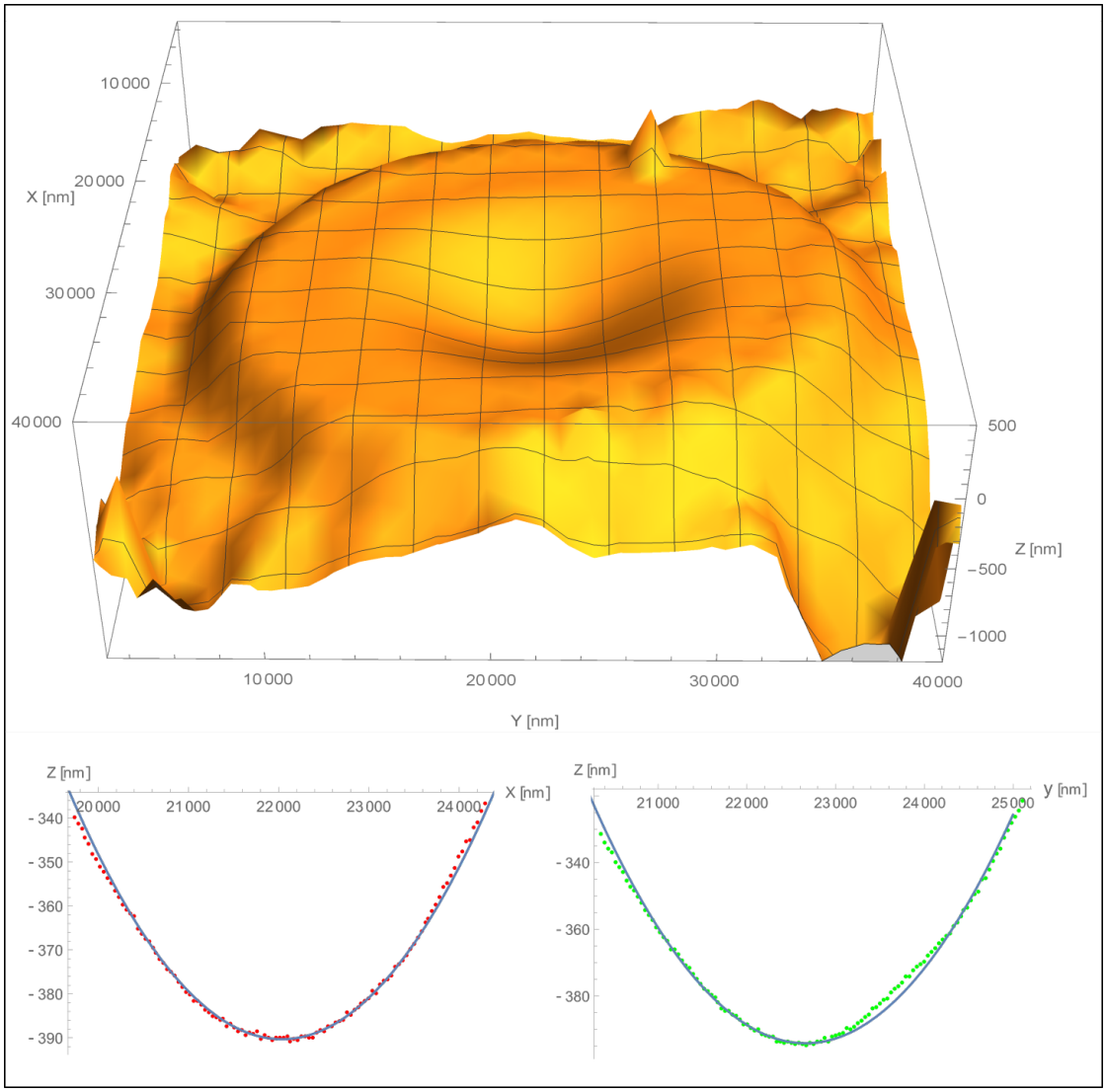

Figure A.9.: Center: Interferometric measurement of the fiber profile from the microcavity. Bottom: Cross section in x and y direction of the fiber tip (points). Fitting by a circular function (solid line) with different weights yields a radius of curvature of 49 µm in x direction (left) and 40 µm in y direction (right).

A.7. White light source

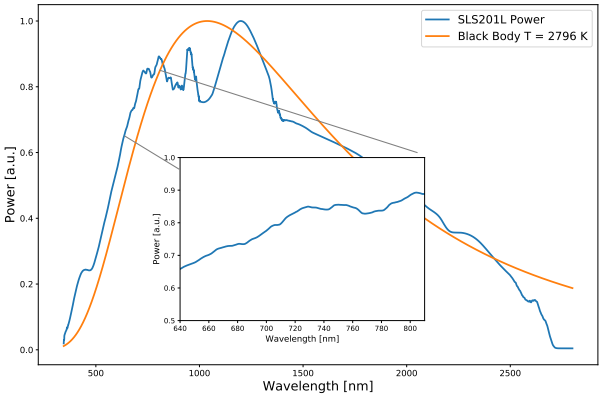

Figure A.10.: Spectral power distribution of the compact stabilized broadband light sources (Thorlabs SLS201L). A broad white light spectrum with a color temperature of 2796 K is emitted by a tungsten halogen light bulb, focus by a aspheric lens into a fiber, which can be coupled to the microcavity. The insert shows the emission over the microcavity stopband. The spectrum was measured by Thorlabs, futher details under `https://www.thorlabs.com/newgrouppage9.cfm?objectgroup_id=7269&pn=SLS201L/M`.

A.8. Spectrometer

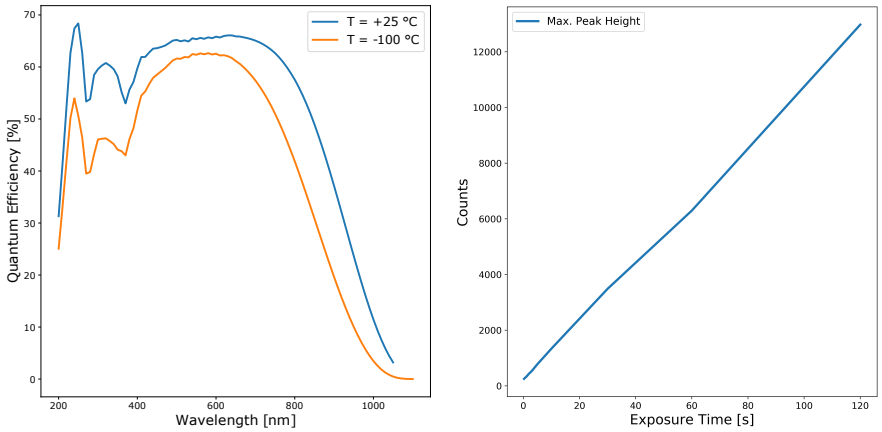

Figure A.11.: *Right:* Quantum efficiency of the Andor iDus 420A CCD camera from the spectrometer (Andor Shamrock 500i) used in this thesis. The camera is cooled to a temperature of -80 °C. The quantum efficiency is measured by the manufacturer. *Left:* Measured linearity of the spectrometer and CCD camera for different exposure times.

A.9. Fiber Background Emission

The microcavity is only accessible through several meters of fibers, which are installed from the outside (fiber breakout box A.4) to the experimental insert (see A.7). The SiV^- are (resonantly or off-resonantly) excited with lasers coupled into the fibers. Contamination and impurities in the fiber material (see 1.1) lead to background emission, especially when the off-resonant green light is used. These residual counts lead to a bad signal to noise ratio and can become a serious problem, when single SiV^- should be coupled to the microcavity. They may prevent even a measurement of the correlation function. The emission also depends on the temperature and can vary enormously between room temperature and LHe temperature.
For this reason, the background emission of four fibers is investigated under both conditions. Their properties are summed up in table D. A special apparatus (see fig. A.12), build for this test is used. Every fiber is cleaved and put into a bare fiber terminator to connect the fiber to collimation optics. The fibers are passing a press seal and go two times through a 9 mm stainless tube, such that their end is again passing the press seal at the top. The bending of the fiber do not change significantly their transmission.
Green excitation light is spectrally filtered before entering the fiber. The transmitted light is fiber coupled to the spectrometer. The fiber background emission is measured at room temperature and at 4 K. This is achieved by inserting the tube into the siphon entry of the cryostat. In that way, the fibers are directly immersed to LHe in the main bath. Form the filling level, it can be assumed, that $\approx$ 26 cm of the 5 m long fibers were in LHe. The compared emission spectra is shown in figure A.15 and A.16. Every spectrum is normalized to the transmitted power.
Figure A.14 compares the background emission of all fibers at room and at LHe temperature. Under both conditions, the pure silica core fibers (Al and MM) are emitting much less counts, which makes them attractive for the single SiV^- experiments.

Short	Name	Manufacture	Type	Wavelengths	Core material	Cladding Material	Coating
Al	SM530-125-160AL	Art Photonics	SM	cutoff at 530 nm	Pure silica	Fluorine-doped fused silica	Aluminum
Cu	Cu800-SMF	IVG Fiber	SM	800-1000 nm	Germanium-doped silica	Pure silica	Copper alloy, inner carbon layer
PM	PM630-HP	Thorlabs	PM	620-850 nm	Germanium-doped silica	Pure silica	dual acrylate
MM	FG050UGA	Thorlabs	MM	250-1200 nm	Pure silica	Fluorine-doped silica	acrylate

Table D.: Investigated fibers at room temperature and 4 K.

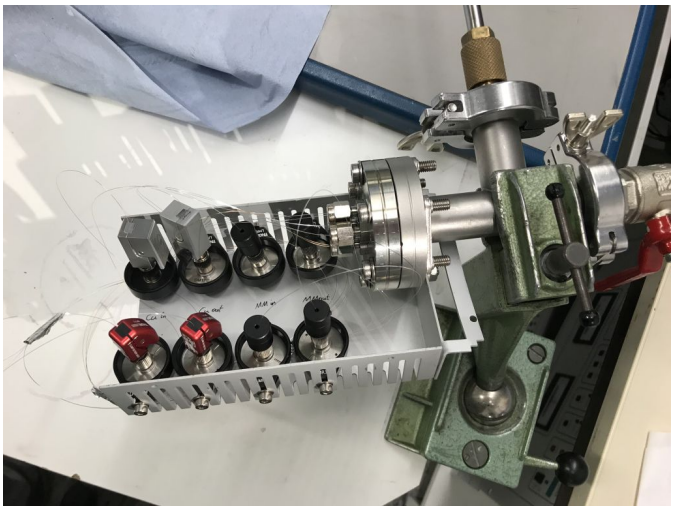

Figure A.12.: Fiber Background Test Device.

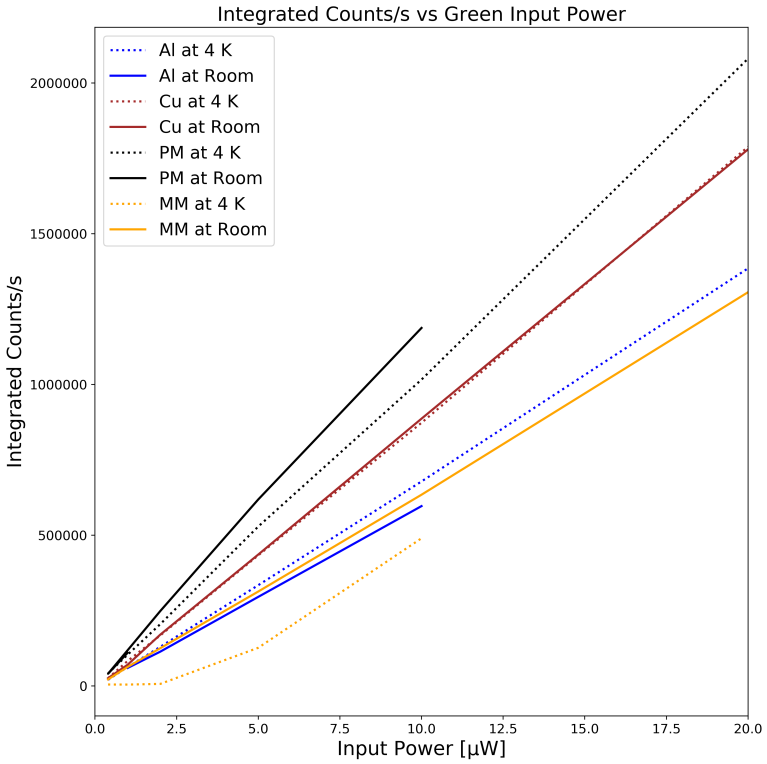

Figure A.13.: Fiber background emission as function of the input power at 532 nm.

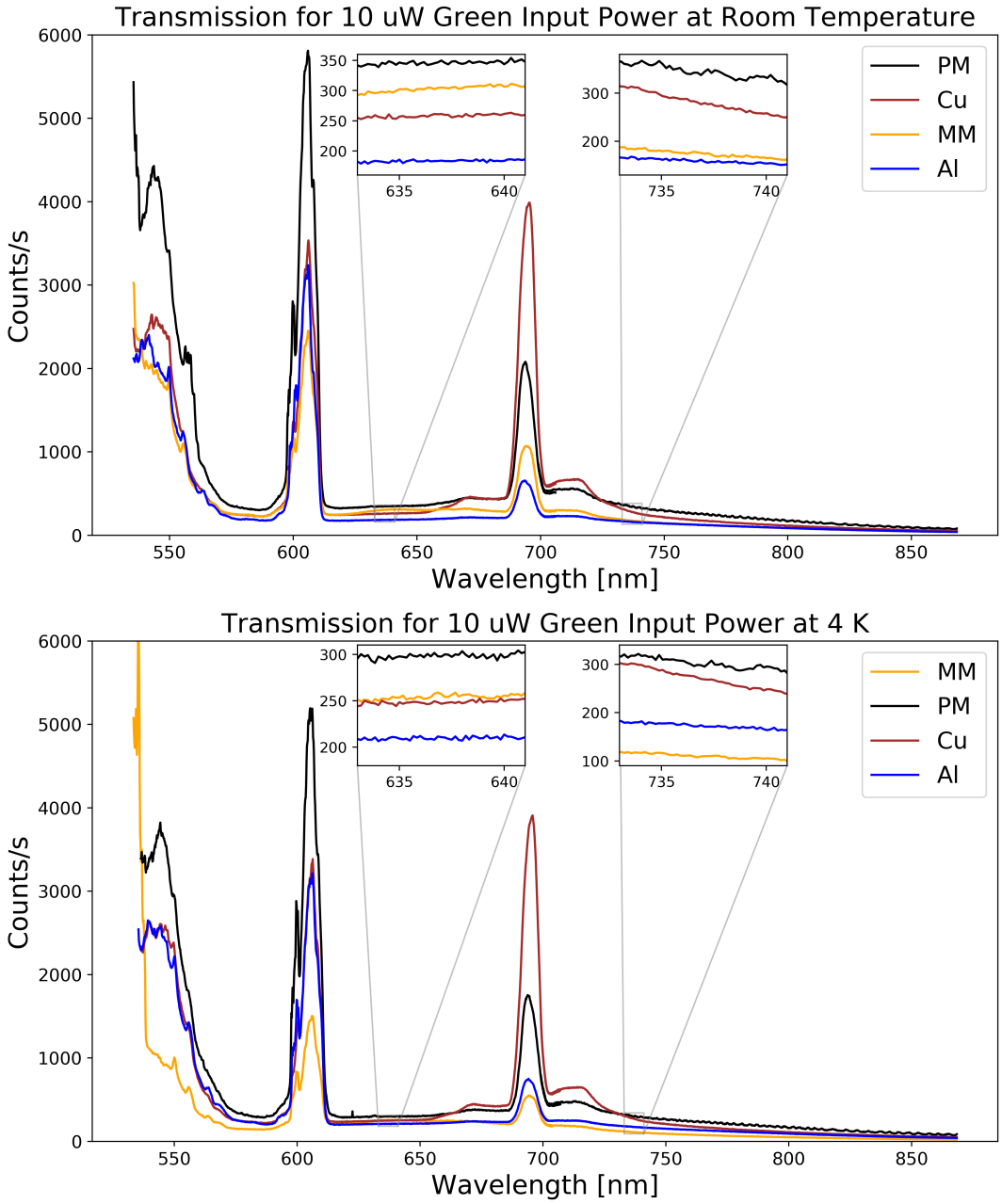

Figure A.14.: Fiber background emission comparing all four investigated fibers. The inset shows a detailed view along the region of the ZPL of the NV^- and the SiV^-. The pure silica core fibers (Al and MM) are featuring the lowest background emission.

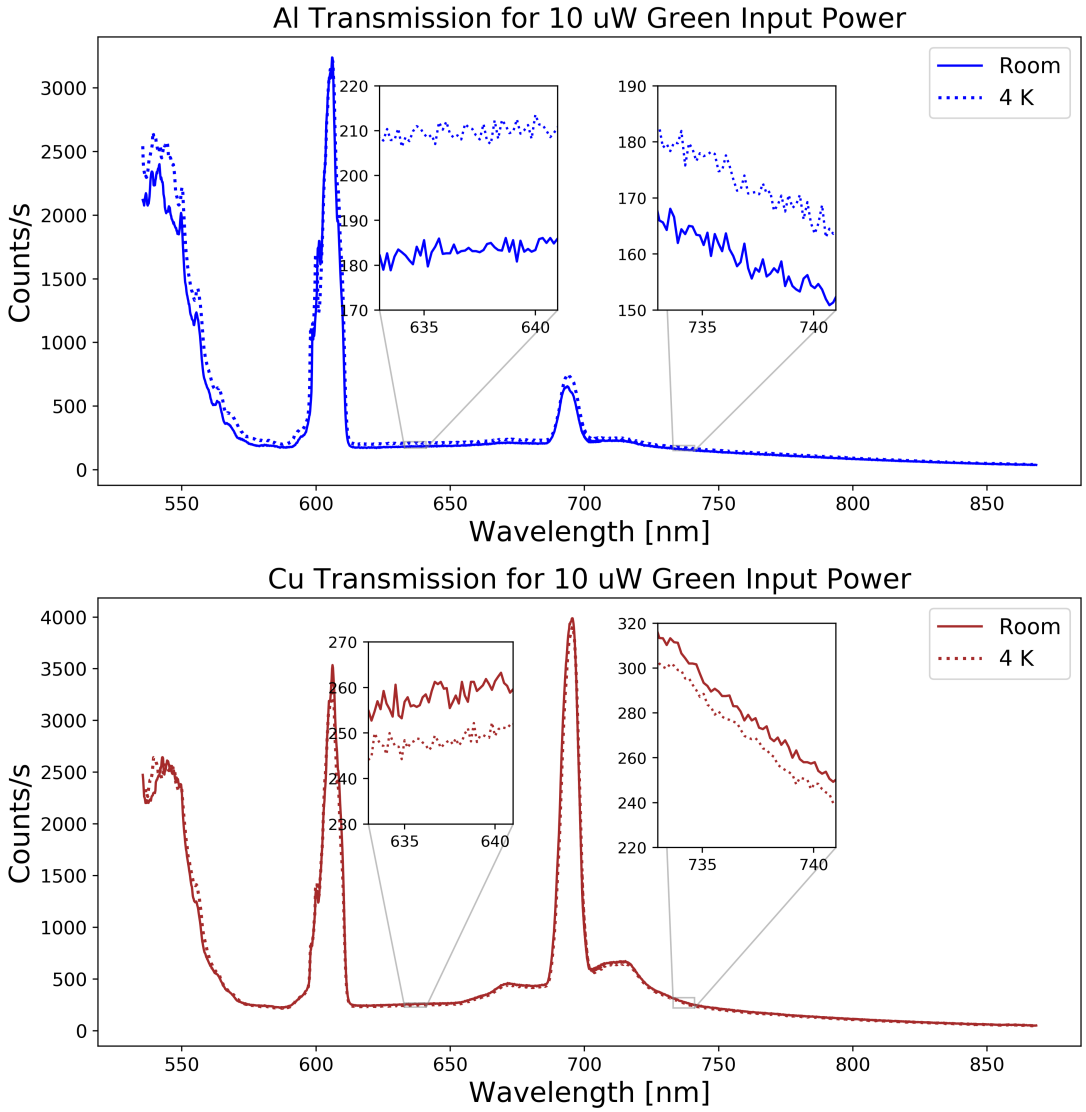

Figure A.15.: Particular fiber emission spectra for the Al and Cu fiber, comparing the emission at room temperature and at LHe temperature.

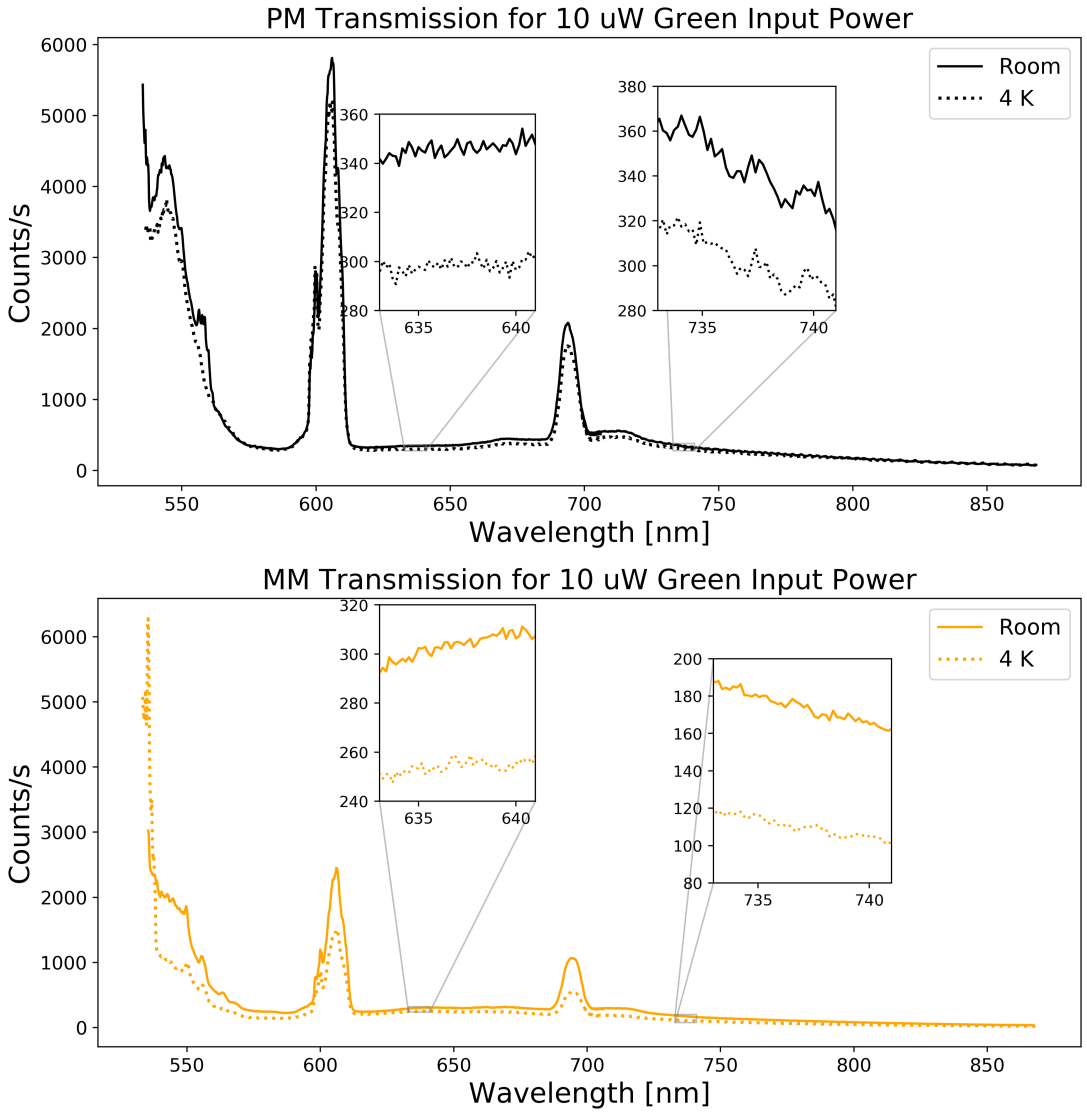

Figure A.16.: Particular fiber emission spectra for the PM and MM fiber, comparing the emission at room temperature and at LHe temperature.

A.10. Nanopositioner Voltage Calibration

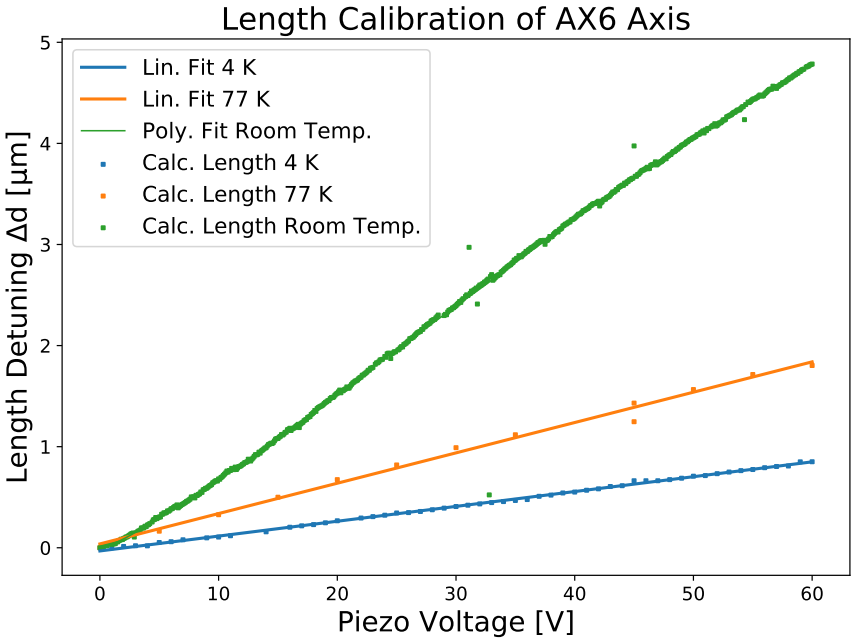

Figure A.17.: Length calibration of the nanopositioner axis used to scan the cavity length. The microcavity length is determined for various positions on the scan ramp (data points) at different temperatures. This data is used, to associate the scanned axis voltage with a microcavity lengths detuning. At room temperature, a non-linear behaviour is much more present, then at lower temperature with decreased expansion range. This effect was also measured by the manufactor [Lindenberg u. Bödefeld, 2013].

A.11. Qudi

Qudi[1] is a modular suite for experiment control and data processing, details can be found in Binder et al. [2017]. Qudi is written in Python under an open license. It provides a modular architecture for operating with several instruments by dividing the functionality into hardware, experiment logic and a user interface layer. The core consists of a user interface, live data visualization, distributed execution over networks, access from Jupyter notebooks for code input and data recording [Binder et al., 2017]. Originally, it was designed for experimental control of confocal microscopy, quantum optics and quantum information experiments. Features are for example XYZ piezo control for confocal fluorescence microscopy via National Instruments devices, access for ODRM measurement devices or a magnetic field alignment for NV^- via fluorescence.
Qudi also has a built-in readout of an APD connected via a National Instrument Card (SCB-68) to the experiment PC. For the measurement performed in this thesis, the program was extended by several self-written functions and accesses to new devices maintaining the initial idea of dividing into hardware, logic and gui. These extensions are:

- Remote access to a wavemeter webserver[2]. The DL is send to another laboratory, where the wavelength is measured by a HighFinesse WS6-200 wavemeter. The experiment PC in this laboratory runs a small webserver, providing the measured wavelengths, which is read out by Qudi
- Control/readout of the nanopositioners from AttoCube, by USB connection to the controller device (ANC350). The nanopositioners are initialized as a hardware device[3]. Qudi controls the axis offset or can be used to set a new position by single steps or in the continuous mode. The positions can be read out for example to distinguish different lateral positions on the diamond membrane.
- Control of the spectrometer Shamrock 500i from Andor and readout of the Andor iDus 420A CCD camera, connected by USB. The python library used was provided by the manufacturer. It is possible to select a grating, the wavelength range of the measurement and the exposure time.

[1] GitHub: `https://github.com/Ulm-IQO/qudi`, documentation: `https://ulm-iqo.github.io/qudi-generated-docs/html-docs/`
[2] available under: `https://github.com/stepansnigirev/py-ws7`
[3] python library: `https://github.com/Laukei/pyanc350`

- Access to a mixed signal oscilloscope Keysight MSOX4104A or MSO7104A by USB or TCP/IP[4]. Qudi can readout the acquired complete waveforms or specific values, measured by the built-in functions of the scope. The output of the scope (only MSOX4104A) can be used to apply arbitrary voltage signals, for example to synchronize with other measurement devices.

By these extensions, a self-written GUI shown in fig. A.18 can be used to automatically measure the finesse of the microcavity with the scope, by reading out an arbitrary amount of microcavity transmission signals and corresponding voltage ramps. The resonance peaks are fitted by the program with a Lorentzian function, to determine the center peaks and the FWHM for calculating the finesse. If the microcavity length is measured by the DL, the scope program can be used in a similar way. The calculated finesse/length values are saved with other experimental parameters like the wavelength or the position of the nanopositioners in a text file.
A spectrometer program can be used for automatic readout of a spectrum (see fig. A.19), which can also be fitted by a Lorentzian function to determine the microcavity lengths from a white light spectrum. This program can also controls the microcavity length by the nanopositioners axis with a voltage applied by the control device. In that way, the scans of the microcavity length can be recorded automatically. The program is saving the results in a .dat file and can be used to plot the received map of spectra (see fig. A.20).

[4]python library: `https://pyvisa.readthedocs.io/en/latest/`

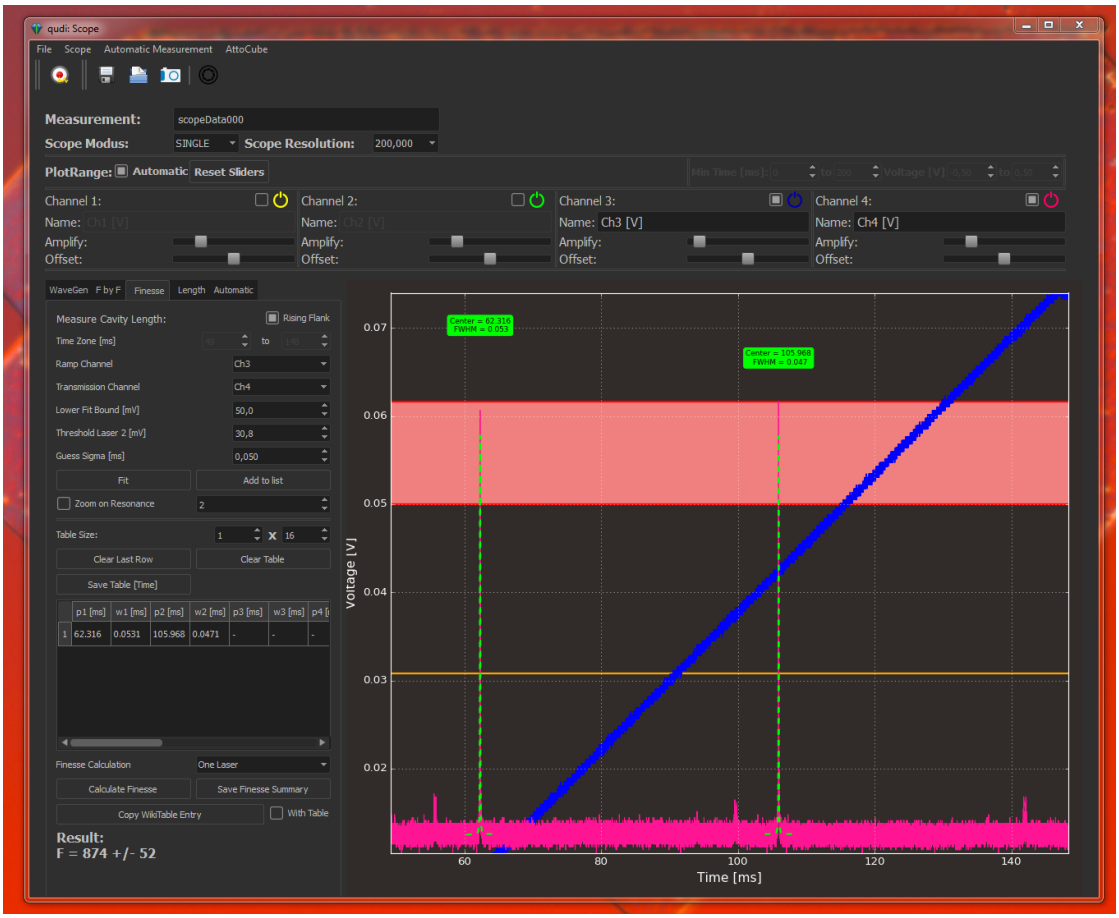

Figure A.18.: Qudi scope extension. All four analog channels of the scope can be readout by selecting a specific resolution. The waveforms can be plotted with a different offset and amplification. The scope is used to measure the PD signal from the microcavity transmission of a length scan. From the transmission peaks, the FWHM and the FSR can be directly extracted to determine the finesse. Statistics can be acquired for scanning over a longer range to cover several FSR. The Lorentzian fits are automatically done by the program, which needs a specific voltage height, to identify the fundamental mode.

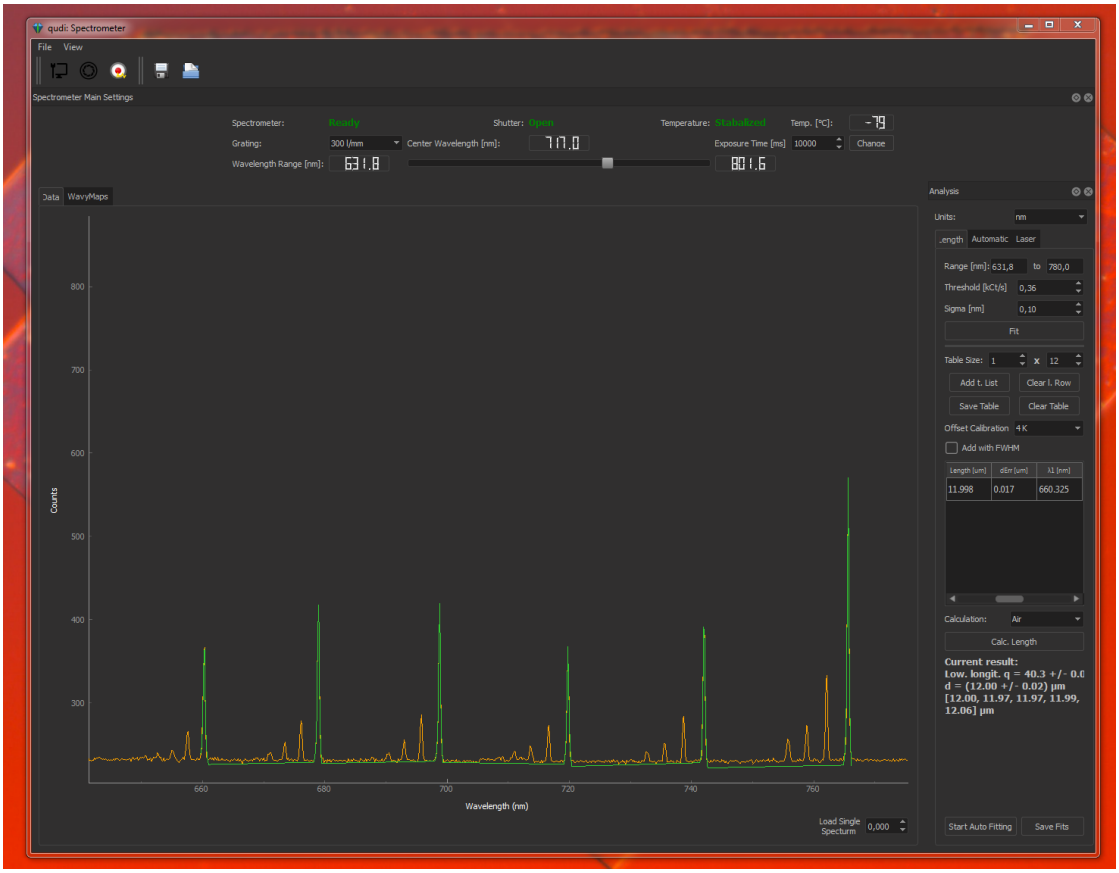

Figure A.19.: Qudi spectrometer extension. The grating spectrometer from Andor can be controlled by the upper panel to adjust the scanned wavelength range and exposure time. After a spectrum is recorded, it can be fit with an arbitrary amount of Lorentzian functions, where the wavelength range and height is selected. In that way, all fundamental modes TEM_{00q} can be fitted with one click. After adding them to the right table, the microcavity length can also be calculated automatically (up to now only for the bare mirror). The right panel can be used to control longer automatic measurements, which can be also directly fitted and saved to an output file. The spectrometer extension is connected to the nanopositioner control device. and LDTS can be recorded automatically.

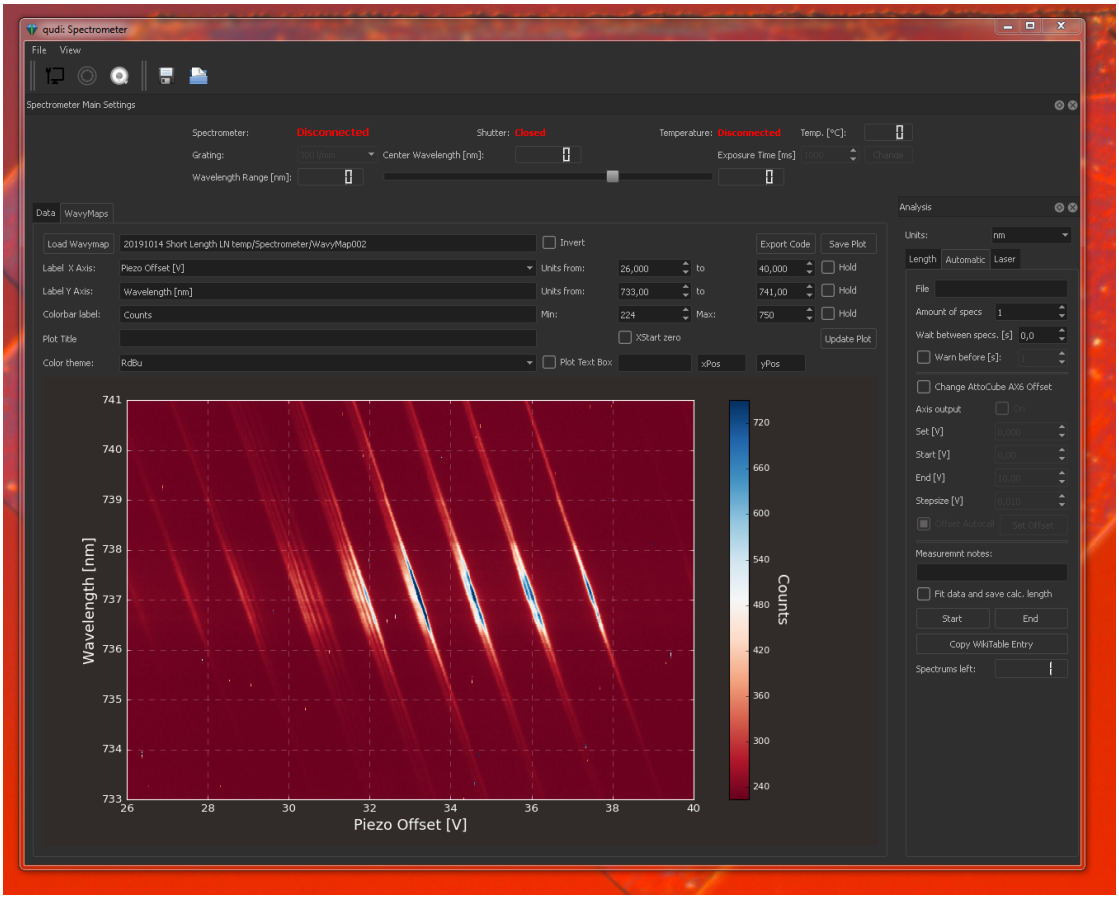

Figure A.20.: Qudi spectrometer extension for plotting LDTS. Some of the basic plot properties can be changed.

B

Bibliography

[Aharonovich et al. 2011a]
Aharonovich, I ; Castelletto, S ; Simpson, D A. ; Su, C-H ; Greentree, A D. ; Prawer, S: Diamond-based single-photon emitters. In: *Reports on Progress in Physics* 74 (2011), jun, Issue 7, pp. 076501. http://dx.doi.org/10.1088/0034-4885/74/7/076501. – DOI 10.1088/0034–4885/74/7/076501

[Aharonovich et al. 2011b]
Aharonovich, Igor ; Greentree, Andrew D. ; Prawer, Steven: Diamond photonics. In: *Nature Photonics* 5 (2011), jun, Issue 7, pp. 397–405. http://dx.doi.org/10.1038/nphoton.2011.54. – DOI 10.1038/nphoton.2011.54

[Albrecht 2014]
Albrecht, Roland C.: *Coupling of a Single Nitrogen-Vacancy Center in Diamond to a Fiber-based Microcavity*, Universität des Saarlandes, PhD Thesis, 2014

[Balasubramanian et al. 2009]
Balasubramanian, Gopalakrishnan ; Neumann, Philipp ; Twitchen, Daniel ; Markham, Matthew ; Kolesov, Roman ; Mizuochi, Norikazu ; Isoya, Junichi ; Achard, Jocelyn ; Beck, Johannes ; Tissler, Julia ; Jacques, Vincent ; Hemmer, Philip R. ; Jelezko, Fedor ; Wrachtrup, Jörg: Ultralong spin coherence time in isotopically engineered diamond. In: *Nature Materials* 8 (2009), apr, Issue 5, pp. 383–387. http://dx.doi.org/10.1038/nmat2420. – DOI 10.1038/nmat2420

[Balshaw 1996]
Balshaw, Nicholas H.: Practical Cryogenics: An Introduction to Laboratory Cryogenics / Oxford Instruments Group. Scientific Research Division. 1996 (0). – Technical Report. -

[Bar-Gill et al. 2013]
Bar-Gill, N. ; Pham, L.M. ; Jarmola, A. ; Budker, D. ; Walsworth, R.L.: Solid-state electronic spin coherence time approaching one second. In: *Nature Communications* 4 (2013), apr, Issue 1. http://dx.doi.org/10.1038/ncomms2771. – DOI 10.1038/ncomms2771

[Becker 2017]
Becker, Jonas N.: *Silicon Vacancy Colour Centres in Diamond Coherence Properties and Quantum Control*, Universität des Saarlandes, PhD Thesis, 2017

[Benedikter et al. 2015]
Benedikter, Julia ; Hümmer, Thomas ; Mader, Matthias ; Schlederer, Benedikt ; Reichel, Jakob ; Hänsch, Theodor W. ; Hunger, David: Transverse-mode coupling and diffraction loss in tunable Fabry-Pérot microcavities. In: *New Journal of Physics* 17 (2015), Issue 5, 053051. http://stacks.iop.org/1367-2630/17/i=5/a=053051

[Benedikter et al. 2017]
Benedikter, Julia ; Kaupp, Hanno ; Hümmer, Thomas ; Liang, Yuejiang ; Bommer, Alexander ; Becher, Christoph ; Krueger, Anke ; Smith, Jason M. ; Hänsch, Theodor W. ; Hunger, David: Cavity-Enhanced Single-Photon Source Based on the Silicon-Vacancy Center in Diamond. In: *Phys. Rev. Applied* 7 (2017), Feb, 024031. http://dx.doi.org/10.1103/PhysRevApplied.7.024031. – DOI 10.1103/PhysRevApplied.7.024031

[Bennett u. Brassard 1984]
Bennett, Charles H. ; Brassard, Gilles: Quantum cryptography: Public key distribution and coin tossing. In: *Proceedings of IEEE International Conference on Computers, Systems and Signal Processing* (1984), Issue 175

[Bennett et al. 1996]
Bennett, Charles H. ; Brassard, Gilles ; Popescu, Sandu ; Schumacher, Benjamin ; Smolin, John A. ; Wootters, William K.: Purification of Noisy Entanglement and Faithful Teleportation via Noisy Channels. In: *Physical Review Letters* 76 (1996), jan, Issue 5, pp. 722–725. http://dx.doi.org/10.1103/physrevlett.76.722. – DOI 10.1103/physrevlett.76.722

[Binder et al. 2017]
Binder, Jan M. ; Stark, Alexander ; Tomek, Nikolas ; Scheuer, Jochen ; Frank,

Florian ; Jahnke, Kay D. ; Müller, Christoph ; Schmitt, Simon ; Metsch, Mathias H. ; Unden, Thomas ; Gehring, Tobias ; Huck, Alexander ; Andersen, Ulrik L. ; Rogers, Lachlan J. ; Jelezko, Fedor: Qudi: A modular python suite for experiment control and data processing. In: *SoftwareX* 6 (2017), pp. 85–90. http://dx.doi.org/10.1016/j.softx.2017.02.001. – DOI 10.1016/j.softx.2017.02.001

[Bogdanović et al. 2017]
Bogdanović, Stefan ; Dam, Suzanne B. ; Bonato, Cristian ; Coenen, Lisanne C. ; Zwerver, Anne-Marije J. ; Hensen, Bas ; Liddy, Madelaine S. Z. ; Fink, Thomas ; Reiserer, Andreas ; Lončar, Marko ; Hanson, Ronald: Design and low-temperature characterization of a tunable microcavity for diamond-based quantum networks. In: *Applied Physics Letters* 110 (2017), apr, Issue 17, pp. 171103. http://dx.doi.org/10.1063/1.4982168. – DOI 10.1063/1.4982168

[Bolshedvorskii et al. 2019]
Bolshedvorskii, Stepan V. ; Zeleneev, Anton I. ; Vorobyov, Vadim V. ; Soshenko, Vladimir V. ; Rubinas, Olga R. ; Zhulikov, Leonid A. ; Pivovarov, Pavel A. ; Sorokin, Vadim N. ; Smolyaninov, Andrey N. ; Kulikova, Liudmila F. ; Garanina, Anastasiia S. ; Lyapin, Sergey G. ; Agafonov, Viatcheslav N. ; Uzbekov, Rustem E. ; Davydov, Valery A. ; Akimov, Alexey V.: Single Silicon Vacancy Centers in 10 nm Diamonds for Quantum Information Applications. In: *ACS Applied Nano Materials* (2019), jul. http://dx.doi.org/10.1021/acsanm.9b00580. – DOI 10.1021/acsanm.9b00580

[Brachmann et al. 2016]
Brachmann, Johannes F. S. ; Kaupp, Hanno ; Hänsch, Theodor W. ; Hunger, David: Photothermal effects in ultra-precisely stabilized tunable microcavities. In: *Optics Express* 24 (2016), sep, Issue 18, pp. 21205. http://dx.doi.org/10.1364/oe.24.021205. – DOI 10.1364/oe.24.021205

[Briegel et al. 1998]
Briegel, H.-J. ; Dür, W. ; Cirac, J. I. ; Zoller, P.: Quantum Repeaters: The Role of Imperfect Local Operations in Quantum Communication. In: *Phys. Rev. Lett.* 81 (1998), Dec, 5932–5935. http://dx.doi.org/10.1103/PhysRevLett.81.5932. – DOI 10.1103/PhysRevLett.81.5932

[Castelvecchi 2018]
Castelvecchi, Davide: The quantum internet has arrived (and it hasn't). In:

Nature 554 (2018), feb, Issue 7692, pp. 289–292. http://dx.doi.org/10.1038/d41586-018-01835-3. – DOI 10.1038/d41586–018–01835–3

[Clark et al. 1995]
Clark, C. D. ; Kanda, H. ; Kiflawi, I. ; Sittas, G.: Silicon defects in diamond. In: *Physical Review B* 51 (1995), jun, Issue 23, pp. 16681–16688. http://dx.doi.org/10.1103/physrevb.51.16681. – DOI 10.1103/physrevb.51.16681

[Clesca 2017]
Clesca, Bertrand: *How Low Can Fiber Loss Go?* Online Webpage. http://opticalcloudinfra.com/index.php/2017/04/17/low-can-fiber-loss-go/. Version: 2017. – April

[Coffey 2014]
Coffey, Valerie: Sea Change: The Challenges Facing Submarine Optical Communications. In: *Optics and Photonics News* 25 (2014), mar, Issue 3, pp. 26. http://dx.doi.org/10.1364/opn.25.3.000026. – DOI 10.1364/opn.25.3.000026

[van Dam et al. 2018]
Dam, Suzanne B. ; Ruf, Maximilian ; Hanson, Ronald: Optimal design of diamond-air microcavities for quantum networks using an analytical approach. In: *New Journal of Physics* 20 (2018), nov, Issue 11, pp. 115004. http://dx.doi.org/10.1088/1367-2630/aaec29. – DOI 10.1088/1367–2630/aaec29

[Demtröder 2000]
Demtröder, Wolfgang: *Laserspektroskopie*. Springer Berlin Heidelberg, 2000 DOI 10.1007/978–3–662–08266–9. http://dx.doi.org/10.1007/978-3-662-08266-9

[Demtröder 2011]
Demtröder, Wolfgang: *Laserspektroskopie 1*. Springer Berlin Heidelberg, 2011 DOI 10.1007/978–3–642–21306–9. http://dx.doi.org/10.1007/978-3-642-21306-9

[Demtröder 2013]
Demtröder, Wolfgang: *Experimentalphysik 2*. Springer Berlin Heidelberg, 2013 DOI 10.1007/978–3–642–29944–5. http://dx.doi.org/10.1007/978-3-642-29944-5

[D'Haenens-Johansson et al. 2011]
D'Haenens-Johansson, U. F. S. ; Edmonds, A. M. ; Green, B. L. ; Newton, M. E. ; Davies, G. ; Martineau, P. M. ; Khan, R. U. A. ; Twitchen, D. J.: Optical properties of the neutral silicon split-vacancy center in diamond. In: *Physical Review*

B 84 (2011), dec, Issue 24. http://dx.doi.org/10.1103/physrevb.84.245208. – DOI 10.1103/physrevb.84.245208

[Dietrich et al. 2014]
Dietrich, Andreas ; Jahnke, Kay D. ; Binder, Jan M. ; Teraji, Tokuyuki ; Isoya, Junichi ; Rogers, Lachlan J. ; Jelezko, Fedor: Isotopically varying spectral features of silicon-vacancy in diamond. In: *New Journal of Physics* 16 (2014), nov, Issue 11, pp. 113019. http://dx.doi.org/10.1088/1367-2630/16/11/113019. – DOI 10.1088/1367–2630/16/11/113019

[Dréau et al. 2018]
Dréau, Anaïs ; Tcheborateva, Anna ; Mahdaoui, Aboubakr E. ; Bonato, Cristian ; Hanson, Ronald: Quantum Frequency Conversion of Single Photons from a Nitrogen-Vacancy Center in Diamond to Telecommunication Wavelengths. In: *Physical Review Applied* 9 (2018), jun, Issue 6. http://dx.doi.org/10.1103/physrevapplied.9.064031. – DOI 10.1103/physrevapplied.9.064031

[Drever et al. 1983]
Drever, R.W.P. ; Hall, J.L. ; Kowalski, F.V. ; Hough, J. ; Ford, G.M. ; Munley, A.J. ; Ward, H.: Laser phase and frequency stabilization using an optical resonator. In: *Applied Physics B* 31 (1983), Issue 2, 97-105. http://dx.doi.org/10.1007/BF00702605. – DOI 10.1007/BF00702605. – ISSN 0946–2171

[Ekert 1991]
Ekert, Artur K.: Quantum cryptography based on Bell's theorem. In: *Phys. Rev. Lett.* 67 (1991), Aug, 661–663. http://dx.doi.org/10.1103/PhysRevLett.67.661. – DOI 10.1103/PhysRevLett.67.661

[Fox 2006]
Fox, Mark: *Quantum Optics*. Oxford University Press https://www.ebook.de/de/product/5214114/mark_fox_quantum_optics.html. – ISBN 0198566735

[Fu 2019]
Fu, Kai-Mei: Viewpoint: Making Diamond Qubits Talk to Light. In: *American Physical Society (APS Physics)* (2019). https://physics.aps.org/articles/v12/117

[Gottesman et al. 2012]
Gottesman, Daniel ; Jennewein, Thomas ; Croke, Sarah: Longer-Baseline Telescopes Using Quantum Repeaters. In: *Physical Review Letters* 109 (2012), aug, Issue 7. http://dx.doi.org/10.1103/physrevlett.109.070503. – DOI 10.1103/physrevlett.109.070503

[Haroche u. Raimond 2006]
Haroche, Serge ; Raimond, Jean-Michel: *Exploring the Quantum*. Oxford University Press, 2006 DOI 10.1093/acprof:oso/9780198509141.001.0001. http://dx.doi.org/10.1093/acprof:oso/9780198509141.001.0001

[Häußler et al. 2018]
Häussler, Stefan ; Benedikter, Julia ; Bray, Kerem ; Regan, Blake ; Dietrich, Andreas ; Twamley, Jason ; Aharonovich, Igor ; Hunger, David ; Kubanek, Alexander: A Diamond-Photonics Platform Based on Silicon-Vacancy Centers in a Single Crystal Diamond Membrane and a Fiber-Cavity. (2018), December

[Humphreys et al. 2018]
Humphreys, Peter C. ; Kalb, Norbert ; Morits, Jaco P. J. ; Schouten, Raymond N. ; Vermeulen, Raymond F. L. ; Twitchen, Daniel J. ; Markham, Matthew ; Hanson, Ronald: Deterministic delivery of remote entanglement on a quantum network. In: *Nature* 558 (2018), jun, Issue 7709, pp. 268–273. http://dx.doi.org/10.1038/s41586-018-0200-5. – DOI 10.1038/s41586–018–0200–5

[Hunger et al. 2012]
Hunger, D. ; Deutsch, C. ; Barbour, R. J. ; Warburton, R. J. ; Reichel, J.: Laser micro-fabrication of concave, low-roughness features in silica. In: *AIP Advances* 2 (2012), mar, Issue 1, pp. 012119. http://dx.doi.org/10.1063/1.3679721. – DOI 10.1063/1.3679721

[Hunger et al. 2010]
Hunger, D ; Steinmetz, T ; Colombe, Y ; Deutsch, C ; Hänsch, T W. ; Reichel, J: A fiber Fabry-Perot cavity with high finesse. In: *New Journal of Physics* 12 (2010), Issue 6, 065038. http://stacks.iop.org/1367-2630/12/i=6/a=065038

[Iwasaki et al. 2015]
Iwasaki, Takayuki ; Ishibashi, Fumitaka ; Miyamoto, Yoshiyuki ; Doi, Yuki ; Kobayashi, Satoshi ; Miyazaki, Takehide ; Tahara, Kosuke ; Jahnke, Kay D. ; Rogers, Lachlan J. ; Naydenov, Boris ; Jelezko, Fedor ; Yamasaki, Satoshi ;

Nagamachi, Shinji ; Inubushi, Toshiro ; Mizuochi, Norikazu ; Hatano, Mutsuko: Germanium-Vacancy Single Color Centers in Diamond. In: *Scientific Reports* 5 (2015), aug, Issue 1. http://dx.doi.org/10.1038/srep12882. – DOI 10.1038/srep12882

[Iwasaki et al. 2017]
Iwasaki, Takayuki ; Miyamoto, Yoshiyuki ; Taniguchi, Takashi ; Siyushev, Petr ; Metsch, Mathias H. ; Jelezko, Fedor ; Hatano, Mutsuko: Tin-Vacancy Quantum Emitters in Diamond. In: *Physical Review Letters* 119 (2017), dec, Issue 25. http://dx.doi.org/10.1103/physrevlett.119.253601. – DOI 10.1103/physrevlett.119.253601

[Jahnke et al. 2015]
Jahnke, Kay D. ; Sipahigil, Alp ; Binder, Jan M. ; Doherty, Marcus W. ; Metsch, Mathias ; Rogers, Lachlan J. ; Manson, Neil B. ; Lukin, Mikhail D. ; Jelezko, Fedor: Electron–phonon processes of the silicon-vacancy centre in diamond. In: *New Journal of Physics* 17 (2015), apr, Issue 4, pp. 043011. http://dx.doi.org/10.1088/1367-2630/17/4/043011. – DOI 10.1088/1367–2630/17/4/043011

[Jahnke 2015]
Jahnke, Kay D.: *The silicon-vacancy centre in diamond*, Universität Ulm, PhD Thesis, 2015

[Jamali et al. 2014]
Jamali, Mohammad ; Gerhardt, Ilja ; Rezai, Mohammad ; Frenner, Karsten ; Fedder, Helmut ; Wrachtrup, Jörg: Microscopic diamond solid-immersion-lenses fabricated around single defect centers by focused ion beam milling. In: *Review of Scientific Instruments* 85 (2014), dec, Issue 12, pp. 123703. http://dx.doi.org/10.1063/1.4902818. – DOI 10.1063/1.4902818

[Janitz et al. 2015]
Janitz, Erika ; Ruf, Maximilian ; Dimock, Mark ; Bourassa, Alexandre ; Sankey, Jack ; Childress, Lilian: Fabry-Perot microcavity for diamond-based photonics. In: *Physical Review A* 92 (2015), oct, Issue 4. http://dx.doi.org/10.1103/physreva.92.043844. – DOI 10.1103/physreva.92.043844

[Janitz et al. 2017]
Janitz, Erika ; Ruf, Maximilian ; Fontana, Yannik ; Sankey, Jack ; Childress, Lilian: High mechanical bandwidth fiber-coupled Fabry-Perot cavity. In: *Optics*

Express 25 (2017), aug, Issue 17, pp. 20932. http://dx.doi.org/10.1364/oe.25.020932. – DOI 10.1364/oe.25.020932

[Kaupp et al. 2016]
Kaupp, Hanno ; Hümmer, Thomas ; Mader, Matthias ; Schlederer, Benedikt ; Benedikter, Julia ; Haeusser, Philip ; Chang, Huan-Cheng ; Fedder, Helmut ; Hänsch, Theodor W. ; Hunger, David: Purcell-Enhanced Single-Photon Emission from Nitrogen-Vacancy Centers Coupled to a Tunable Microcavity. In: *Physical Review Applied* 6 (2016), nov, Issue 5. http://dx.doi.org/10.1103/physrevapplied.6.054010. – DOI 10.1103/physrevapplied.6.054010

[Kimble 2008]
Kimble, H. J.: The quantum internet. In: *Nature* 453 (2008), June, Issue 7198, 1023–1030. http://dx.doi.org/10.1038/nature07127. – ISSN 0028–0836

[Kogelnik u. Li 1966]
Kogelnik, H. ; Li, T.: Laser Beams and Resonators. In: *Appl. Opt.* 5 (1966), Oct, Issue 10, 1550–1567. http://dx.doi.org/10.1364/AO.5.001550. – DOI 10.1364/AO.5.001550

[Kómár et al. 2014]
Kómár, P. ; Kessler, E. M. ; Bishof, M. ; Jiang, L. ; Sørensen, A. S. ; Ye, J. ; Lukin, M. D.: A quantum network of clocks. In: *Nature Physics* 10 (2014), jun, Issue 8, pp. 582–587. http://dx.doi.org/10.1038/nphys3000. – DOI 10.1038/nphys3000

[Lühmann et al. 2018]
Lühmann, Tobias ; Raatz, Nicole ; John, Roger ; Lesik, Margarita ; Rödiger, Jasper ; Portail, Marc ; Wildanger, Dominik ; Kleissler, Felix ; Nordlund, Kai ; Zaitsev, Alexander ; Roch, Jean-François ; Tallaire, Alexandre ; Meijer, Jan ; Pezzagna, Sébastien: Screening and engineering of colour centres in diamond. In: *Journal of Physics D: Applied Physics* 51 (2018), oct, Issue 48, pp. 483002. http://dx.doi.org/10.1088/1361-6463/aadfab. – DOI 10.1088/1361–6463/aadfab

[Liao et al. 2018]
Liao, Sheng-Kai ; Cai, Wen-Qi ; Handsteiner, Johannes ; Liu, Bo ; Yin, Juan ; Zhang, Liang ; Rauch, Dominik ; Fink, Matthias ; Ren, Ji-Gang ; Liu, Wei-Yue ; Li, Yang ; Shen, Qi ; Cao, Yuan ; Li, Feng-Zhi ; Wang, Jian-Feng ; Huang, Yong-Mei ; Deng, Lei ; Xi, Tao ; Ma, Lu ; Hu, Tai ; Li, Li ; Liu, Nai-Le ; Koidl, Franz ; Wang, Peiyuan ; Chen, Yu-Ao ; Wang, Xiang-Bin ; Steindorfer, Michael ; Kirchner,

Georg ; Lu, Chao-Yang ; Shu, Rong ; Ursin, Rupert ; Scheidl, Thomas ; Peng, Cheng-Zhi ; Wang, Jian-Yu ; Zeilinger, Anton ; Pan, Jian-Wei: Satellite-Relayed Intercontinental Quantum Network. In: *Physical Review Letters* 120 (2018), jan, Issue 3. http://dx.doi.org/10.1103/physrevlett.120.030501. – DOI 10.1103/physrevlett.120.030501

[Liao et al. 2017]
Liao, Sheng-Kai ; Cai, Wen-Qi ; Liu, Wei-Yue ; Zhang, Liang ; Li, Yang ; Ren, Ji-Gang ; Yin, Juan ; Shen, Qi ; Cao, Yuan ; Li, Zheng-Ping ; Li, Feng-Zhi ; Chen, Xia-Wei ; Sun, Li-Hua ; Jia, Jian-Jun ; Wu, Jin-Cai ; Jiang, Xiao-Jun ; Wang, Jian-Feng ; Huang, Yong-Mei ; Wang, Qiang ; Zhou, Yi-Lin ; Deng, Lei ; Xi, Tao ; Ma, Lu ; Hu, Tai ; Zhang, Qiang ; Chen, Yu-Ao ; Liu, Nai-Le ; Wang, Xiang-Bin ; Zhu, Zhen-Cai ; Lu, Chao-Yang ; Shu, Rong ; Peng, Cheng-Zhi ; Wang, Jian-Yu ; Pan, Jian-Wei: Satellite-to-ground quantum key distribution. In: *Nature* 549 (2017), aug, Issue 7670, pp. 43–47. http://dx.doi.org/10.1038/nature23655. – DOI 10.1038/nature23655

[Lindenberg u. Bödefeld 2013]
Lindenberg, Tobias ; Bödefeld, Christoph: Technical Note: Power dissipation of a piezo / attocube systems AG. 2013 (1). – Technical Report. -

[Lindner et al. 2018]
Lindner, Sarah ; Bommer, Alexander ; Muzha, Andreas ; Krueger, Anke ; Gines, Laia ; Mandal, Soumen ; Williams, Oliver ; Londero, Elisa ; Gali, Adam ; Becher, Christoph: Strongly inhomogeneous distribution of spectral properties of silicon-vacancy color centers in nanodiamonds. In: *New Journal of Physics* 20 (2018), nov, Issue 11, pp. 115002. http://dx.doi.org/10.1088/1367-2630/aae93f. – DOI 10.1088/1367–2630/aae93f

[Luong et al. 2016]
Luong, D. ; Jiang, L. ; Kim, J. ; Lütkenhaus, N.: Overcoming lossy channel bounds using a single quantum repeater node. In: *Applied Physics B* 122 (2016), apr, Issue 4. http://dx.doi.org/10.1007/s00340-016-6373-4. – DOI 10.1007/s00340–016–6373–4

[Machielse et al. 2019]
Machielse, B. ; Bogdanovic, S. ; Meesala, S. ; Gauthier, S. ; Burek, M. J. ; Joe, G. ; Chalupnik, M. ; Sohn, Y. I. ; Holzgrafe, J. ; Evans, R. E. ; Chia,

C. ; Atikian, H. ; Bhaskar, M. K. ; Sukachev, D. D. ; Shao, L. ; Maity, S. ; Lukin, M. D. ; Lončar, M.: Quantum Interference of Electromechanically Stabilized Emitters in Nanophotonic Devices. In: *Physical Review X* 9 (2019), aug, Issue 3. http://dx.doi.org/10.1103/physrevx.9.031022. – DOI 10.1103/physrevx.9.031022

[Meesala et al. 2018]
Meesala, Srujan ; Sohn, Young-Ik ; Pingault, Benjamin ; Shao, Linbo ; Atikian, Haig A. ; Holzgrafe, Jeffrey ; Gündoğan, Mustafa ; Stavrakas, Camille ; Sipahigil, Alp ; Chia, Cleaven ; Evans, Ruffin ; Burek, Michael J. ; Zhang, Mian ; Wu, Lue ; Pacheco, Jose L. ; Abraham, John ; Bielejec, Edward ; Lukin, Mikhail D. ; Atatüre, Mete ; Lončar, Marko: Strain engineering of the silicon-vacancy center in diamond. In: *Physical Review B* 97 (2018), may, Issue 20. http://dx.doi.org/10.1103/physrevb.97.205444. – DOI 10.1103/physrevb.97.205444

[Meschede 2008]
Meschede, Dieter: *Optik, Licht und Laser*. Vieweg+Teubner, 2008 DOI 10.1007/978–3–8348–9288–1. http://dx.doi.org/10.1007/978-3-8348-9288-1. – ISBN 978–3–8348–9288–1

[Metsch et al. 2019]
Metsch, Mathias H. ; Senkalla, Katharina ; Tratzmiller, Benedikt ; Scheuer, Jochen ; Kern, Michael ; Achard, Jocelyn ; Tallaire, Alexandre ; Plenio, Martin B. ; Siyushev, Petr ; Jelezko, Fedor: Initialization and Readout of Nuclear Spins via a Negatively Charged Silicon-Vacancy Center in Diamond. In: *Physical Review Letters* 122 (2019), may, Issue 19. http://dx.doi.org/10.1103/physrevlett.122.190503. – DOI 10.1103/physrevlett.122.190503

[Monroe et al. 2014]
Monroe, C. ; Raussendorf, R. ; Ruthven, A. ; Brown, K. R. ; Maunz, P. ; Duan, L.-M. ; Kim, J.: Large-scale modular quantum-computer architecture with atomic memory and photonic interconnects. In: *Physical Review A* 89 (2014), feb, Issue 2. http://dx.doi.org/10.1103/physreva.89.022317. – DOI 10.1103/physreva.89.022317

[Neu et al. 2012]
Neu, Elke ; Agio, Mario ; Becher, Christoph: Photophysics of single silicon vacancy centers in diamond: implications for single photon emission. In: *Optics Express* 20

(2012), aug, Issue 18, pp. 19956. http://dx.doi.org/10.1364/oe.20.019956. – DOI 10.1364/oe.20.019956

[Neu et al. 2013]
Neu, Elke ; Hepp, Christian ; Hauschild, Michael ; Gsell, Stefan ; Fischer, Martin ; Sternschulte, Hadwig ; Steinmüller-Nethl, Doris ; Schreck, Matthias ; Becher, Christoph: Low-temperature investigations of single silicon vacancy colour centres in diamond. In: *New Journal of Physics* 15 (2013), Issue 4, 043005. http://stacks.iop.org/1367-2630/15/i=4/a=043005

[Neu et al. 2011]
Neu, Elke ; Steinmetz, David ; Riedrich-Möller, Janine ; Gsell, Stefan ; Fischer, Martin ; Schreck, Matthias ; Becher, Christoph: Single photon emission from silicon-vacancy colour centres in chemical vapour deposition nanodiamonds on iridium. In: *New Journal of Physics* 13 (2011), Issue 2, 025012. http://stacks.iop.org/1367-2630/13/i=2/a=025012

[Neu 2012]
Neu, Elke K.: *Silicon vacancy color centers in chemical vapor deposition diamond : new insights into promising solid state single photon sources*, Universität des Saarlandes, PhD Thesis, 2012. http://dx.doi.org/http://dx.doi.org/10.22028/D291-22802. – Elektronische Ressource. – DOI http://dx.doi.org/10.22028/D291–22802

[Nguyen et al. 2019a]
Nguyen, C. T. ; Sukachev, D. D. ; Bhaskar, M. K. ; Machielse, B. ; Levonian, D. S. ; Knall, E. N. ; Stroganov, P. ; Chia, C. ; Burek, M. J. ; Riedinger, R. ; Park, H. ; Lončar, M. ; Lukin, M. D.: An integrated nanophotonic quantum register based on silicon-vacancy spins in diamond. In: *Physical Review B* 100 (2019), oct, Issue 16. http://dx.doi.org/10.1103/physrevb.100.165428. – DOI 10.1103/physrevb.100.165428

[Nguyen et al. 2019b]
Nguyen, C. T. ; Sukachev, D. D. ; Bhaskar, M. K. ; Machielse, B. ; Levonian, D. S. ; Knall, E. N. ; Stroganov, P. ; Riedinger, R. ; Park, H. ; Lončar, M. ; Lukin, M. D.: Quantum Network Nodes Based on Diamond Qubits with an Efficient Nanophotonic Interface. In: *Physical Review Letters* 123 (2019), oct, Issue

18. http://dx.doi.org/10.1103/physrevlett.123.183602. – DOI 10.1103/physrevlett.123.183602

[Peev et al. 2009]
Peev, M ; Pacher, C ; Alléaume, R ; Barreiro, C ; Bouda, J ; Boxleitner, W ; Debuisschert, T ; Diamanti, E ; Dianati, M ; Dynes, J F. ; Fasel, S ; Fossier, S ; Fürst, M ; Gautier, J-D ; Gay, O ; Gisin, N ; Grangier, P ; Happe, A ; Hasani, Y ; Hentschel, M ; Hübel, H ; Humer, G ; Länger, T ; Legré, M ; Lieger, R ; Lodewyck, J ; Lorünser, T ; Lütkenhaus, N ; Marhold, A ; Matyus, T ; Maurhart, O ; Monat, L ; Nauerth, S ; Page, J-B ; Poppe, A ; Querasser, E ; Ribordy, G ; Robyr, S ; Salvail, L ; Sharpe, A W. ; Shields, A J. ; Stucki, D ; Suda, M ; Tamas, C ; Themel, T ; Thew, R T. ; Thoma, Y ; Treiber, A ; Trinkler, P ; Tualle-Brouri, R ; Vannel, F ; Walenta, N ; Weier, H ; Weinfurter, H ; Wimberger, I ; Yuan, Z L. ; Zbinden, H ; Zeilinger, A: The SECOQC quantum key distribution network in Vienna. In: *New Journal of Physics* 11 (2009), jul, Issue 7, pp. 075001. http://dx.doi.org/10.1088/1367-2630/11/7/075001. – DOI 10.1088/1367–2630/11/7/075001

[Pfister et al. 2016]
Pfister, A. D. ; Salz, M. ; Hettrich, M. ; Poschinger, U. G. ; Schmidt-Kaler, F.: A quantum repeater node with trapped ions: a realistic case example. In: *Applied Physics B* 122 (2016), Issue 4, 1–19. http://dx.doi.org/10.1007/s00340-016-6362-7. – DOI 10.1007/s00340–016–6362–7. – ISSN 1432–0649

[Pingault et al. 2014]
Pingault, Benjamin ; Becker, Jonas N. ; Schulte, Carsten H. ; Arend, Carsten ; Hepp, Christian ; Godde, Tillmann ; Tartakovskii, Alexander I. ; Markham, Matthew ; Becher, Christoph ; Atatüre, Mete: All-Optical Formation of Coherent Dark States of Silicon-Vacancy Spins in Diamond. In: *Physical Review Letters* 113 (2014), dec, Issue 26. http://dx.doi.org/10.1103/physrevlett.113.263601. – DOI 10.1103/physrevlett.113.263601

[Piracha et al. 2016a]
Piracha, Afaq H. ; Rath, Patrik ; Ganesan, Kumaravelu ; Kühn, Stefan ; Pernice, Wolfram H. P. ; Prawer, Steven: Scalable Fabrication of Integrated Nanophotonic Circuits on Arrays of Thin Single Crystal Diamond Membrane Windows. In: *Nano Letters* 16 (2016), apr, Issue 5, pp. 3341–3347. http://dx.doi.org/10.1021/acs.nanolett.6b00974. – DOI 10.1021/acs.nanolett.6b00974

[Piracha et al. 2016b]
Piracha, Afaq H. ; Ganesan, Kumaravelu ; Lau, Desmond W. M. ; Stacey, Alastair ; McGuinness, Liam P. ; Tomljenovic-Hanic, Snjezana ; Prawer, Steven: Scalable fabrication of high-quality, ultra-thin single crystal diamond membrane windows. In: *Nanoscale* 8 (2016), Issue 12, pp. 6860–6865. http://dx.doi.org/10.1039/c5nr08348f. – DOI 10.1039/c5nr08348f

[Purcell 1995]
Purcell, E. M.: Spontaneous Emission Probabilities at Radio Frequencies. In: *Confined Electrons and Photons*. Springer US, 1995, pp. 839–839

[Riedel 2017]
Riedel, Daniel: *Engineering of the photonic environment of single nitrogen-vacancy centers in diamond*, Universität Basel, PhD Thesis, 2017

[Riedel et al. 2017]
Riedel, Daniel ; Söllner, Immo ; Shields, Brendan J. ; Starosielec, Sebastian ; Appel, Patrick ; Neu, Elke ; Maletinsky, Patrick ; Warburton, Richard J.: Deterministic Enhancement of Coherent Photon Generation from a Nitrogen-Vacancy Center in Ultrapure Diamond. In: *Physical Review X* 7 (2017), sep, Issue 3. http://dx.doi.org/10.1103/physrevx.7.031040. – DOI 10.1103/physrevx.7.031040

[Riehle 2006]
Riehle, Fritz: *Frequency Standards*. Wiley-VCH https://www.ebook.de/de/product/21192652/fritz_riehle_frequency_standards.html

[Ritter et al. 2012]
Ritter, Stephan ; Nolleke, Christian ; Hahn, Carolin ; Reiserer, Andreas ; Neuzner, Andreas ; Uphoff, Manuel ; Mucke, Martin ; Figueroa, Eden ; Bochmann, Joerg ; Rempe, Gerhard: An elementary quantum network of single atoms in optical cavities. In: *Nature* 484 (2012), April, Issue 7393, 195–200. http://dx.doi.org/10.1038/nature11023. – ISSN 0028–0836

[Rogers et al. 2014a]
Rogers, Lachlan J. ; Jahnke, Kay D. ; Metsch, Mathias H. ; Sipahigil, Alp ; Binder, Jan M. ; Teraji, Tokuyuki ; Sumiya, Hitoshi ; Isoya, Junichi ; Lukin, Mikhail D. ; Hemmer, Philip ; Jelezko, Fedor: All-Optical Initialization, Readout, and Coherent Preparation of Single Silicon-Vacancy Spins in Diamond. In:

Physical Review Letters 113 (2014), dec, Issue 26. http://dx.doi.org/10.1103/physrevlett.113.263602. – DOI 10.1103/physrevlett.113.263602

[Rogers et al. 2019]
Rogers, Lachlan J. ; Wang, Ou ; Liu, Yan ; Antoniuk, Lukas ; Osterkamp, Christian ; Davydov, Valery A. ; Agafonov, Viatcheslav N. ; Filipovski, Andrea B. ; Jelezko, Fedor ; Kubanek, Alexander: Single Si - V- Centers in Low-Strain Nanodiamonds with Bulklike Spectral Properties and Nanomanipulation Capabilities. In: *Physical Review Applied* 11 (2019), feb, Issue 2. http://dx.doi.org/10.1103/physrevapplied.11.024073. – DOI 10.1103/physrevapplied.11.024073

[Rogers et al. 2014b]
Rogers, L.J. ; Jahnke, K.D. ; Teraji, T. ; Marseglia, L. ; Müller, C. ; Naydenov, B. ; Schauffert, H. ; Kranz, C. ; Isoya, J. ; McGuinness, L.P. ; Jelezko, F.: Multiple intrinsically identical single-photon emitters in the solid state. In: *Nature Communications* 5 (2014), aug, pp. 4739. http://dx.doi.org/10.1038/ncomms5739. – DOI 10.1038/ncomms5739

[Rose et al. 2018]
Rose, Brendon C. ; Huang, Ding ; Zhang, Zi-Huai ; Stevenson, Paul ; Tyryshkin, Alexei M. ; Sangtawesin, Sorawis ; Srinivasan, Srikanth ; Loudin, Lorne ; Markham, Matthew L. ; Edmonds, Andrew M. ; Twitchen, Daniel J. ; Lyon, Stephen A. ; Leon, Nathalie P.: Observation of an environmentally insensitive solid-state spin defect in diamond. In: *Science* 361 (2018), jul, Issue 6397, pp. 60–63. http://dx.doi.org/10.1126/science.aao0290. – DOI 10.1126/science.aao0290

[Saleh u. Teich 2008]
Saleh, Bahaa E. ; Teich, Malvin C.: *Grundlagen der Photonik*. Wiley VCH Verlag GmbH https://www.ebook.de/de/product/7017400/bahaa_e_a_saleh_malvin_carl_teich_grundlagen_der_photonik.html. – ISBN 3527406778

[Schirhagl et al. 2014]
Schirhagl, Romana ; Chang, Kevin ; Loretz, Michael ; Degen, Christian L.: Nitrogen-Vacancy Centers in Diamond: Nanoscale Sensors for Physics and Biology. In: *Annual Review of Physical Chemistry* 65 (2014), apr, Issue 1, pp. 83–105. http://dx.doi.org/10.1146/annurev-physchem-040513-103659. – DOI 10.1146/annurev–physchem–040513–103659

[Sohn et al. 2018]
Sohn, Young-Ik ; Meesala, Srujan ; Pingault, Benjamin ; Atikian, Haig A. ; Holzgrafe, Jeffrey ; Gündoğan, Mustafa ; Stavrakas, Camille ; Stanley, Megan J. ; Sipahigil, Alp ; Choi, Joonhee ; Zhang, Mian ; Pacheco, Jose L. ; Abraham, John ; Bielejec, Edward ; Lukin, Mikhail D. ; Atatüre, Mete ; Lončar, Marko: Controlling the coherence of a diamond spin qubit through its strain environment. In: *Nature Communications* 9 (2018), may, Issue 1. http://dx.doi.org/10.1038/s41467-018-04340-3. – DOI 10.1038/s41467–018–04340–3

[Song et al. 2016]
Song, Guo-Zhu ; Wu, Fang-Zhou ; Zhang, Mei ; Yang, Guo-Jian: Heralded quantum repeater based on the scattering of photons off single emitters using parametric down-conversion source. In: *Scientific Reports* 6 (2016), jun, Issue 1. http://dx.doi.org/10.1038/srep28744. – DOI 10.1038/srep28744

[Stahl 2018]
Stahl, Alexander: *Aufbau und Test eines konfokalen Mikroskops für Untersuchungen von Farbzentren bei mK-Temperaturen*, Johannes Gutenberg-Universität Mainz, Master Thesis, 2018

[Sternschulte et al. 1994]
Sternschulte, H. ; Thonke, K. ; Sauer, R. ; Münzinger, P. C. ; Michler, P.: 1.681-eV luminescence center in chemical-vapor-deposited homoepitaxial diamond films. In: *Physical Review B* 50 (1994), nov, Issue 19, pp. 14554–14560. http://dx.doi.org/10.1103/physrevb.50.14554. – DOI 10.1103/physrevb.50.14554

[Sukachev et al. 2017]
Sukachev, D. D. ; Sipahigil, A. ; Nguyen, C. T. ; Bhaskar, M. K. ; Evans, R. E. ; Jelezko, F. ; Lukin, M. D.: Silicon-Vacancy Spin Qubit in Diamond: A Quantum Memory Exceeding 10 ms with Single-Shot State Readout. In: *Physical Review Letters* 119 (2017), nov, Issue 22. http://dx.doi.org/10.1103/physrevlett.119.223602. – DOI 10.1103/physrevlett.119.223602

[Takeoka et al. 2014]
Takeoka, Masahiro ; Guha, Saikat ; Wilde, Mark M.: Fundamental rate-loss tradeoff for optical quantum key distribution. In: *Nature Communications* 5 (2014), oct, Issue 1. http://dx.doi.org/10.1038/ncomms6235. – DOI 10.1038/ncomms6235

[Tao et al. 2014]
Tao, Y. ; Boss, J. M. ; Moores, B. A. ; Degen, C. L.: Single-crystal diamond nanomechanical resonators with quality factors exceeding one million. In: *Nature Communications* 5 (2014), apr, Issue 1. http://dx.doi.org/10.1038/ncomms4638. – DOI 10.1038/ncomms4638

[Terhal 2015]
Terhal, Barbara M.: Quantum error correction for quantum memories. In: *Reviews of Modern Physics* 87 (2015), apr, Issue 2, pp. 307–346. http://dx.doi.org/10.1103/revmodphys.87.307. – DOI 10.1103/revmodphys.87.307

[Uphoff et al. 2015]
Uphoff, Manuel ; Brekenfeld, Manuel ; Rempe, Gerhard ; Ritter, Stephan: Frequency splitting of polarization eigenmodes in microscopic Fabry–Perot cavities. In: *New Journal of Physics* 17 (2015), jan, Issue 1, pp. 013053. http://dx.doi.org/10.1088/1367-2630/17/1/013053. – DOI 10.1088/1367–2630/17/1/013053

[Wan et al. 2018]
Wan, Noel H. ; Shields, Brendan J. ; Kim, Donggyu ; Mouradian, Sara ; Lienhard, Benjamin ; Walsh, Michael ; Bakhru, Hassaram ; Schröder, Tim ; Englund, Dirk: Efficient Extraction of Light from a Nitrogen-Vacancy Center in a Diamond Parabolic Reflector. In: *Nano Letters* 18 (2018), mar, Issue 5, pp. 2787–2793. http://dx.doi.org/10.1021/acs.nanolett.7b04684. – DOI 10.1021/acs.nanolett.7b04684

[Wolchover 2019]
Wolchover, Natalie: To Invent a Quantum Internet. In: *QuantaMagazine* (2019). https://www.quantamagazine.org/stephanie-wehner-is-designing-a-quantum-internet-20190925/

[Wootters u. Zurek 1982]
Wootters, W. K. ; Zurek, W. H.: A single quantum cannot be cloned. In: *Nature* 299 (1982), oct, Issue 5886, pp. 802–803. http://dx.doi.org/10.1038/299802a0. – DOI 10.1038/299802a0

[Zaitsev 2001]
Zaitsev, Alexander M.: *Optical Properties of Diamond*. Springer Berlin Heidelberg, 2001 DOI 10.1007/978–3–662–04548–0. http://dx.doi.org/10.1007/978-3-662-04548-0

[Zhang et al. 2018]
Zhang, Jingyuan L. ; Sun, Shuo ; Burek, Michael J. ; Dory, Constantin ; Tzeng, Yan-Kai ; Fischer, Kevin A. ; Kelaita, Yousif ; Lagoudakis, Konstantinos G. ; Radulaski, Marina ; Shen, Zhi-Xun ; Melosh, Nicholas A. ; Chu, Steven ; Lončar, Marko ; Vučković, Jelena: Strongly Cavity-Enhanced Spontaneous Emission from Silicon-Vacancy Centers in Diamond. In: *Nano Letters* 18 (2018), feb, Issue 2, pp. 1360–1365. http://dx.doi.org/10.1021/acs.nanolett.7b05075. – DOI 10.1021/acs.nanolett.7b05075

List of Figures

Cheers!

Zum Abschluss dieser Arbeit möchte ich die Gelegenheit nutzen, um danke zu sagen. An erster Stelle geht mein besonderer Dank an meinen Betreuer Marcel Salz, ohne den diese Arbeit nicht möglich gewesen wäre. Marcel hat mir von Faserresonatoren bis hin zu Quantenrepeatern unglaublich viel Wissen anschaulich und klar vermittelt. Neben der Theorie konnte ich eine Menge an experimentellen Methoden im Umgang mit Fasern, Optik, Elektronik und vielem mehr von ihm lernen. Ohne Marcels vorausschauende Planung und Konstruktion des Experiments, die extrem aufwändige Beschaffung einer geeigneten Diamant Membran, die mehrfach um die halbe Welt gereist ist, und die Durchführung des Experiments mit endlosem Überheben von flüssigem Stickstoff und Helium, wäre das Projekt nicht ansatzweise soweit voran gekommen. Das Ganze klappt natürlich auch nur mit einem motiviertem und tatkräftigem Projektleiter. Für die Begeisterung für das Thema, seinen Enthusiasmus für Physik und das Vertrauen in uns möchte ich mich bei Ferdinand Schmidt-Kaler bedanken. Besonders dankbar bin ich ihm für die Ermöglichung und Unterstützung eines unvergesslich schönen Forschungsaugenhaltes in der Gruppe von Nir Bar-Gill in Jerusalem. Bei Alexander Stahl und Max Hettrich möchte ich mich für die gute Vorbereitung des Kryostats und Labors bedanken. Außerdem gilt mein Dank der ganzen Arbeitsgruppe, die eine tolle Arbeitsatmosphäre und Zusammenhalt schafft. Bei Dmitry Budker möchte ich mir für die Zweitkorrektur bedanken.
Für die Durchführung des Projekts ist die Kollaboration mit einer ganzen Reihe von weiteren Wissenschaftlern äußerst wichtig gewesen. Deswegen möchte ich mich auch bedanken bei:

- Athavan Nadarajah, Alastair Stacey und Steven Prawer (Uni Melbourne) für die Fabrikation und Applizierung der Diamant Membran
- Michael Kieschnik und Jan Meijer (Uni Leipzig) für die Implantierung
- Max Pallmann, Julia Benedikter und David Hunger (KIT) für den Faserresonator und die besonders hilfreiche Beratung in vielen Bereichen
- Philipp Fuchs, Morgane Gandil, Michel Challier, Elke Neu, Christoph Becher (Uni Saarbrücken) für Hinweise zu Diamant und SiVs und der Untersuchung mit Konfokalmikroskopie und SEM

- Julia Heupel und Cyril Popov (Uni Kassel) für die Herstellung neuer Diamantproben

Die Tieftemperatur Messungen hätten ohne kygogene Flüssigkeiten nicht durchgeführt werden können, deswegen bedanke ich mich bei Christian Olf und Sebastian Fuchs, für die technische Unterstützung. Bei allen Fragen zu Elektrik und IT waren Heinz Lenk und Michael Boeßenecker eine hervorragende Unterstützung. Außerdem gilt beim Dank Christine Best, Elvira Stuck-Kerth und Andrea Graham für die Hilfe bei allen bürokratischen Angelegenheiten und natürlich den Reisekostenabrechnungen. Zudem bedanke ich mich bei allen Mitarbeitern der Mechanikwerkstatt, sowie der Etatverwaltung am Institut für Physik.
Schließlich möchte ich mich bei meinen Kommilitonen und WG Mitbewohnern bedanken, aus denen in den letzten Jahren gute Freunde geworden sind. Durch sie wird mir die Zeit des Studiums in besonders schöner Erinnerung bleiben. Ebenfalls danke ich allen Freunden und natürlich meiner Familie, ganz besonders meinen Eltern, Birgit und Dietmar, sowie meinen Großeltern für ihre Unterstützung, die mir das Studium der Physik ermöglicht hat.